Broadband Characterization Techniques for RF Materials and Engineered Composites

Dissertation

Presented in Partial Fulfillment of the Requirements for
the Degree Doctor of Philosophy in the
Graduate School of The Ohio State University

By

Jae-Young Chung, B.S., M.S.

Graduate Program in Electrical and Computer Engineering

The Ohio State University

2010

Dissertation Committee:

John L. Volakis, Advisor

Kubilay Sertel, Co-advisor

Joel T. Johnson

Ronald M. Reano

Abstract

Recent interest in new materials, including metamaterials and magneto-dielectrics, for RF applications provided strong impetus for measurement techniques to characterize associated permittivity, permeability, and loss factors. Traditional measurement techniques are not readily available to characterize these engineered composites. For example, conventional resonant cavity methods are known to be narrowband and require careful sample preparation. For metamaterials and magneto-dielectrics, broadband characterization is particularly necessary to observe their dispersive properties. Also, a challenge with new materials, such as layered composites, is the restriction in measurable shape, size and thickness. Often, small and irregularly shaped samples are available, making their characterization challenging.

With these issues in mind, this dissertation is aimed at developing new characterization techniques for novel engineered composites. Specifically, four techniques are presented to characterize textured metamaterial volumetric structures, magneto-dielectric mixtures and films, and highly conductive metallo-dielectric films. One of the presented techniques is based on a Gaussian beam illumination. In this method, the Gaussian beam is used to illuminate the center of layered material samples to avoid diffraction from sample edges. In contrast to generating the Gaussian beam using bandwidth-limited lenses, the beam was reconstructed by scanning a probe

over a virtual aperture much like the synthetic aperture radar process. This approach was successfully employed at X-band (8 to 12 GHz) for the characterization of slow-wave propagation in a layered metamaterial slab. However, the Gaussian beam method is not feasible at low frequencies as it requires a large sample aperture ($> \lambda$ in size). The second characterization method was, therefore, developed to measure smaller samples ($< \lambda/4$) in lower frequencies (100 MHz to 4.8 GHz). More specifically, a stripline fixture, supporting transverse electromagnetic wave propagation, was designed to characterize permittivity and permeability of ferrite mixtures. This approach is suitable for reasonably thick samples but not accurate for extremely thin samples (thickness $t < 1$ mm). For thin material composites, we employed a planar microstrip line based structure for accurate measurements. Furthermore, a new de-embedding process based on full-wave simulations was developed to avoid uncertainties in conventional quasi-static de-embedding process. The last and 4th presented method was developed for material samples with high conductivity. As compared to the low-conductive materials presented already, of interest with these materials is the characterization of conductivity and resistivity. Using a 1-port reflection coefficient measurement set-up, these quantities were extracted for multilayer metallo-dielectric films over broadbandwidth (100 MHz to 15 GHz).

To my wife and daughter

Acknowledgments

I would like to express sincerest thanks to my advisor, Prof. John L. Volakis, for his guidance and patience made this dissertation possible. I have learned great deals for being a leading engineer through his enthusiasm and uncompromised professionalism. I am also grateful to Dr. Kubilay Sertel for his continuous guidance throughout years as a co-advisor and mentor. I have enjoyed working with him, and deeply appreciate his contribution to this work. I may not have another chance to work with a researcher like him, who has profound insights on every field in scientific research. I also thank to my previous advisor Dr. Chi-Chih Chen who opened the world of electromagnetics to me. The valuable knowledge and skills that I learned from him have been the backbone of my research over these years. I appreciate Prof. Joel T. Johnson and Prof. Ronald M. Reano for being my candidacy exam committee as well as dissertation reading committee. They not only took time off from their busy schedule but also kindly guided me to complete this work. I would also like to acknowledge Dr. Lanlin Zhang and Dr. Niru Nahar for the help and guidance pertaining to unfamiliar fields such as material science and optics.

It has been a great experience to meet and become good friends with many colleagues at ElectroSciene Laboratory (ESL). I really want to thank for their valuable discussion and friendship. Special thanks to my officemates - Elias Alwan, Nil Apaydin, Erdinc Irci, Tao Peng and Ioannis Tzanidis. My gratitude is also extended for

other friends at ESL - Kenny Browne, Chun-Sik Chae, Justin Kasemodel, Jun Seok Lee, Gil Young Lee, Haksu Moon, William Moulder, James Park, and Jing Zhao. The list would be incomplete without mentioning friends with whom I started this journey - Hyunchul Jung, Kyung-young Jung, Yong-Chae Jung, Youngseo Ko, Praphun Naenna, Salih Yarga, and Yijun Zhou.

Finally, I would like to thank my family. The unconditional love and support of my parents and parents-in-law have been the greatest motivation during the graduate study. And most importantly, I would like to express the deepest gratitude to my wife, Ju-Hyun, who has been a super mom by raising Sang-Yoo and building her career in difficult situation. Thank you and I love you!

Vita

September 19, 1976	Born - Seoul, Korea
February, 2002	B.S., Electrical Eng., Yonsei University, Seoul, Korea
March, 2007	M.S., Electrical and Computer Eng., The Ohio State University, Columbus, USA
February, 1997 - April, 1999	Signalman, Republic of Korea Marine Corps, Pohang, Korea
June, 2002 - June, 2004	RF Engineer, Motorola, Seoul, Korea
September, 2004 - present	Graduate Research Associate, ElectroScience Laboratory, The Ohio State University, Columbus, USA

Publications

Journal Publications

Jae-Young Chung and Chi-Chih Chen, "Two-layer dielectric rod antenna," *IEEE Transaction on Antennas and Propagation*, vol. 56, no. 6, pp. 1541-1547, June 2008.

Jae-Young Chung, Kubilay Sertel, and John L. Volakis, "A Non-invasive metamaterial characterization system using synthetic Gaussian aperture," *IEEE Transaction on Antennas and Propagation*, vol. 57, no. 7, pp. 2006-2013, July 2009.

Jae-Young Chung, Kubilay Sertel, and John L. Volakis, "Broadband characterization of bulk and thin magnetic composites using stripline structures," *submitted to IEEE Transaction on Antennas and Propagation*

.

Conference Publications

Jae-Young Chung and Chi-Chih Chen, "A dual-linear polarization UWB dielectric rod probe design," *Antenna Measurement Techniques Association (AMTA) Symposium*, Austin, TX, USA, 2006.

Jae-Young Chung and Chi-Chih Chen, "Ultra-wide bandwidth two-layer dielectric rod antenna," *IEEE Antenna and Propagation Society (APS) Symposium*, Honolulu, HI, USA, 2007.

Jae-Young Chung, Kubilay Sertel, and John L. Volakis, "Synthetic aperture Gaussian beam measurement system for wideband characterization of RF materials and metamaterials," *IEEE Antenna and Propagation Society (APS) Symposium*, San Diego, CA, USA, 2008.

Jae-Young Chung, Kubilay Sertel, and John L. Volakis, "A Non-invasive metamaterial characterization system using synthetic Gaussian aperture," *XXIXth General Assembly of Union Radio Science International (URSI)*, Chicago, IL, USA, 2008.

Jae-Young Chung, Kubilay Sertel, and John L. Volakis, "Broadband characterization of engineered composites," *URSI-National Radio Science Meeting*, Boulder, CO, USA, 2009.

Jae-Young Chung, Kubilay Sertel, and John L. Volakis, "Broadband permeability characterization of thin and small magnetic composites with patterned anisotropy," *submitted to 2010 IEEE Antennas and Propagation Society Symposium*, Toronto, Canada, July, 2010.

Fields of study

Major Field: Electrical and Computer Engineering

Studies in:

Electromagnetics
RF Circuits
Mathematics

Table of Contents

Page

List of Tables

List of Figures

Chapter 1

INTRODUCTION

1.1 Motivation and Objectives

Recent progress in radio frequency (RF) materials and engineered composites that exhibit unique electromagnetic behavior hold promise to dramatically improve the performance of RF components and antenna elements. For example, novel dielectrics and magnetic materials with tunable electrical properties have recently been developed using advanced mixing technologies [1–3]. Furthermore, it has been shown that periodic alignments of such homogeneous materials reduce the loss factors (which typically hinder the utilization at RF frequencies) [4, 5]. In fact, extensive studies on periodic engineered composites during the last decade drive the next big leap in electromagnetic research. Commonly termed as "metamaterials", composites such as negative refractive index materials [6, 7], magnetic photonic crystals [8, 9], magneto-dielectric [10, 11] and metallo-dielectric materials [12, 13] are realized using periodic repetitions of a "unit cell" geometry. With the correct alignment of unit cells, these metamaterials exhibit extraordinary properties never found in nature (e.g., sub-wavelength focusing, slow-wave mode propagation, high surface impedance, etc.).

The incorporation of the above materials as substrates and/or superstrates in RF applications requires an accurate characterization of their electromagnetic properties. As these materials are rather complicated in structure (e.g., combinations of inhomogeneous unit cells), highly dispersive and often anisotropic, conventional material characterization techniques may not be readily applicable. In this context, the goal of this dissertation is aimed at developing new measurement fixtures and methodologies for accurate characterization of advanced RF materials, metamaterials, and engineered composites.

Unlike solid-state physics and material science, that concerns atomic and microscopic material properties, here we are particularly interested in the characterization of macroscopic electromagnetic material properties as defined by the constitutive relations:

$$\mathbf{D} = \varepsilon \mathbf{E} \ , \tag{1.1}$$

$$\mathbf{B} = \mu \mathbf{H} \ . \tag{1.2}$$

Here, ε and μ are the permittivity and permeability that represent the macroscopic behavior relating the field intensities ($\mathbf{E}$ and $\mathbf{H}$) and the flux densities ($\mathbf{D}$ and $\mathbf{B}$) inside the material. For a simple material, they are typically expressed as complex numbers (i.e., $\varepsilon = \varepsilon' - \varepsilon''$ and $\mu = \mu' - \mu''$) where the real and imaginary parts indicate the amount of electric and magnetic energy stored and dissipated in the material. However, the macroscopic properties of engineered composites are often represented by more complicated forms making their characterization difficult. For example, they can be functions of orientation [i.e., anisotropic, $\bar{\bar{\varepsilon}}$ and $\bar{\bar{\mu}}$], position [i.e., inhomogeneous, $\varepsilon(x,\ y,\ z)$ and $\mu(x,\ y,\ z)$], frequency [i.e., dispersive, $\varepsilon(f)$ and $\mu(f)$], and applied fields [i.e., nonlinear, $\varepsilon(E)$ and $\mu(H)$].

The history of ε and μ characterization dates back from the early 1930s right after Debye, a Nobel prize laureate, had established the dielectric theory [14]. However, the development of reliable characterization techniques had not kept pace with the theory until World War II, which provoked the research in functional electromagnetic materials for electromagnetic signature control, stealth technology, microwave absorbers, etc [15]. Despite the number of books, review papers, and hundreds of journal papers that have been published since then, material characterization continues to be one of the most active research topics as new materials and composites find applications in new areas. In particular, during the last decade, there has been renewed/intense interest in material characterization due to the following reasons:

1. As mentioned, the evolution of engineered composites, such as novel mixtures and periodic structures, requires new characterization techniques to be developed. As these artificial materials are sensitive to external perturbation, there is a high demand on developing non-invasive characterization techniques to improve the measurement accuracy.

2. With the evergrowing push for wide-band RF devices, it is necessary to characterize material properties over a broad bandwidth. In addition, broadband characterization capability is also essential to capture materials' dispersive responses to identify the usable frequency range of the material.

3. With dramatic increase in the clock speed of electronic devices, there is an absolute need to design characterization techniques for the GHz frequency range.

This task presents considerable challenges since at such high frequencies measurements are highly vulnerable to small errors in sample alignment, air-gaps between experiment apparatus and sample, higher-order mode propagation, etc.

With these issues in mind, during the past four years, we have developed several broadband material characterization techniques suitable for complex composites and metamaterials. Specifically, four new techniques for the characterization of bulk and thin film engineered composites, as illustrated in Fig. 1.1, are presented in this dissertation. Key contributions of the new techniques are:

1. Development of a new non-invasive characterization method using a virtual Gaussian distributed aperture: This method avoids the use of problematic lenses in conventional free-space measurement systems by synthesizing the Gaussian beam from a scanned probe array. Using this system, a slow-wave behavior in a multilayer band-gap structure was accurately characterized at 8-12 GHz.

2. Design of a new broadband fixture for bulk material characterization: A tapered stripline structure is developed for simultaneous characterization of ε and μ. The fixture is optimized to operate in the broad frequency range of 100 MHz to 4.8 GHz, i.e., 48:1 bandwidth.

3. Design of a new property de-embedding algorithm for thin composites and anisotropic magneto-dielectrics: In contrast to conventional algorithms using quasi-static analyses, the new algorithm de-embeds the material properties based on full-wave simulation data. Together with a microstrip line measurement fixture, this enable us to characterize a thin and small (1 cm $\times$ 1 cm $\times$ 500 μm) magnetic composites with in-plane anisotropy.

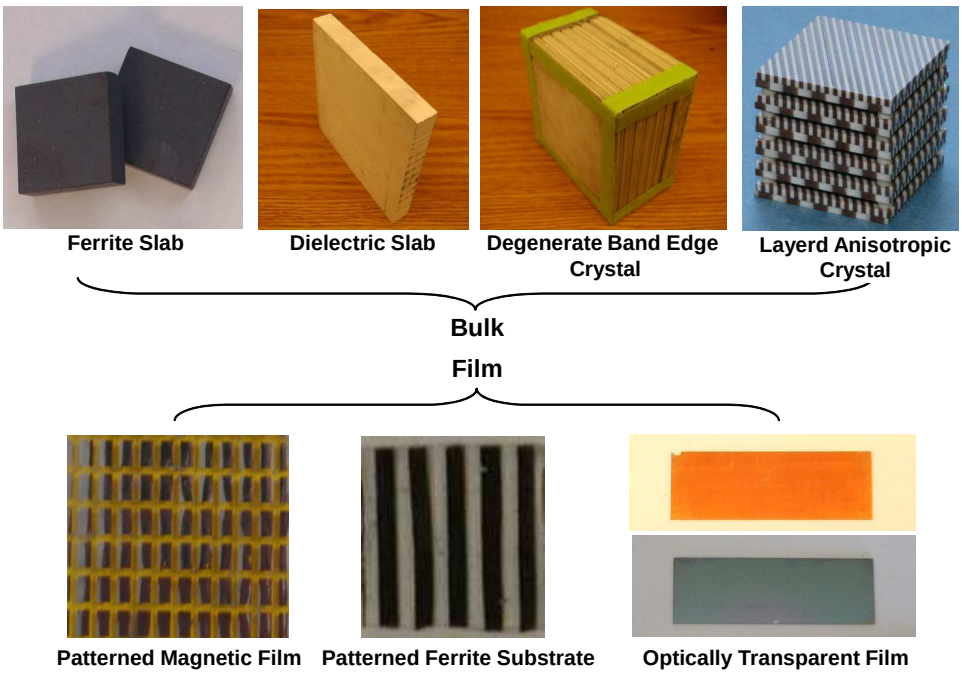

(a)

Figure 1.1: Examples of bulk and film type engineered composites.

4. Characterization of RF conductivity of metallic films: Supplementary to the abovementioned characterization of ε and μ, a technique for broadband conductivity (σ) characterization is developed using an open-ended coaxial probe. With this method, the effective σ of multilayer metallo-dielectric films could be characterized at 100 MHz to 15 GHz frequency range.

1.2 Organization of the Dissertation

A chapter-by-chapter outline of the dissertation is given as follows:

Chapter 2 is devoted to the review of existing material characterization techniques. Advantages and disadvantages of various techniques are investigated under considerations such as operation bandwidth, measurable electrical properties, required sample size, shape, and thickness. Also discussed is the rationale on the selection/development of effective characterization techniques for complex engineered composites. As we extensively use the broadband transmission/reflection (T/R) method [16–18] throughout this dissertation, different types of the T/R methods and their property de-embedding techniques are discussed in detail.

Chapter 3 presents a new broadband technique for characterizing a metamaterial slab. This is a free-space transmission technique that employs a synthetic Gaussian aperture to illuminate a planar sample with a focused beam. Parametric studies for optimal Gaussian beam reconstruction are presented and examples are given on their importance. The chapter describes the measurement set-up with 2-D planar and 3-D spherical virtual apertures, and emphasize the advantages of the spherical virtual aperture system. The validity of the new approach and measurement uncertainties are examined from measurements of a known sample (e.g. dielectric slab). Following the validation, the measured transmission response of a layered metamaterial slab at X-band is presented.

For broadband RF material characterization (e.g., below 5 GHz), the free-space method in Chapter 3 is not practical due to its large set-up size (large horn antenna and sample are required). To overcome this issue, in Chapter 4, we proposed a tapered stripline method for broadband characterization of ε and μ at the frequency range of 100 MHz to 4.8 GHz. Simulation results to achieve an optimized fixture geometry are presented along with the upper frequency limitation due to higher-order modes.

Also, we describe the increase of measurement errors for thin sample characterization based on full-wave simulations.

Since the tapered stripline method is not applicable to characterize thin materials, in Chapter 5, we introduce a microstrip line method with a new de-embedding process. The latter utilizes data from full-wave simulations instead of usual quasi-static analyses (such as conformal mapping and variational method) to effectively calculate the in-plane properties of a small and thin sample (less than 1 cm $\times$ 1 cm $\times$ 500 μm). The procedure to formulate the governing equations in the new de-embedding process is described using lumped element analyses. We validate the proposed method by characterizing patterned ferrite composites fabricated in Material Science Department at The Ohio State University. The measured results are further compared with the data from a conventional impedance analyzer and mixing rules from effective medium theory.

In Chapter 6, we develop a technique to characterize conductivity (σ) and resistivity (ρ) of metallic films. In this method, an open-ended coaxial probe is employed for broadband measurements of film's reflection coefficient. Subsequently, σ and ρ are de-embedded using a closed-form formula developed by the so-called thin film approximation. Transparent conductive films are characterized over the frequency range of 100 MHz to 15 GHz with this method.

Conclusions of the presented works and discussions of future research topics are given in Chapter 7.

Chapter 2

REVIEW OF MATERIAL CHARACTERIZATION TECHNIQUES

2.1 Introduction

The term "material characterization" refers to the quantification of material properties. Among various properties, we narrow down our focus to electrical properties such as permittivity/permeability (ε/μ), dielectric-loss/magnetic-loss factors ($\tan\delta_\epsilon/\tan\delta_\mu$), conductivity/resistivity (σ/ρ), transmission/reflection responses, etc. These values are used to represent the macroscopic behavior of a material in interacting with electromagnetic fields. Material characterization is a classical electromagnetic research area and its importance has never overlooked during the high growth of RF technology. As a result, many books and extensive review papers have been published [15, 19–24]. In this chapter, we summarize the basic principle of electromagnetic material characterization and review the most popular techniques used in electromagnetic research.

Material characterization requires two steps: (1) the measure of material response to the impinging source fields and (2) the calculation of material properties from the obtained material response. For the first step (i.e., measurement), the source

fields are obviously the E- and H-fields. The crucial assumption in such electromagnetic measurement is that the impinging wave is relatively weak so that the original characteristic of the material sample under test does not change. This implies the interaction inside the sample must be linear to the strength of the time harmonic fields. However, it does not indicate the sample response against other source fields should be linear. For example, the permeability of ordered magnetic materials (e.g., ferrites and ferromagnetic materials) significantly varies by the strength of the biased magnetic field (i.e., applied DC field) [1,25]. Moreover, although the biased field is removed, the permeability does not return to the initial state as a remanent flux density still exists inside the material. As a matter of fact, characterizing such non-linearity is often the focus of attention.

The second step is called the "de-embedding" or "extraction" process. Using fundamental electromagnetic field analyses, material responses such as impedance, resonant frequency, scattering parameters (S-parameters) can be expressed in terms of material's properties. If a closed-form expression is available to relate these responses and material properties of interest, the de-embedding process is simple and straightforward. However, it is often unrealizable to obtain a closed-form expression, particularly when the measurement requires complicated steps. In this case, material properties can be numerically determined using an iterative solver [18, 26]. Both cases will be discussed in this dissertation along with the development of new characterization techniques.

To carry out accurate material characterization, a proper measurement fixture and de-embedding process should be correctly chosen or designed based on the following considerations:

- The state of the material sample (e.g., liquid, solid, powder, etc.)
- The size and shape of the sample (e.g., small, large, flat, sphere, toroid, thin, thick, etc.)
- The frequency range of interest (e.g., narrow or broadband, low or high frequency)
- The material parameters of interest (e.g., ε, μ or both, homogenized or localized properties, anisotropy, etc.)
- Measurement process (e.g., destructive or non-destructive, contact or non-contact)
- Required measurement accuracy
- Cost

There is no universal technique that covers all these considerations. It is the responsibility of an engineer to choose the most effective one based on requirements in characterization. Among numerous amount of reported techniques, in the next, we review three most widely-used characterization techniques. They are capacitance/inductance (C/L) method, resonant method, and transmission/reflection (T/R) method as illustrated in Fig. 2.1 [19, 27]. Their benefits and shortcomings are discussed with regard to the considerations listed above. Furthermore, the review provides the reasoning for the extensive use of the T/R method for the broadband characterization of engineered composites.

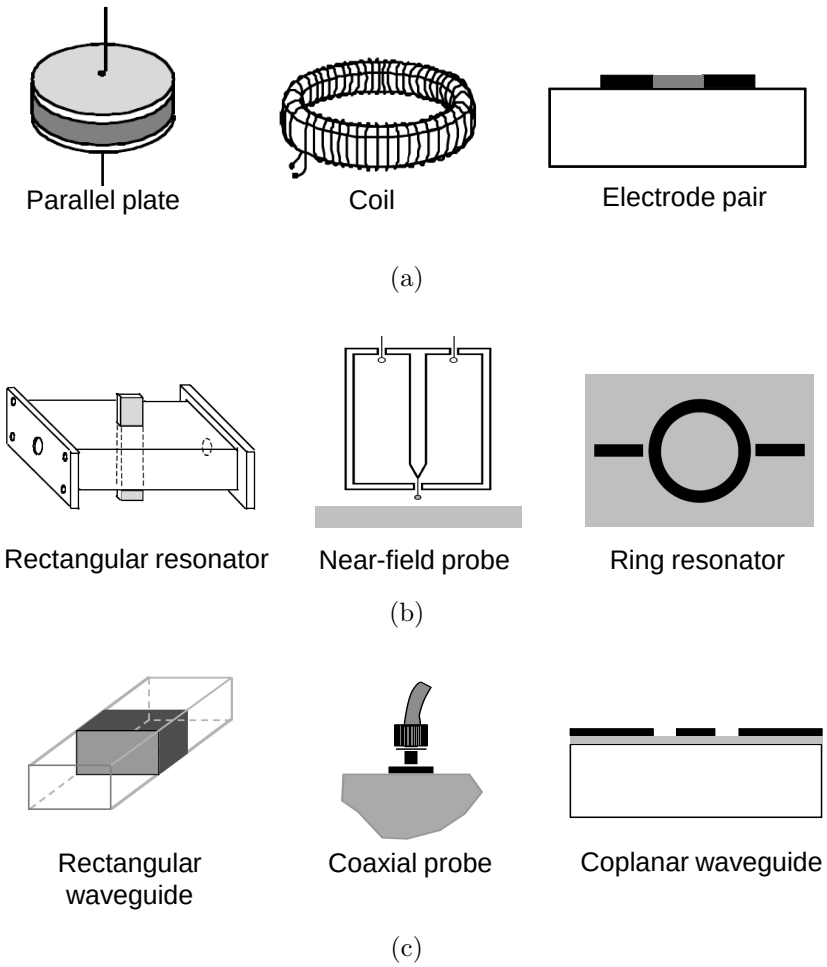

Figure 2.1: Illustrations of material characterization techniques: (a) capacitance/inductance methods, (b) resonant method, and (c) transmission/reflection methods.

2.2 Capacitance/Inductance Method for Low Frequency

This method de-embeds ε and μ from the capacitance (C) and inductance (L) captured in measurement fixtures (with the presence of a material sample) [28,29]. As in Fig. 2.1, the measurement of C and L are often realized using parallel plates and coil structures. The C/L method is also known as admittance/impedance method since

the measured C or L is embedded in a circuit parameter, which is either admittance (Y) or impedance (Z). That is,

$$Y_s = G_s + j\omega C_s, \tag{2.1}$$

$$Z_s = R_s + j\omega L_s, \tag{2.2}$$

where G_s and C_s are conductance and capacitance, and R_s and L_s are resistance and inductance inside the measurement fixtures. Equivalent circuit models for Y_s and Z_s are illustrated in Fig. 2.2(a) and (b). It is worth noting that the C/L method rely on the assumption that Y_s and Z_s are not affected by any inductive and capacitive factors, respectively. Although the measurement fixtures are carefully designed to hold this assumption, the impact of parasitic L and C are unavoidable as the frequency increases [28]. Consequently, a parallel LC resonator is formed and the measured Y_s or Z_s is distorted by its resonance at the higher frequency. Due to this problem, the operation frequency range of the C/L method is typically limited to < 1 GHz.

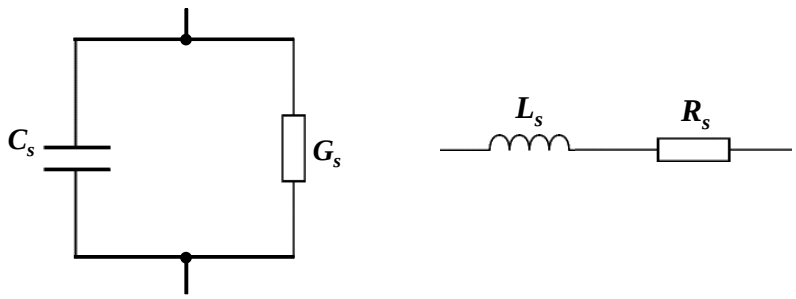

(a) (b)

Figure 2.2: Equivalent circuit models for (a) Y_s and (b) Z_s.

Despite the bandwidth limitation, the C/L method is widely-used in many EM laboratories due to its simple measurement set-up. In the following sections, we further discuss ε and μ characterizations from a commercial C/L method instrument available at Electroscience Laboratory: Agilent E4991A impedance analyzer [28].

2.2.1 Characterization of ε

Fig. 2.3 is a picture of the Agilent E4991A impedance analyzer connected with the 16454A dielectric test fixture for ε characterization. With this set-up, the admittance is measured between two electrodes while the sample is clamped in the middle. Prior to measuring the sample, a calibration must be performed via the measurements of three known standards (i.e., open-short-load) [30]. The open- and short-standard measurements are realized by separating and contacting the electrodes to each other. The load-standard is a material with known thickness and ε_r (e.g., Teflon slab of thickness 0.78 mm and $\varepsilon_r = 2.1$). It is found that more accurate results are obtained if the load-standard has similar properties to the saample [31].

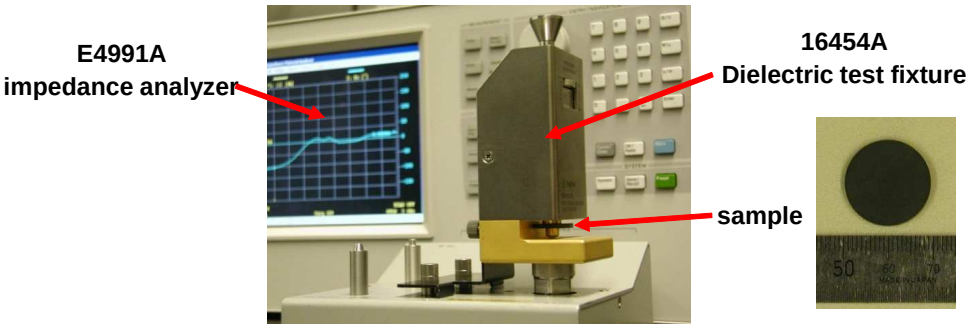

Figure 2.3: The ε characterization set-up using Agilent E4991A with 16454A.

Once the calibration is completed, the measured complex admittance can be expressed by (2.1). If we define the capacitance without the sample as C_0, (2.1) is re-written by

$$Y_s = j\omega C_0 \left(\frac{C_s}{C_0} - \frac{G_s}{\omega C_0} \right). \tag{2.3}$$

where the term in the parentheses is the relative permittivity of the sample. Namely,

$$\varepsilon_{rs} = \frac{C_s}{C_0} - j\frac{G_s}{\omega C_0}. \tag{2.4}$$

For electrodes whose contacting area is A with a separation t, $C_0 = A\varepsilon_0/t$ ($\varepsilon_0 = 8.854 \times 10^{-12}$ F/m, permittivity of free-space). If we substitute this value into (2.4), the real and imaginary parts of ε_{rs} are calculated by

$$\varepsilon'_{rs} = \frac{tC_s}{\varepsilon_0 A}, \tag{2.5}$$

$$\varepsilon''_{rs} = \frac{tG_s}{\varepsilon_0 \omega A}. \tag{2.6}$$

As an example, Fig. 2.4 shows the measured real and imaginary values of ε_{rs} of a ferrite composite. The sample was prepared by mixing powders of NiZn ferrite and Polydimethylsiloxane (PDMS) in the ratio of 50% and 50%. Afterwards, the mixed powder comdosite was secured by a cross-link agent and degassing process. Also noting that the thickness of the composite was 780 μm which is thinner than the required thickness ($t \leq 1$ mm) for the 16454A test fixture. As observed, the measured results show stable values up to 500 MHz (i.e., $\varepsilon'_{rs} \approx 4.6$, $\varepsilon''_{rs} \approx 0.01$). The permittivity of this composite is expected to be stable up to several GHz. After 500 MHz, however, the measured ε_{rs} starts to alter due to the resonance exhibited around 2 GHz. As mentioned, this resonance is due to the non-trivial inductance at higher frequency range, thereby forming a resonator with the capacitance inside the sample.

Because of this, the credible frequency range is limited to < 1 GHz, or more strictly < 500 MHz.

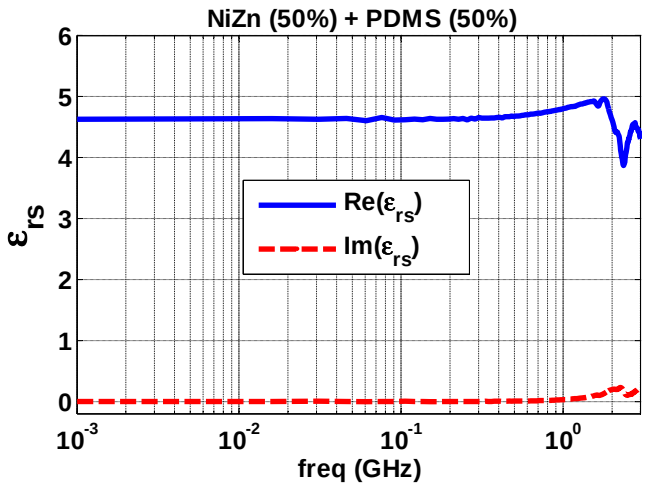

Figure 2.4: Permittivity of NiZn-PDMS composite measured with Agilent E4991A impedance analyzer.

2.2.2 Characterization of μ

A typical test configuration for the inductance measurement is the coil structure [see Fig. 2.1(a)]. In this set-up, a toroidal sample is coiled with a wire and the magnetic flux density ($\mathbf{B}$) is measured along the circumference of the toroid. However, the coil structure is not available at a frequency higher than 100 KHz due to the arise of parasitic capacitance in the windings [32]. To avoid such adverse effect, a coaxial line structure is used as a test fixture in the impedance analyzer set-up. Fig. 2.5 is the measurement set-up for the μ characterization. Also, Fig. 2.6 illustrate the details of the coaxial test fixture.

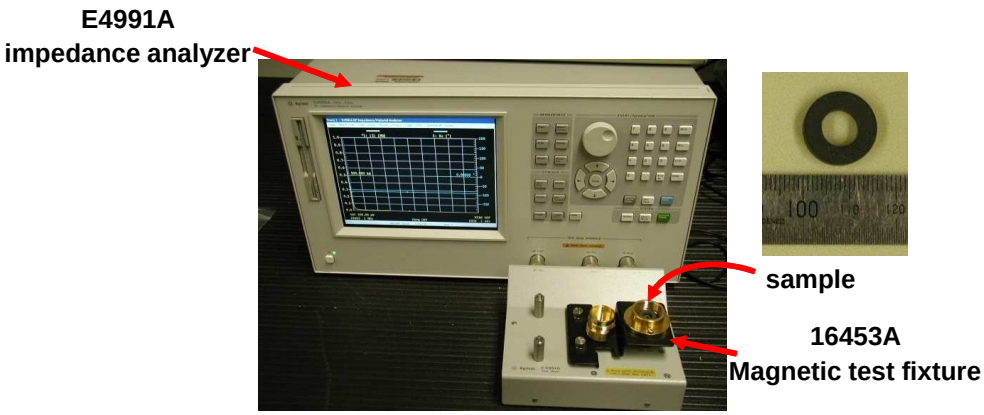

Figure 2.5: The μ characterization set-up using Agilent E4991A with 16453A.

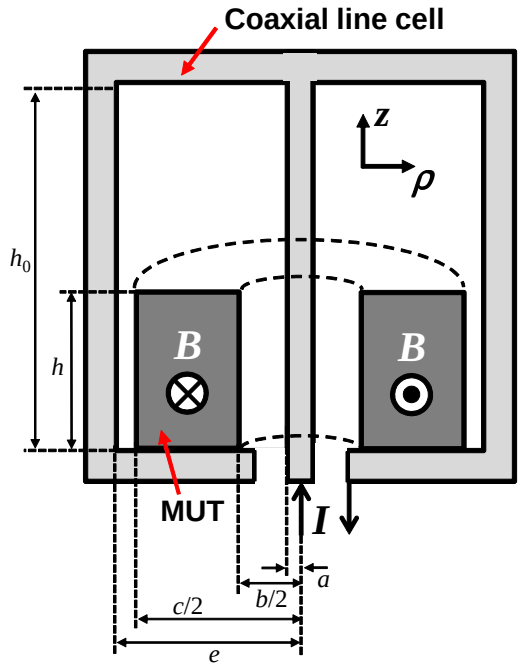

Figure 2.6: Cross-section of the 16453A coaxial test fixture.

With this set-up, the self-inductance inside the coaxial test cell can be calculated from the measurement of **B** induced by the current loop (I):

$$\begin{aligned} L_s &= \frac{1}{I}\int \mathbf{B}\cdot\,\mathbf{ds} \\ &= \int_{c/2}^{e}\int_{0}^{h_0}\frac{\mu_0}{2\pi\rho}\,d\rho dz + \int_{b/2}^{c/2}\int_{0}^{h}\frac{\mu_0\mu_r}{2\pi\rho}\,d\rho dz + \int_{b/2}^{c/2}\int_{h}^{h_0}\frac{\mu_0}{2\pi\rho}\,d\rho dz + \int_{a}^{b/2}\int_{0}^{h_0}\frac{\mu_0}{2\pi\rho}\,d\rho dz, \end{aligned} \tag{2.7}$$

where $\mu_0 = 4\pi\times10^{-7}$ and μ_{rs} is relative permeability of the sample. Other geometrical parameters are depicted in Fig. 2.6. (2.7) is further simplified to

$$L_s = \frac{\mu_0}{2\pi}\left[h\left(\mu_{rs}-1\right)\ln\left(\frac{c}{b}\right) + h_0\ln\left(\frac{e}{a}\right)\right]. \tag{2.8}$$

Solving (2.8) in terms of μ_{rs} gives

$$\mu_{rs} = \frac{2\pi\left(L_s - L_e\right)}{\mu_0 h\ln\left(c/b\right)} + 1, \tag{2.9}$$

where $L_e = \frac{\mu_0}{2\pi}h_0\ln\left(\frac{e}{a}\right)$, the self-inductance of an empty test cell (i.e., without the sample). The measurement of L_e is a part of calibration process. Next, L_s in (2.9) can be expressed by the measured impedance Z_s in (2.2):

$$L_s = \frac{Z_s}{j\omega}, \tag{2.10}$$

where L_s is a complex number considering the loss factor due to the conductance, G_s. Substituting (2.10) into (2.9) provides

$$\mu_{rs} = \frac{2\pi\left(Z_s - j\omega L_e\right)}{j\omega\mu_0 h\ln\left(c/b\right)} + 1. \tag{2.11}$$

Using the described procedure, μ_{rs} of the NiZn-PDMS composite (same to the ε_{rs} measurement example) was characterized and the results are shown in Fig. 2.7. Stable responses of $\mu'_{rs} \approx 4.3$ and $\mu''_{rs} \approx 0.03$ are presented at low frequencies. The peak at

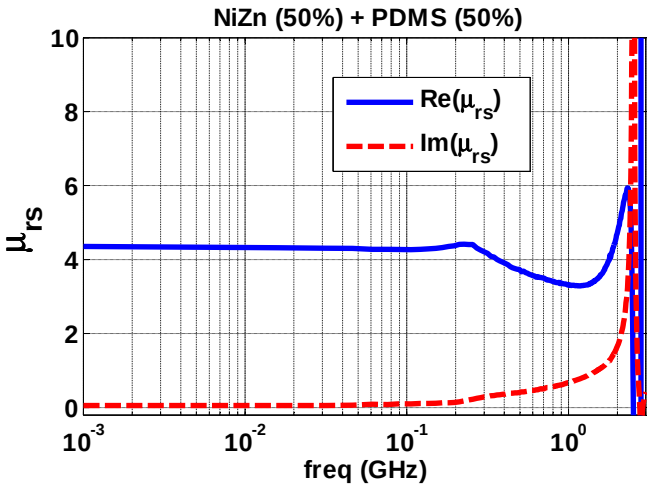

Figure 2.7: Permeability of NiZn-PDMS composite measured with Agilent E4991A impedance analyzer.

240 MHz corresponds to the domain wall resonance of the NiZn ferrite. However, the peak around 2.4 GHz originated from the resonance of parasitic C and the sample's L. Although this resonance is located at 2.4 GHz, the measured results are started to diverge from 1 GHz.

2.2.3 Limitation of C/L Method

Besides the operation frequency limit demonstrated along with the ε and μ measurement examples, the C/L method have the following limitations:

1. Two separate measurement set-ups and de-embedding processes are required to characterize ε and μ. Therefore, the C/L method is rather complicated to characterize materials having both non-trivial ε and μ (e.g., magneto-dielectrics, ferrites, etc.).

2. Inhomogeneous composites cannot be characterized. For example, the effective (or homogenized) ε and μ of a patterned composite (see Fig. 1.1) can be characterized by uniformly illuminating the composite with electromagnetic fields. This cannot be achieved by locally applying the fields as in the C/L method configurations.

3. It is not feasible to characterize a composite with metallic inclusions. As the electrodes are highly conductive, placing the electrodes forms a shorted circuit if the sample is also conductive or has metallic inclusions.

4. Another shortcoming of the C/L method can be its laborious sample preparation process. The sample needs to be tailored in two different shapes (e.g., thin plate and toroidal core). This can be troublesome for hard samples, as special tools (e.g., diamond or water jet cutter) must be used.

2.3 Resonant Method for Narrow Bandwidth

For this method, a material sample is inserted in a resonant structure [33–37]. Subsequently, the real and imaginary components of ε or μ of the sample are de-embedded from the measured resonant frequency (f_r) and quality factor (Q). The resonant method has a very high sensitivity as the electromagnetic waves interact with the sample multiple times inside the resonant structure. For example, one of the resonant method developed in Electroscience Laboratory [38] measured the uniaxial-anisotropic properties of a rutile (TiO_2) sample with accuracy of 4 digits in the permittivity and loss tangent. The cost of the high sensitivity is the narrow operation bandwidth. Only sample properties in the vicinity of the resonant frequency can be

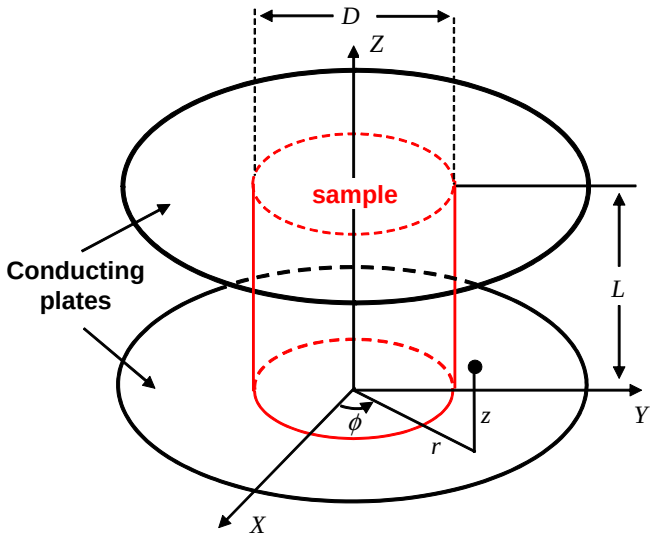

Figure 2.8: Illustration of the Courtney resonator.

obtained. Therefore, the resonant method is not available to provide information on how the material properties vary with frequency.

2.3.1 De-embedding of Material Properties

Fig. 2.8 shows a typical measurement set-up for the resonant method. The sample is sandwiched between two conducting plates and it serves as a key part of the resonator. This configuration is often called "Courtney resonator" after his pioneering work [35]. There are other types of resonators such as coaxial resonators [39] and split resonators [40] developed to reduce the cavity size and to characterize thin samples. As de-embedding procedures of other resonant methods do not differ much from Courtney's work, in this section, we mainly discuss the calculations of sample properties from the measured responses in the Courtney resonator (i.e., a cylindrical cavity) [33, 35, 36].

As mentioned, the permittivity (or permeability) and loss tangents of the sample are de-embedded from the measurement of resonant frequency (f_r) and quality factor (Q) in the resonant method. These parameters are commonly measured with the TE_{011} mode. With the TE_{011} mode, the effects from the air gaps between the sample and the conducting plates are negligible since the fields tend to be zero at these points. Moreover, compared to other modes, it is easier to identify the resonant peak [19]. Herein, we consider the de-embedding of ε_{rs} and $\tan\delta_\varepsilon$ for a non-magnetic material (i.e., $\mu_{rs} = 1$). The de-embedding of magnetic properties is also available using the TE_{011} mode [33, 35] but not discussed in here. Assuming the conducting plates are infinitely large, the analytical form of the characteristic equation for the TE_{011} mode is given by [36]

$$\left[\frac{\varepsilon_{rs}J_0'(\alpha)}{\alpha J_0(\alpha)} + \frac{K_0'(\beta)}{\beta K_0(\beta)}\right]\left[\frac{J_0'(\alpha)}{\alpha J_0(\alpha)} + \frac{K_0'(\beta)}{K_0(\beta)}\right] = 0, \tag{2.12}$$

where

$$\alpha = \frac{\pi D}{\lambda}\sqrt{\varepsilon_{rs} - (\lambda/2L)^2}, \tag{2.13}$$

$$\beta = \frac{\pi D}{\lambda}\sqrt{(\lambda/2L)^2 - 1}, \tag{2.14}$$

$J_0(\alpha)$ and $K_0(\beta)$ are Bessel functions of the first and second kind. λ is a wavelength in the free-space. D and L are indicated in Fig. 2.8. From (2.13) and (2.14), ε_{rs} is calculated by

$$\varepsilon_{rs} = 1 + \left(\frac{c}{\pi D f_r}\right)^2 \left(\alpha_1^2 + \beta_1^2\right), \tag{2.15}$$

where α_1 and β_1 are the first roots of (2.12). As in (2.15), the permittivity of the sample can be calculated from the measured f_r.

For the calculation of $\tan\delta_\varepsilon$, Q of the resonator must be measured. Q of any resonant structure refers to the ratio of the maximum stored energy to the energy

lost in a cycle. Since we already have a solution for ε_{rs} referring to the stored energy, $\tan\delta_\varepsilon$ can be obtained by counting on the energy loss in the resonator. Losses may occur due to the dielectric loss inside the sample and the conduction loss at the plates. The derivations of each loss term are given in [33]. We only provide the result of $\tan\delta_\varepsilon$ as below:

$$\tan\delta_\varepsilon = \frac{A}{Q_0} - BR_s, \tag{2.16}$$

where

$$\begin{aligned}
A &= 1 + W/\varepsilon_{rs}, \\
B &= \frac{1+W}{30\pi^2\varepsilon_{rs}}\left(\frac{\lambda}{2L}\right)^3, \\
W &= \frac{J_1^2(\alpha_1)}{K_1^2(\beta_1)}\frac{K_0(\beta_1)K_2(\beta_1) - K_1^2(\beta_1)}{J_1^2(\alpha 1) - J_0(\alpha_1)J_2(\alpha_1)}, \\
R_s &= \sqrt{\frac{\pi f_r \mu}{\sigma}}
\end{aligned}$$

In the above formulae, σ is the conductivity of the plates and Q_0 is the quality factor in the absence of sample. The equations for W and R_s correspond to the ratio of stored energy inside/outside the sample and the surface resistivity of the conducting plates.

2.3.2 Limitation of Resonant Method

The typical error in the resonant method is less than 1% for ε_r and 0.3% for $\tan\delta_\varepsilon$ characterization. Especially for the loss measurement, a resolution of the order of 10^{-5} can be achieved if a resonator with high Q is used [24]. In spite of its accuracy, the resonant method has several limitations:

1. Such high accuracy fails for high-loss materials as the resonant peak broadens as the loss increases.

2. Closed resonators are not appropriate to measure the material properties under extraordinary environment such as high temperature.

3. The de-embedding process is rather complicate since the wave equations must be solved with the boundary conditions each time. Furthermore, the solutions usually contain complicate harmonic functions (e.g., Bessel functions) that may cost extra computing effort.

4. More than anything else, the resonant method is impossible to measure the material properties as a continuous function of frequency. For a material used in wide-band applications, the characterization of frequency dependent properties is critical. Broader bandwidth characterization may be possible by preparing different sizes of resonators and samples that cover different frequency ranges, however, such effort seems impractical.

2.4 Broadband Transmission/Reflection Method

Broadband characterization is typically carried out using the transmission/reflection (T/R) method. In this case, the material properties are calculated from the measured transmission (S_{21}) and/or reflection (S_{11}) coefficients when the material is inserted into a transmission line (tx-line). Thus, the method is inherently broadband as long as the associated tx-line supports broadband propagation. The T/R method was first articulated by Nicolson and Ross [16] in 1970. Since then, numerous techniques with different tx-line structures have been developed for different purposes.

To carry out accurate characterizations using T/R-based methods, it is necessary to design an appropriate tx-line fixture that accommodates the size and shape of the sample as well as the electrical properties and frequency of interest. Although

there is a variety of measurement fixtures developed for different materials, they can be categorized mainly to two groups, as illustrated in Fig. 2.9(a) and (b). Type-I [18, 41–43] represents the measurement set-up when the surface of the sample is facing the direction of wave propagation. This implies the broadside S-parameters are measured along the short length of the sample [see the inset in Fig. 2.9(a)]. On the other hand, the Type-II methods [26, 44–47] often incorporate conformal tx-lines and the S-parameters are measured along the larger length of the sample. As can be seen in Fig. 2.9(a), the cross-sections of the Type-I methods are completely filled with the sample. With such configurations, material properties of the sample can be directly calculated from the measured S-parameters using the well-known Nicolson-Ross-Weir (NRW) de-embedding process [16, 17]. However for Type-II methods, a secondary de-embedding process is needed to separate the sample property itself from the surrounding effects, since the NRW process does not yield the properties of the sample as the tx-line cross-section is a combination of sample-air-substrate, as depicted in Fig. 2.9(b). Although the de-embedding process is more complicated, Type-II is known to provide more accurate results for thin material characterization. 2.9(b). The above comparisons between Type-I and Type-II T/R methods are summarized in Table 2.1.

Four material characterization techniques discussed in this dissertation all utilize either Type-I or Type-II T/R method. Indeed, since our primary focus is broadband characterization, the T/R method is the only choice among various material characterization techniques. Moreover, a vast selection of tx-line offers the characterization of material samples with arbitrary shapes (e.g., bulk or film) and properties (e.g., dielectric, magnetic, conductive, etc.). Although techniques incorporating with different

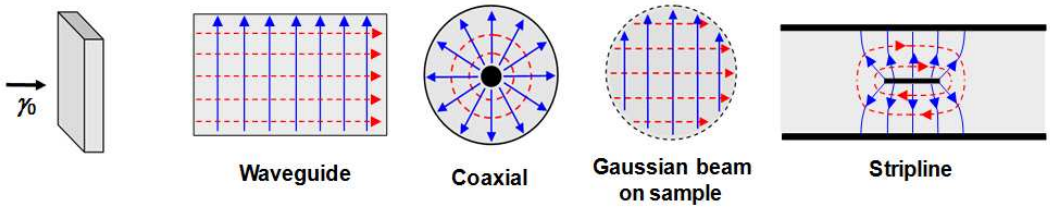

(a)

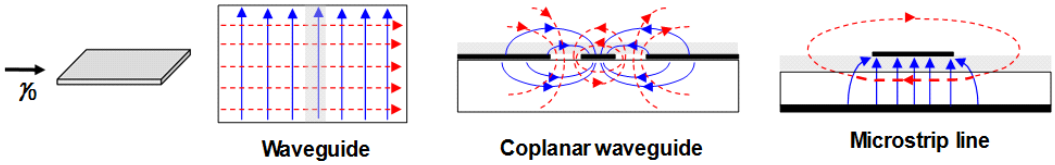

(b)

Figure 2.9: Examples of transmission/reflection methods: (a) Type-I and (b) Type-II. The insets to the left show the orientation of the sample against the direction of wave propagation. The dashed and solid lines refer to magnetic and electric fields. The shaded regions indicate the sample under test.

Table 2.1: Comparison of Type-I and Type-II T/R

Type-I T/R Method	Type-II T/R Method
• Wave propagates along the thickness of the sample. • Sample completely fills the tx-line cross-section. • Rather large and thick sample is required. • Properties directly de-embedded from the NRW equations.	• Wave propagates along the surface of the sample. • Sample partially fills the tx-line cross-section. • Available for small and thin sample characterization. • Need a secondary de-embedding process.

tx-lines have their own uniqueness, they share the same theory for the de-embedding process which is described in the next section.

2.4.1 De-embedding of Material Properties

For the T/R method, it is not necessary to solve the wave equations accounting for boundary conditions of the associated tx-line. We can rely on the more convenient and commonly used tx-line parameters: impedance and S-parameters. The calculation of ε and μ from the measured impedance and S-parameters can be found elsewhere [16–18]. In this section, we re-derive the equations by taking into account tx-line structural effects. The latter refers to any effect that differ the wave propagation in tx-line from the free-space propagation. They are assumed to be identical in most previously reported derivations. However, this assumption may not hold for general tx-lines affected by parasitic elements and dispersive characteristics.

Fig. 2.10 shows a general T/R method set-up. In the figure, a sample of thickness t is completely filling the cross-section of the tx-line. We assume two ports are matched after calibration, and thus there is no reflection at ports. The incident wave is from the left of the sample implying only forwarding wave exists in region III. Γ and τ refer to the elementary reflection coefficient and the propagating factor in the sample thickness, respectively. Otherwise, S_{11} and S_{21} are the resultant of multiple reflections and transmissions inside the sample. We also assume the tx-line and the sample are reciprocal, that is $S_{21} = S_{12}$.

With the above set-up, the sample's relative permittivity (ε_{rs}) and relative permeability (μ_{rs}) can be expressed with other parameters (Γ, τ,γ_e, and γ_s). The wave propagation constant in the empty tx-line section (γ_e) and the section filled with the

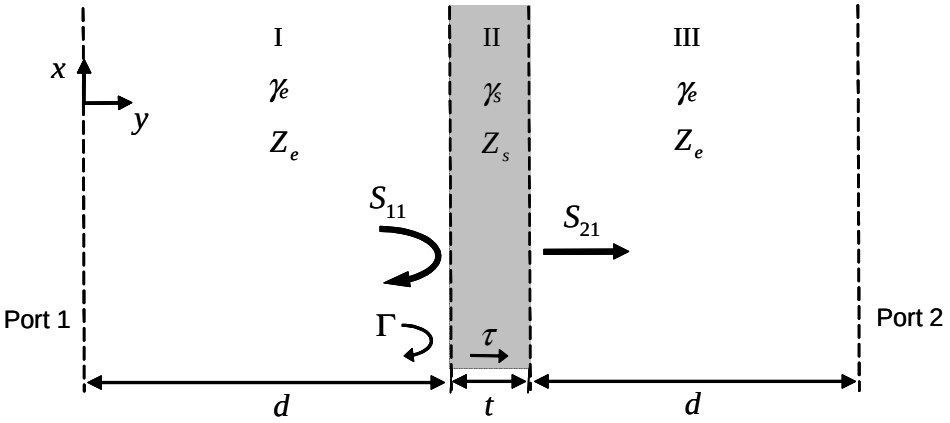

Figure 2.10: A general illustration of the T/R method set-up.

sample (γ_s) are given by

$$\gamma_e = jk_0\sqrt{\mu_{re}\varepsilon_{re}}, \tag{2.17}$$

$$\gamma_s = jk_0\sqrt{\mu_{rs}\varepsilon_{rs}}, \tag{2.18}$$

where k_0 is the wave propagation constant in the free-space. Assuming the transverse electromagnetic (TEM) wave propagation, the characteristic impedances for the empty and sample sections are given by

$$Z_e = \frac{j\omega\mu_0\mu_{re}}{\gamma_e} = \frac{\gamma_e}{j\omega\varepsilon_0\varepsilon_{re}}, \tag{2.19}$$

$$Z_s = \frac{j\omega\mu_0\mu_{rs}}{\gamma_s} = \frac{\gamma_s}{j\omega\varepsilon_0\varepsilon_{rs}}, \tag{2.20}$$

Γ is determined from the above impedances as

$$\Gamma = \frac{Z_s - Z_e}{Z_s + Z_e}. \tag{2.21}$$

Also, τ is expressed by

$$\tau = \exp\left(-\gamma_s t\right). \tag{2.22}$$

μ_{rs} and ε_{rs} can be solved by substituting (2.19) and (2.20) into (2.21):

$$\mu_{rs} = \frac{\gamma_s}{\gamma_e}\frac{1+\Gamma}{1-\Gamma}\mu_{re}, \tag{2.23}$$

$$\varepsilon_{rs} = \frac{\gamma_s}{\gamma_e}\frac{1-\Gamma}{1+\Gamma}\varepsilon_{re}. \tag{2.24}$$

(2.23) and (2.24) are identical to the well-known Nicolson-Ross-Weir (NRW) equations [16, 17] except for the presence of μ_{re} and ε_{re}. Usually, $\mu_{re} = \varepsilon_{re} = 1$ (i.e., $\gamma_e = k_0$) is assumed in most de-embedding techniques, however, in reality, this may not be true because of the structural effects in the employed tx-line. For example, a stripline [see Fig. 2.9(a)] has fringing capacitances occurring between corners of the center conductor and the adjacent grounds that contribute to $\varepsilon_{re} \neq 1$. That is, ε_{re} may vary with the thickness and width values of the center conductor [48]. Fringing inductances, however, are usually neglected for tx-lines with a closed structure or with a sufficiently large ground planes. Therefore, we will continue to derive the equations with the assumption that $\mu_{re} = 1$. Then, (2.23) and (2.24) can be rewritten by

$$\mu_{rs} = \frac{\gamma_s}{\gamma_e}\frac{1+\Gamma}{1-\Gamma}, \tag{2.25}$$

$$\varepsilon_{rs} = -\frac{\gamma_e\gamma_s}{k_0^2}\frac{1-\Gamma}{1+\Gamma}. \tag{2.26}$$

Since γ_s is defined by the multiplication of μ_{rs} and ε_{rs} as in (2.18), direct calculation of μ_{rs} and ε_{rs} from (2.25) and (2.26) may exhibit wrong signs or may be swept to each other. To avoid these ambiguities, impedance (z) and refractive index (n) are defined by

$$z = \sqrt{\frac{\mu_{rs}}{\varepsilon_{rs}}}, \tag{2.27}$$

$$n = \sqrt{\mu_{rs}\varepsilon_{rs}}. \tag{2.28}$$

Substituting (2.25) and (2.26) into (2.27) and (2.28) yields

$$z = \pm j \frac{k_0}{\gamma_e} \left(\frac{1+\Gamma}{1-\Gamma} \right), \tag{2.29}$$

$$n = \pm j \frac{\gamma_s}{k_0}. \tag{2.30}$$

For a passive medium, the signs in (2.29) and (2.30) must be chosen to satisfy

$$\mathrm{Re}\{z\} \geq 0, \tag{2.31}$$

$$\mathrm{Im}\{n\} \geq 0. \tag{2.32}$$

To solve z and n (or $\varepsilon_{rs} = n/z$ and $\mu_{rs} = nz$) from (2.29) and (2.30) together with (2.31) and (2.32), the three unknowns (Γ , γ_s, γ_e) must be determined from three S-parameter measurements. Therefore, it is necessary to express these unknowns in terms of the measured S-parameters. This process is described below.

Firtly, we can calculate the analytical solutions of S_{11} and S_{21} (with the presence of the sample) by solving a simple 1-D boundary problem. Let us go back to the problem set-up as in Fig. 2.10. We can write general solutions of the E-fields at region I, II and III in terms of forward and backward waves. That is,

$$E_I = \exp(-\gamma_e z) + C_1 \exp(\gamma_e z), \tag{2.33}$$

$$E_{II} = C_2 \exp(-\gamma_s z) + C_3 \exp(\gamma_s z), \tag{2.34}$$

$$E_{III} = C_4 \exp(-\gamma_e z) + C_5 \exp(\gamma_e z), \tag{2.35}$$

where C_i are the coefficients determined by solving the boundary condition equations based on the continuity of the tangential E- and H-field. The details of calculating C_i can be found in most basic electromagnetic books [49]. In particular, we are interested in the solutions of C_1 and C_4 corresponding to S_{11} and S_{21}, respectively. They are

given by

$$S_{11}(=C_1) = \left[\frac{\Gamma\left(1-\tau^2\right)}{1-\Gamma^2\tau^2}\right], \tag{2.36}$$

$$S_{21}(=C_4) = \left[\frac{\tau\left(1-\Gamma^2\right)}{1-\Gamma^2\tau^2}\right], \tag{2.37}$$

$$\text{where } \tau = \exp\left(-\gamma_s t\right). \tag{2.38}$$

From (2.36) and (2.37), Γ and τ can be solved if the measured S_{11} and S_{21} provided. Nicolson, Ross, and later Weir [16,17] have provided closed-form expressions of Γ and τ in terms of S_{11} and S_{21}. They introduced new variables to pursue mathematical simplicity as below:

$$X = \frac{1-V_1V_2}{V_1-V_2}, \tag{2.39}$$

$$\text{where } V_1 = S_{21} + S_{11}, \tag{2.40}$$

$$V_2 = S_{21} - S_{11}. \tag{2.41}$$

Substituting (2.40) and (2.41) into (2.39) yields

$$X = \frac{1-S_{21}^2+S_{11}^2}{2S_{11}}. \tag{2.42}$$

Also, substituting (2.36) and (2.37) into (2.42) gives

$$X = \frac{1+\Gamma^2}{2\Gamma}. \tag{2.43}$$

From (2.43), Γ, one of the three unknowns in (2.29) and (2.30), is obtained by

$$\Gamma = X \pm \sqrt{X^2-1}. \tag{2.44}$$

The sign in (2.44) is properly chosen so that $|\Gamma| < 1$. With the determined Γ, τ is calculated by

$$\tau = \frac{V_1-\Gamma}{1-V_1\Gamma} = \frac{S_{11}+S_{21}-\Gamma}{1-\left(S_{11}+S_{21}\right)\Gamma}. \tag{2.45}$$

With the knowledge of τ, the second unknown γ_s can be calculated from (2.38) as

$$\gamma_s = \frac{1}{t}\left[\ln\left|\frac{1}{\tau}\right| + j\left(2\pi m + \phi\right)\right], \tag{2.46}$$

where ϕ is the phase of $1/\tau$ and $m = 0, \pm1, \pm2, \cdots$. It is necessary to choose proper m to resolve the phase ambiguity originated from more than 2π phase differences between the actual and calculated τ. This occurs when the thickness of the sample is more than half of the wavelength (in material). To this end, the last unknown remained is γ_e, which can be obtained from the measurement of the empty tx-line (S_{21}^e). The analytical solution for S_{21}^e is given by

$$S_{21}^e = \exp\left[-\gamma_e\left(2d + t\right)\right], \tag{2.47}$$

where d is the distance from the sample surface to the tx-line ports, as indicated in Fig. 2.10. Solving (2.47) for γ_e provides

$$\gamma_e = \frac{1}{2d + t}\left[\ln\left|\frac{1}{S_{21}^e}\right| + j\left(2\pi n + \phi_e\right)\right]. \tag{2.48}$$

Similar to (2.46), ϕ_e is the phase of $1/S_{21}^e$ and n is an integer that needs to be chosen properly. The lengthy derivation of the de-embedding process for T/R method can be summarized as below:

1. Measure three S-parameters (S_{11} and S_{21} with the sample, and S_{21}^e without the sample).

2. Calculate three unknowns (Γ , γ_s, γ_e) from (2.44), (2.46), and (2.48).

3. Calculate z and n from (2.29)-(2.32).

4. Sample's permittivity and permeability are obtained by $\varepsilon_{rs} = n/z$ and $\mu_{rs} = nz$.

To examine the benefit of considering the structural effects, the S-parameters of a dielectric slab were measured and its permittivity was de-embedded using the above procedure under two different assumptions: $\gamma_e = k_0$ and $\gamma_e \neq k_0$. The former assumes there is no structural effect so that the wave propagation constant in the tx-line is identical to the one in the free-space. On the other hand, the latter calculate γ_e from the measured S_{21}^e, as in (2.48), and then used in the de-embedding process. Fig. 2.11 shows the comparison of the de-embedded permittivities for each case. The sample was a dielectric slab with a known permittivity of $\varepsilon_{rs} = 9$. The tx-line used in this example was a tapered stripline introduced in Chapter 4. As can be seen, the de-embedded ε_{rs} diverges more from the known value when $\gamma_e = k_0$ is used. Specifically, the maximum error decreases from 3.9% to 2.7% by using the measured γ_e. This is because k_0 is smaller than the actual propagation constant, implying that the effective thickness of the sample is over-estimated due to the structural effect in the stripline.

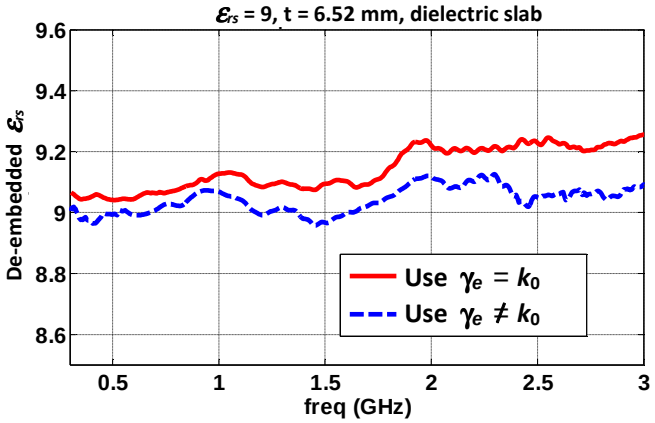

Figure 2.11: De-embedded permittivity of $\varepsilon_{rs} = 9$ dielectric slab.

2.4.2 Limitations of T/R Method

Although the T/R method has advantages such as the broadband operation, simultaneous ε and μ characterization, simple de-embedding steps, and vast diversity in measurement set-ups, several limitations can be listed as follows:

1. General error rates of the T/R method are $< 5\%$ for ε (or μ) and $< 10\%$ for tanδ, which are much higher than the resonant method. This is because the measured quantities in the T/R method (voltage ratios) is not as sensitive as those in the resonant method (frequency, Q-factor). Typically for the loss chracterization, higher error values are often resulted due to the uncertainty in the phase data of measured S-parameters. Also, during the propagation inside the tx-line fixture, there can be attenuation by conduction loss, radiation loss, etc. It has been reported that the resolution of loss tangent measurement is approximately ± 0.01 for the T/R method [24]. Therefore, a material with tan$\delta < 0.01$ is not characterizable.

2. As observed in (2.29)-(2.30), (2.44), (2.46), and (2.48), the signs and orders must be carefully chosen to avoid phase wrapping that leads to non-unique retrieval of material parameters. Such uncertainty is predominant when the sample thickness is integer multiples of one-half of the guided wavelength. To circumvent this problem, the use of an iterative solver [18], the Kramer-Kronig relations [50], transmission-only measurements [51] can be considered.

3. The propagation of higher order modes limits the operation frequency range. As the higher order modes contain longitudinal field components, sudden peaks

are manifest when these fields are resonating along the length of the tx-line. We investigate this problem in Chapter 4.

4. Air gaps between the sample and the body of the tx-line generate erroneous results. Such error is also related to the excitation of higher order modes. The impact of the air gaps is more serious at the higher frequency where the wavelength becomes comparable to the gap dimension.

2.5 Summary

Starting from the definition and basic considerations of material characterization, in this chapter, we reviewed three major material characterization techniques. The fundamental theories behind each technique were described, and their benefits and shortcomings were discussed. Based on this review, one may be able to select the most appropriate technique for a given material sample and testing purpose. In our case, we proceeded to use the T/R method to realize broadband characterization of engineered composites. The development of four T/R techniques will be illustrated in the following chapters.

Chapter 3

SYNTHETIC GAUSSIAN BEAM METHOD FOR MULTI-LAYER COMPOSITES

In this chapter, a new free-space measurement approach is presented to characterize RF materials and metamaterials over a wide frequency range. In contrast to the traditional spot-focused horn pair system, the proposed technique generates a Gaussian beam with a tight spot, focused on a sample under test via a synthesis using individually measured responses. Therefore, difficulties in fabricating lenses for the conventional spot-focused horn pair are avoided. We validate the proposed technique by de-embedding the permittivity of a known dielectric slab, and subsequently proceed to characterize the transmission properties of metamaterial assembly. The proposed technique can be adapted for measurements in EM facilities using spherical or planar scanning capability.

3.1 Introduction

Non-invasive characterization of materials has drawn renewed attention for composites with novel dispersion properties. For the composite such as metamaterials constructed from a periodic repetition of layered structures must be tested non-invasively as the supported modes are highly sensitive to external perturbation. Therefore, the

usual resonant cavity method cannot be used as it requires invasive reshaping of the sample for insertion into the measurement fixture. Also, the cavity's measurement bandwidth is restricted by the cavity's resonant frequency. Alternatively, the T/R method does offer broader bandwidth. However, a tx-line fixture must be carefully chosen to avoid invasive measurement configuration. For example, placing a metallic probe over the metamaterials [52] or inserting the metamaterials into metallic waveguides [18] is not permissible. Free-space measurement (FSM) methods [41, 53–56] are therefore best for metamaterials due to their non-invasive nature and wideband operation. FSM is one of the T/R characterization techniques that de-embed material properties from the measured S-parameters between two antennas with the sample placed in the line of sight. That is, instead of using invasive closed structures (such as waveguides), FSM employs free-space as the transmitting channel.

Typically, an FSM measurement set-up consists of a horn pair corrected by dielectric lenses placed over their apertures. In this manner, a common focal point at the sample's surface is configured as in Fig. 3.1(a). That is, the field radiated by the transmitting horn forms a collimated Gaussian beam via the lens that concurrently suppresses diffraction from the sample edges. Also, since the wavefronts are nearly planar throughout the sample, the simple plane-wave transmission/reflection process can be used to de-embed the material properties [41, 53, 54]. This antenna-lens system has also been used in conjunction with time domain spectroscopy for wide band material characterization [55, 56].

However, the lenses used in the conventional system require precise manufacturing and alignment to reduce wavefront aberrations. If the lenses are not aligned precisely at the horizontal axis, the generated Gaussian beam severely suffers from

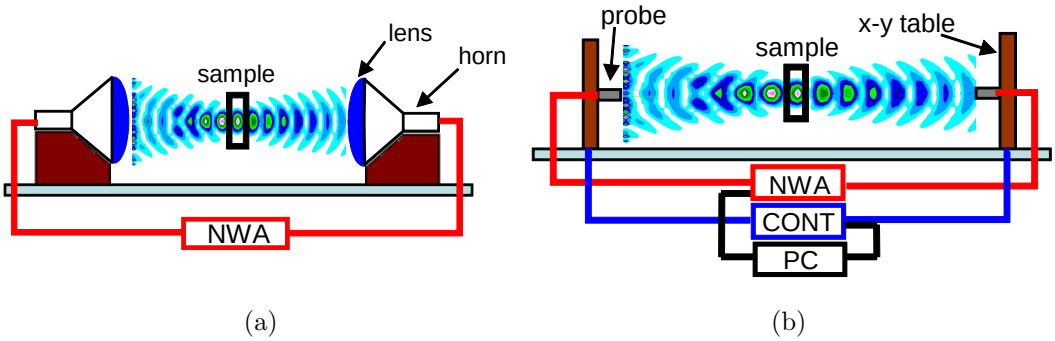

(a) (b)

Figure 3.1: Illustration of the traditional and proposed free-space measurement systems: (a) Traditional spot-focused horn pair with lenses, (b) proposed synthetic aperture system with planar scanning x-y tables. The abbreviations NWA, CONT, and PC refer to network analyzer, controller, and personal computer, respectively.

wavefront aberrations. Also, the lenses are often required to built with multiple coating layers to minimize reflections at the lens-air boundaries. This makes the lenses quite costly, and placing stringent limits on the bandwidth of the overall system. A wideband characterization would also be rather costly as multiple lenses must be custom-manufactured for each frequency band. Furthermore, the lens must necessarily increase in size as frequency decreases, creating additional difficulties on low frequency implementations.

As an alternative, herewith we propose a new technique utilizing synthetic aperture concepts. That is, the beam impinging on the sample is synthetically collimated by post-processing a set of individual measurement responses over a desired virtual aperture. Our proposed synthetic FSM system is illustrated in Fig. 3.1(b). As depicted, S-parameters are measured for each probe location and stored. Subsequently, the Gaussian beam is synthesized with appropriate weighting of each detected signal.

As this process emulates the presence of a large Gaussian distributed aperture, difficulties associated with a large lens are avoided. Below, we demonstrate the proposed technique by using both planar and spherical scanning setups. In particular, a linear x - y table and a spherical scanning rotator are used for this purpose in the anechoic chamber.

3.2 Synthesis of the Virtual Gaussian Aperture

The difficulties in implementing a large physical aperture can be avoided by synthesizing an equivalent virtual surface. Much like a synthetic aperture radar process, a large number of signals are subsequently and coherently summed to produce a signal comparable to the one generated by a large physical aperture. Moreover, the field distribution of such a virtual aperture can be adjusted by weighting the collected signals [57]. Herewith, our goal is to synthesize the Gaussian beam for the FSM method. As depicted in Fig. 3.2(a) and (b), the Gaussian beam is realized by moving a transmitting probe across a planar or spherical aperture and weighting the detected probe field. For experimental realization of the Gaussian beam synthesis in a manner that yields a focused illumination on the sample surface, it is critical to define proper weighting values, spot size, scanning dimensions (i.e., the virtual aperture size), and number of a grid points. These parameters are analogue to the parameters in the extensively studied Gaussian beam theory for optical systems.

Let us first consider the complex weighting at each probe location. Referring to Fig. 3.3, to form a Gaussian beam, the weight value U must take the following form [58]:

$$U(\vec{r}) = \frac{1}{jz_0}\frac{W_0}{W(z)}\exp\left[-\frac{\rho^2}{W^2(z)}\right]\exp\left[-jkz - jk\frac{\rho^2}{2R(z)} + j\zeta(z)\right], \tag{3.1}$$

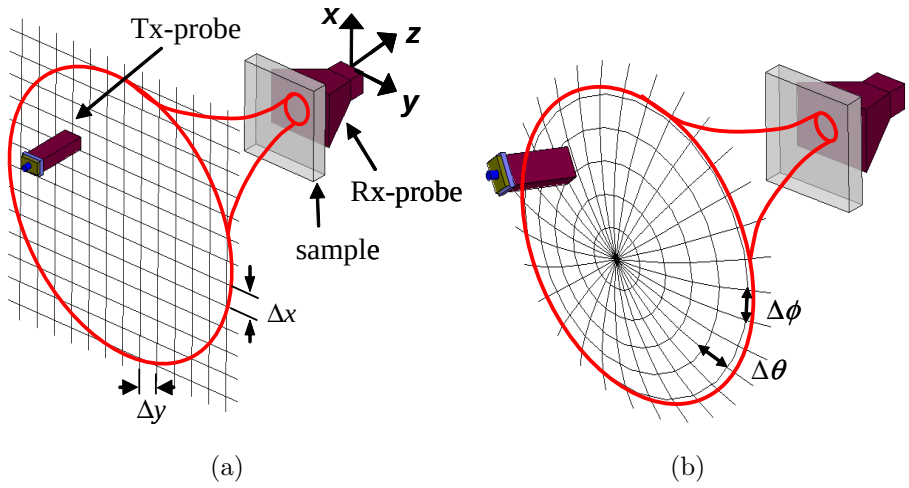

Figure 3.2: Different scanning methods: (a) planar and (b) spherical.

where

k = wave number;

ρ^2 = $x^2 + y^2$;

W_0 = waist;

z_0 = depth of focus = $\pi {W_0}^2/\lambda$;

$W(z)$= beamwidth forming the 86% power envelope = $W_0\,[1 + (z/z_0)^2]^{1/2}$;

$R(z)$ = curvature raadius = $z\,[1 + (z_0/z)^2]$;

$\zeta(z)$ = Guoy phase = $\tan^{-1}(z/z_0)$.

The first (real) exponential term in (3.1) describes a non-uniform amplitude distribution, implying strong field close to the propagation axis with rapid decay away from the *waist*. The second (complex) exponential term in (3.1) defines the phase progression in the form of a plane wave corrected by a slowly varying Guoy phase and

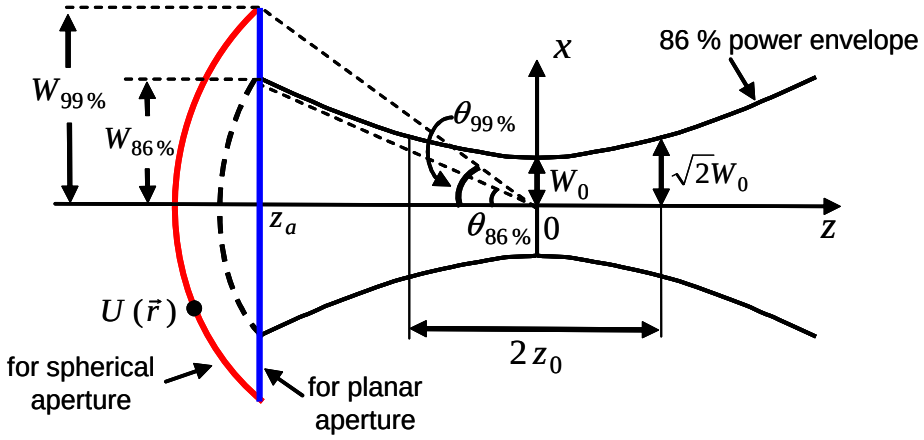

Figure 3.3: Gaussian beam profile. $U(\vec{r})$: Complex amplitude, W_0: Beam waist, z_0: Depth of focus, W: Beamwidth, θ: Divergence angle.

a spherical wave front phase factor. The wavefront is almost planar at the *waist*, and diverges as the beam moves away from the *waist* to eventually resemble a spherical wave at the far-field ($z >> z_0$). Accordingly, the *waist* is the desired sample location for an FSM system as the collimated beam illuminates a finite sample with nearly planar wavefront but without seeing the edges. A narrower waist size is certainly preferred. However, the paraxial beam approximation (inherited to the Gaussian beam) implies the waist size should be larger than (or equal to) a wavelength. Thus, we will use $W_0 = \lambda$ throughout this paper. With this waist size, the scanning area on the planar or spherical surface must be defined large enough to avoid artificial diffraction during reconstruction. Specifically, to cover 99% of the total power, a scanning area as large as $2W_{99\%}$ for a planar aperture and $2\theta_{99\%}$ for a spherical aperture must be scanned (see Fig. 3.3). As the aperture is located in the far zone ($z_a >> z_0$), $W_{99\%}$ and $\theta_{99\%}$ can be found from [58]:

$$W_{99\%} = 1.5W_{86\%} \approx 1.5\frac{\lambda}{\pi W_0}z_a \quad \text{(meters)}, \tag{3.2}$$

$$\theta_{99\%} = \tan^{-1}(1.5\tan_{86\%}) \approx \tan^{-1}\left(1.5\frac{\lambda}{\pi W_0}\right) \quad \text{(radian)}. \tag{3.3}$$

From (3.2), $W_{99\%}$ is proportional to z_a implying the measurement range can be a critical restriction for planar virtual aperture realization. However, as the spherical aperture is realized by an angular scan, it is more suited for lower frequencies where space is at a premium. Clearly, both (3.2) and (3.3) must be chosen with respect to the lowest frequency when adapted to wideband measurements. Concurrently, we must scan the defined area with intervals satisfying Nyquist's sampling rate. As the response for each measurement is sampled at discrete locations, the intervals must be sufficiently small to capture the phase variation between two adjacent grid points. Therefore,

$$\Delta x = \Delta y < \frac{\lambda}{2}, \tag{3.4}$$

$$\Delta\theta = \Delta\phi < \frac{\lambda}{2(a+\lambda)}, \tag{3.5}$$

for the planar and spherical apertures, respectively, where a is the maximum radius of the sample under test. Contrary to the scanning area, (3.4) and (3.5) must be chosen with respect to the highest frequency for wideband measurements.

To examine the impact of the above parameters, we simulated the Gaussian beam reconstruction process employing a Hertzian dipole probe as illustrated in Fig. 3.4(a). For this experiment, the Hertzian dipole moved over a planar aperture surface and was weighted with the appropriate Gaussian complex amplitudes. Subsequently, the radiation pattern of each weighted Hertzian dipole was incorporated in the observation domain to demonstrate the overall radiated field. The analytical calculation of the overall E-field from the weighted Hertzian dipole array is described in Appendix A. Fig. 3.4(b) and (c) show the ideal magnitude and constant phase contour plots

of the reconstructed E-field at 10 GHz. For these plots, the proper Gaussian beam reconstruction parameters were used as shown in Table 3.1. As observed in Fig. 3.4(b) and (c), a focused Gaussian beam is reconstructed with a uniform phase distribution at the waist. However, the Gaussian beam reconstruction fails when one of the parameters does not satisfy the recommended conditions. Some of these situations are depicted in Fig. 3.4(d)-(f). That is, if the scanned aperture is reduced from $2W_{99\%}$ to $2W_{67\%}$, artificial diffractions and blurring of the reconstructed spot at $z = 0$ is observed [see Fig. 3.4(d)]. Also, if distance between sample points is doubled from 0.43λ to 0.86λ, the side-lobe amplitudes increase around the aperture plane [see Fig. 3.4(e)]. Further, Fig. 3.4(f) shows that the reconstructed beam is not collimated when the waist size is reduced from λ to 0.5λ.

Table 3.1: Parameters for simulation

Waist (W_0)	Aperture lateral position (z_a)	Aperture transverse dimension ($2W_{99\%} \times 2W_{99\%}$)	Sampling rate ($\Delta x = \Delta y$)
λ	-10λ	$10\lambda \times 10\lambda$	0.43λ

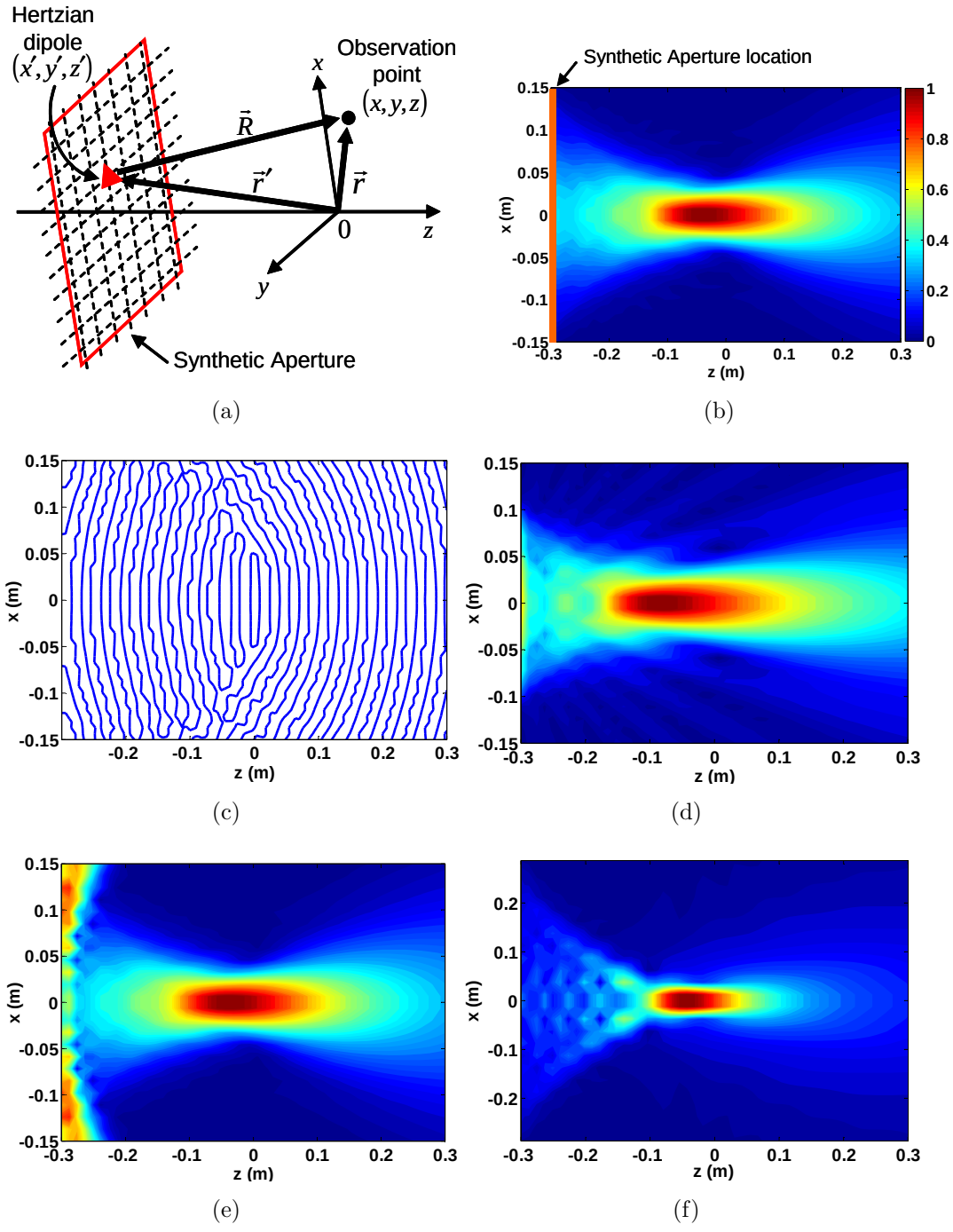

Figure 3.4: Simulated results of synthesized E-field from the weighted Hertzian dipoles: (a) Simulation set-up, (b) magnitude of the desired beam using the parameters in Table 3.1, (c) constant phase contours of the desired beam, (d) magnitude when insufficient scan area is used [$2W_{99\%} \rightarrow 2W_{67\%}$], (e) magnitude when insufficient sampling rate is used [$0.43\lambda \rightarrow 0.86\lambda$], and (f) magnitude when narrower waist is used [$\lambda \rightarrow 0.5\lambda$].

Another simulation study was performed using a full-wave simulation tool (Ansoft HFSS). As in the 3D simulation model depicted in Fig. 3.5, a dielectric slab of $\varepsilon_r = 9$ ($10.6 \times 10.6 \times 0.67$ cm^2) is located at $z = 0$. The Gaussian beam is reconstructed by weighting and adding a bundle of plane waves from different incident angles ($-30° < \theta < 30°$, $-30° < \phi < 30°$ from the z-axis). This process emulates the reconstruction of the spherical virtual aperture. The simulation results are depicted in Fig. 3.5(b) and (c). They are showing the sum of E-field magnitudes inside the simulation domain without and with the Gaussian weighting. For the plot without the Gaussian weighting [Fig. 3.5(b)], strong diffractions at the edges of the sample can be observed. In this case, the half power beamwidth (HPBW) upon the sample surface was computed as 8.6 cm. However, as shown in Fig. 3.5(c), the HPBW was reduced to 3.4 cm by applying Gaussian weights, thereby illuminating the sample with a collimated Gaussian beam. It has been reported that the diffraction effects at the edges of the sample is negligible if the minimum transverse dimension of the sample is greater than 3 times of HPBW [41]. According to this experimental observation, a sample whose dimension is larger than 10.2×10.2 cm^2 can be effectively measured without the diffraction effects. The simulation results shown in Fig. 3.5(c) is the convincing proof of this rule.

3.3 Measurement Process and Set-Up

Assuming that scanning parameters are properly chosen as described in the previous section, we proceed to discuss the measurement process. The overall procedure is described in Fig. 3.6, and refer to the measurement of the transmission coefficient (S_{21}) to be used for determining the unknown material property. Specifically, as a

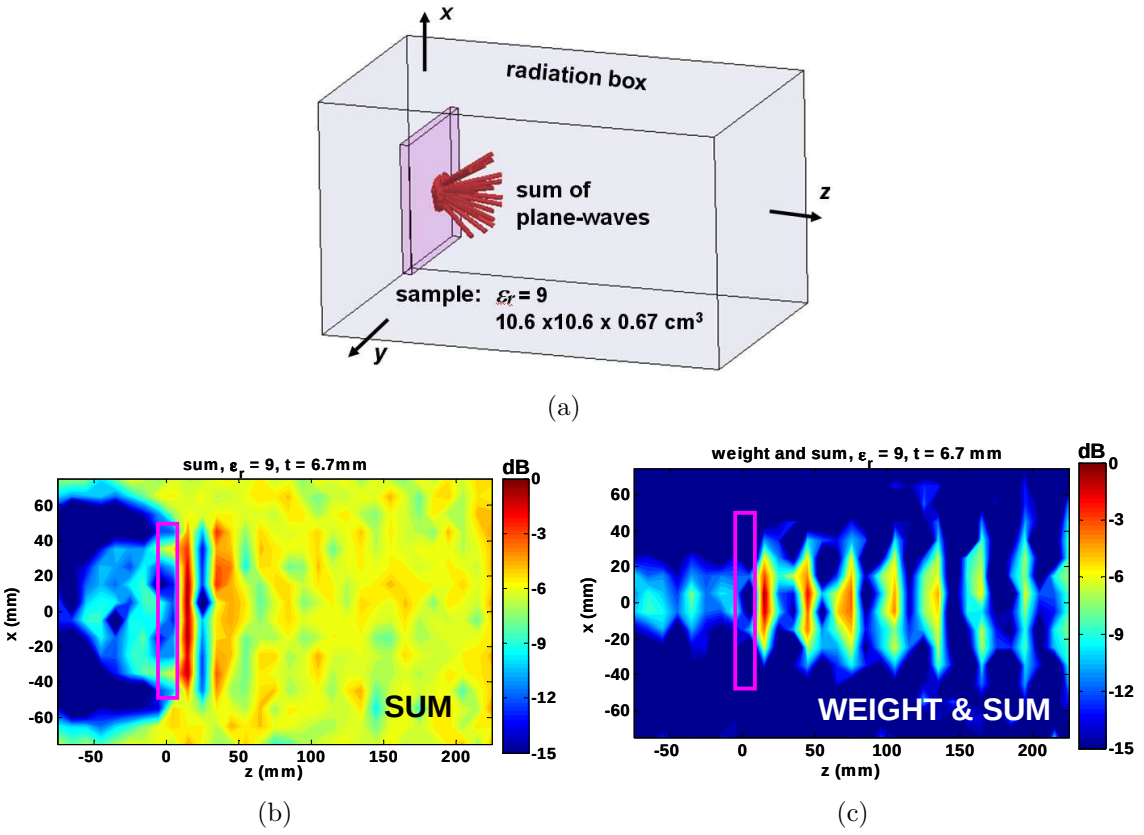

Figure 3.5: Full-wave simulations of Gaussian beam synthesis: (a) problem set-up to generate spherical virtual aperture, (b) E-field magnitude for the sum of plane waves, and (b) E-field magnitude for the sum of weighted plane waves.

first step, the transmitting probe is moved across the designated planar or spherical aperture to generate the synthetic aperture and collect the S_{21}^i values at the ith probe location. As illustrated in Fig. 3.7(a), a planar virtual aperture is realized by moving the transmitting probe across x- and y- directions, while the sample and receiving probe remain stationary. On the other hand, a spherical aperture is formed by simultaneously changing the viewing angles in θ- and ϕ-directions under the consistent plane-wave illumination [see Fig. 3.7(b)]. Although desirable, use of a compact range is not necessary. Indeed, stray reflections coming from nearby structures can

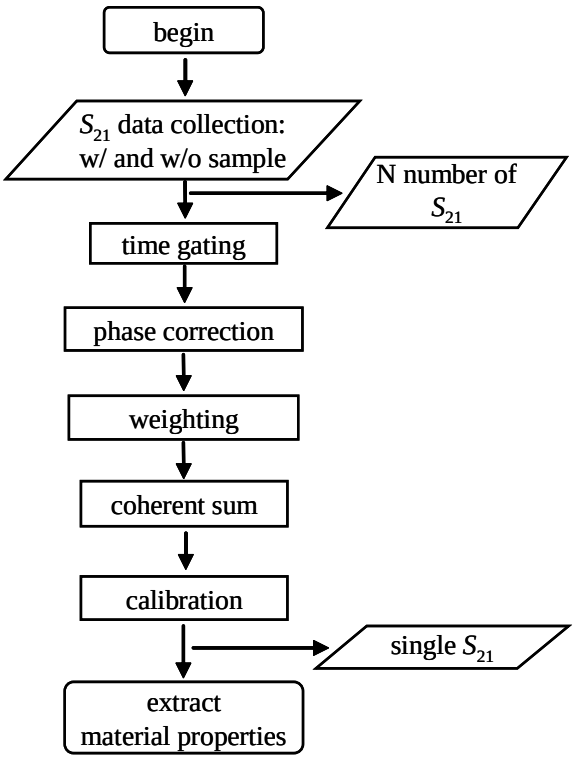

Figure 3.6: Flow chart of the new free-space measurement procedure.

be eliminated via a synthesis process. In the following, we demonstrate the spherical scan system in a compact range only to use the existing scanning hardware in ElectroScience Laboratory (primarily for antenna pattern characterizations).

We remark that for each S_{21}^i measurement, time-domain gating is applied to remove multiple reflections between the receiving probe and sample. Of course, the gating window must also be large enough to allow for complete inclusion of multiple reflections within the sample. Prior to the synthesis of individual responses, phase error correction may also be necessary. These errors are due to positioning uncertainties (during measurement) and misalignments of the scan points. Nevertheless, as noted

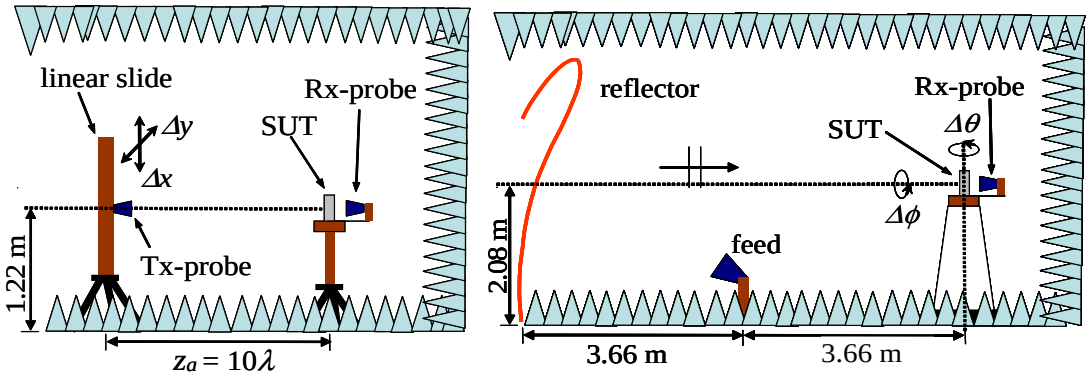

(a) (b)

Figure 3.7: Measurement set-up in the OSU ElectroScience Lab anechoic chamber: (a) Planar and (b) spherical scanning system.

later, the spherical scans had negligible phase errors, and for our measurements, no error correction was required.

The overall (plane wave) transmission coefficient is obtained by weighting and summing the individual S_{21}^i measurements. Referring to Fig. 3.8, the synthesized $S_{21}(S_{21}^{total})$ can be expressed as

$$S_{21}^{total} = \frac{V_2^{total}}{V_1^{total}}, \tag{3.6}$$

where $V_1^{total} = 1/N \sum_{i=1}^{N} V_1^i$ in which V_1^i refers to the probe excitation voltage (at the ith location) and V_2^{total} is the normalized voltage measured at the receiving stationary antenna when all probes are transmitting. Of course

$$S_{21}^i = \frac{V_2^i}{V_1^i}, \tag{3.7}$$

where V_2^i is the measured voltage at the receiving end when only the ith probe is transmitting. To form the Gaussian beam, it is necessary to weight each S_{21}^i with the

complex Gaussian coefficients U^i giving

$$V_2^{total} = \frac{1}{\sum_{i=1}^{N} U^i} \sum_{i=1}^{N} V_2^i U^i = \frac{1}{\sum_{i=1}^{N} U^i} \sum_{i=1}^{N} S_{21}^i V_1^i U^i. \tag{3.8}$$

Assuming that the probe voltages are identical at each probe location (i.e., $V_1^1 = V_1^2 = V_1^3 = \cdots = V_1^N = V_1$), (3.8) simplifies to

$$V_2^{total} = \frac{V_1}{\sum_{i=1}^{N} U^i} \sum_{i=1}^{N} S_{21}^i V_1^i U^i, \tag{3.9}$$

and from (3.6), we get the final (plane wave) transmission coefficient

$$S_{21}^{total} = \frac{V_1}{\sum_{i=1}^{N} U^i} \sum_{i=1}^{N} S_{21}^i U^i. \tag{3.10}$$

The measured S_{21}^{total} data in presence of the sample under test is subsequently normalized by the measured S_{21}^{total} data in absence of the sample to factor out the propagation phase.

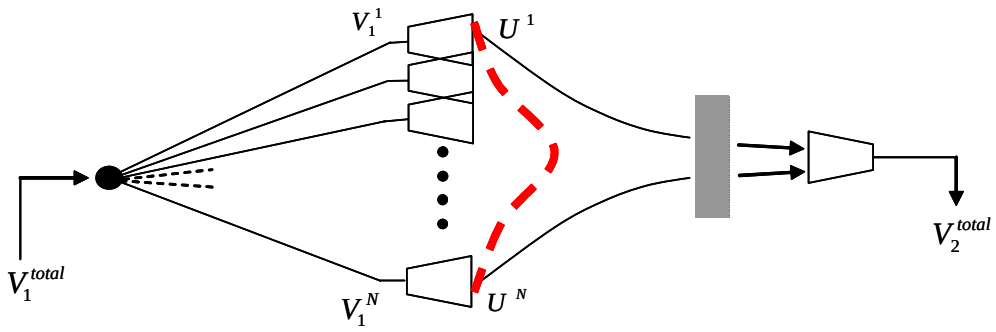

Figure 3.8: Simplified picture of the new free-space measurement system.

3.4 Measurement Demonstration

As a reference, we proceeded to first characterize a simple dielectric slab with a known permittivity using planar and spherical virtual apertures. Furthermore,

a complex anisotropic degenerate band edge (DBE) slab was characterized with a spherical virtual aperture.

3.4.1 Dielectric Slab Using a Planar Aperture

The measurement performance of the proposed system employing planar scanning set-up [see Fig. 3.7(a)] is demonstrated here with a dielectric slab of $\varepsilon_r = 9.0$, thickness $t = 0.67$ cm, and cross-sectional dimension of 10.16×10.16 cm^2. Data was collected in the X-band (8-12 GHz) using a frequency sweep of 401 points with an Agilent 8722ET vector network analyzer. A pair of X-band standard gain horns was used for the transmitting/receiving probes with the parameters given in Table 3.2.

Table 3.2: Parameters for planar scanning example

Aperture lateral position (z_a)	Aperture transverse dimension ($2W_{99\%} \times 2W_{99\%}$)	Sampling interval ($\Delta x = \Delta y$)	Number of grid points
$-10\lambda_{8G}$ (37.5 cm)	$10\lambda_{8G} \times 10\lambda_{8G}$ (37.5×37.5 cm)	$0.5\lambda_{12G}$ (1.25 cm)	$31 \times 31 = 961$

Prior to processing the collected data, the air-measurement phase data (in absence of the sample) for each grid point was compared with the calculated one to investigate the need of phase error corrections. The calculated phase was obtained based on the given parameters described in Fig.3.7(a) and Table 3.2. Fig. 3.9 is one of the examples showing phase differences between two, which are air-measured and calculated phase responses at 10 GHz along the horizontal line (i.e., $x = 0$, $0 < y < 37.5$ cm). These

constant phase errors were caused by the misalignment of the first scanning point. Instead of recollecting all the data, the phase correction was done by adding/subtracting the observed phase differences into both air- and sample-measurement phase data for every frequency point and grid point. This method can be used under the assumption that the phase errors during air- and sample-measurements are identical.

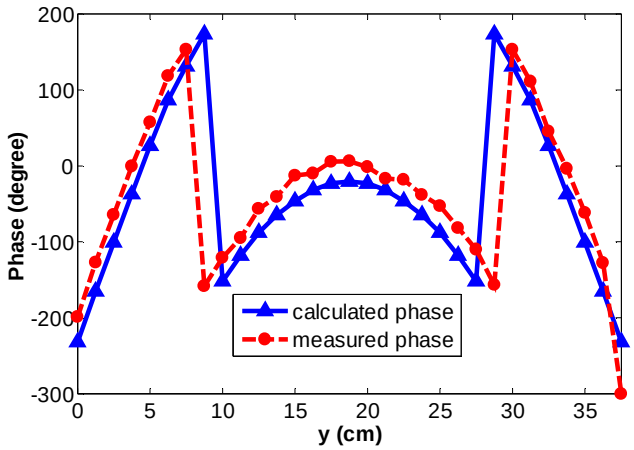

Figure 3.9: Calculated and measured S_{21} phase (without sample) at 10 GHz along the horizontal axis of the planar virtual aperture.

Indeed, Fig. 3.10 shows the measured S_{21} data before and after phase correction. Clearly, the phase correction significantly reduces the discrepancies between analytical and measured S_{21} data, particularly for the phase result depicted in Fig. 3.10(b). Also given in the figure is the measured S_{21} data using the single line of sight measurement named as horn-to-horn. The erratic behavior of the horn-to-horn data is due to diffractions from the sample's edges as the Gaussian beam was not adapted to illuminate the sample. Furthermore, as observed in Fig. 3.10(a), the magnitude of the S_{21} measured data can exceed 0 dB when diffractions from the sample's edges

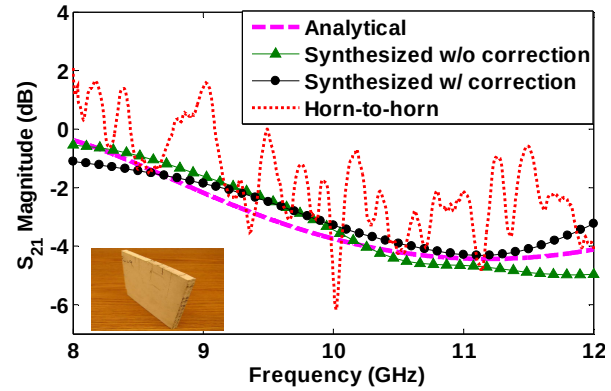

(a)

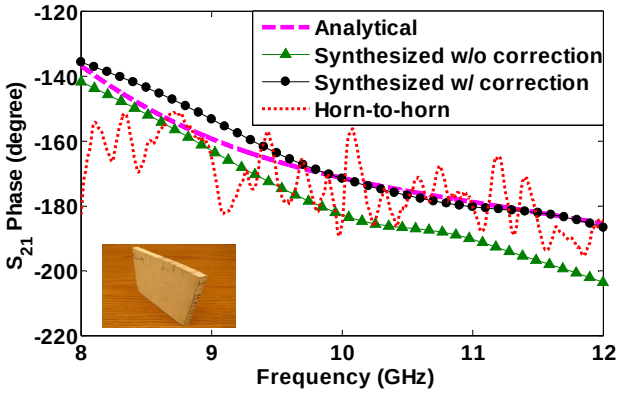

(b)

Figure 3.10: S_{21} data for the 0.67 cm thick dielectric slab ($\varepsilon_r = 9.0$) using the planar virtual aperture: (a) magnitude and (b) phase.

add coherently with the field transmitted through the sample. We close this section by noting that the permittivity extracted from the synthesized S_{21} data led to a maximum error of 4.3% from the reference value ($8.60 < \varepsilon_r < 9.21$) as shown in Fig. 3.15.

3.4.2 Dielectric Slab Using a Spherical Aperture

We proceeded to repeat measurements and characterization of a simple dielectric slab as in the previous subsection but using a spherical virtual aperture [see Fig. 3.7(b)] and thicker sample having $t = 1.31$ cm. The measurement was done in X-band using a standard gain horn as the receiving probe and a 2-18 GHz double ridge horn as the main reflector feed. The scanning parameters forming the spherical aperture are given in Table 3.3. Specifically, we should have $\theta_{99\%} > 25.55^\circ$ and $\Delta\theta = \Delta\phi < 7.39^\circ$ based on (3.3) and (3.5). As depicted in Fig. 3.11, the data were collected by rotating the receiving probe in the ϕ-direction and by sweeping across the θ-direction. During measurements, we recorded the S_{21} at each grid point by combining two orthogonally polarized responses as typically done for 3D antenna pattern measurements. For example, the x-polarized S_{21} was obtained by summing the V- and H-polarized S_{21} as depicted in Fig. 3.12.

Table 3.3: Parameters for spherical scanning example

θ-scan range ($-\theta_{99\%}$ to $\theta_{99\%}$)	ϕ-scan range	Sampling interval ($\Delta\theta = \Delta\phi$)	Number of grid points
-30° to 30°	0 to 360°	5°	$13 \times 36 = 468$

Fig. 3.13 shows the measured V- and H-polarized data and their addition in the absence of the sample (i.e., air-measurements). The V-pol data was collected by setting the feed horn with vertical polarization and rotating the rx-probe in θ- and ϕ-directions. The H-pol data was measured in the same way but with the horizontally polarized feed. The addition of these two sets of data using the configuration in

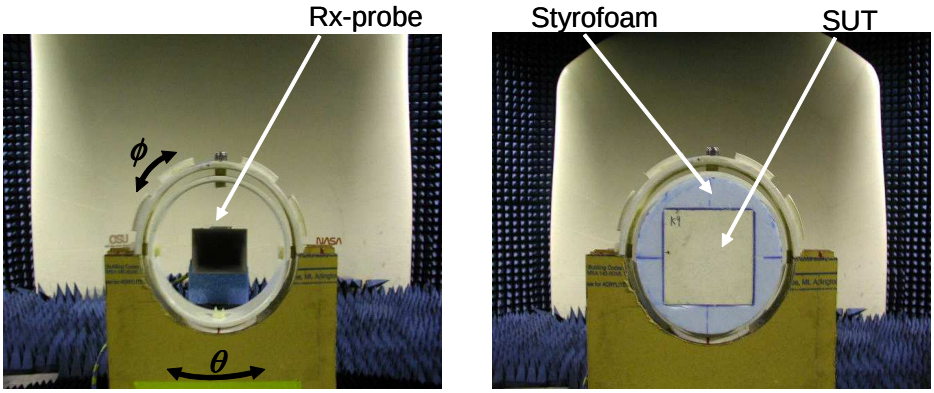

(a) (b)

Figure 3.11: Pictures of the sample holder in the OSU ElectroScience Lab anechoic chamber: (a) w/o sample and (b) w/ sample.

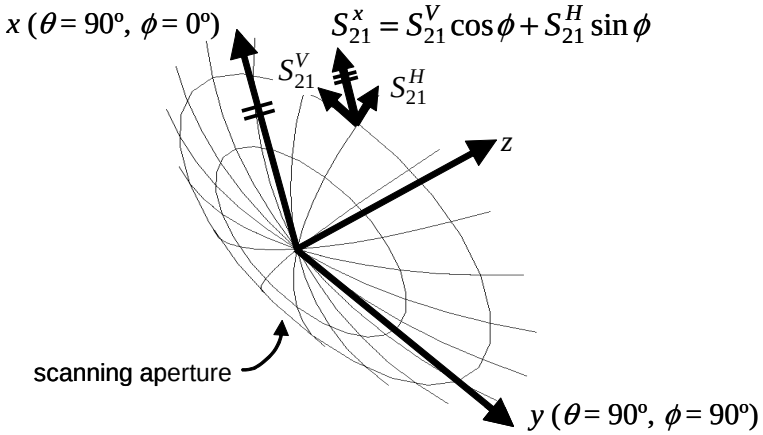

Figure 3.12: Illustration of data collection process associated with the spherical aperture.

Fig. 3.12 provides the results as if the measurements were taken by rotating the reflector in θ- and ϕ-directions.

The magnitude and phase of the measured S_{21} using the spherical virtual aperture are given in Fig. 3.14. These were obtained without the phase error correction step

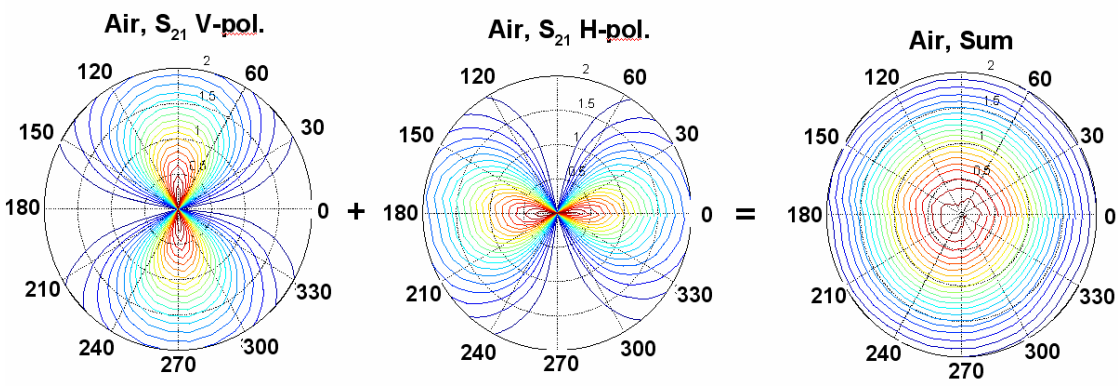

Figure 3.13: Polar contour plots of the S_{21} magnitude measured in the air.

as such errors in both θ- and ϕ-directions were negligible, implying that our system set-up was highly accurate during measurements. Again, the horn-to-horn data in Fig. 3.14 is substantially affected by edge diffractions and multiple reflections. In contrast, the synthesized data are in excellent agreement with predicted analytical curves. The corresponding extracted permittivity is $8.89 < \varepsilon_r < 9.09$, i.e., within 2.3% of the reference value (see Fig. 3.15). That is, the spherical synthetic aperture yielded more accurate data than the planar one. We also note that the accuracy of the planar scan data can be further improved by including the radiation pattern of the scanning probe in the synthesis process.

3.4.3 Measurement of a Layered Anisotropic Slab

Having validated the proposed measurement method, we now proceed to characterize the transmission properties of a metamaterial slab. The latter is an 8-layer degenerate band edge (DBE) crystal with geometrical details given in Fig. 3.16. Each unit cell is composed of two anisotropic layers realized by printed metallic strips and an isotropic layer (i.e., air). We remark that this slab exhibits special modes that are

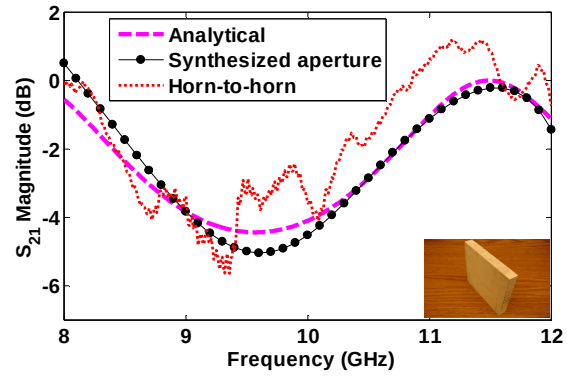

(a)

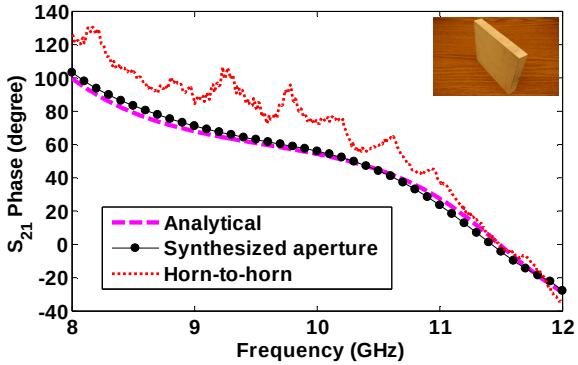

(b)

Figure 3.14: S_{21} data for the 1.31 cm thick dielectric slab ($\varepsilon_r = 9.0$) using the spherical virtual aperture: (a) magnitude and (b) phase.

highly resonant as pointed out in [9]. For the specific design in Fig. 3.16, the DBE slab is expected to exhibit three different resonances in the X-band as illustrated in the simulated band diagram (see Fig. 3.17).

The spherical virtual aperture was used for the measurement since it is more accurate and requires less grid points as demonstrated in the previous examples. Specifically, the same parameters as in Table 3.3 were used except for the frequency range of 7-14 GHz. As seen in Fig. 3.18, the measured S_{21} data using the synthesized aperture method accurately predicts the transmission behaviors by showing excellent

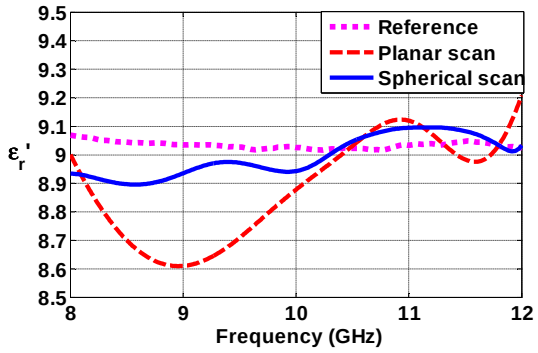

Figure 3.15: Measured dielectric constants of the dielectric slab using planar and spherical apertures. The reference data was measured by Agilent 85070 probe kit.

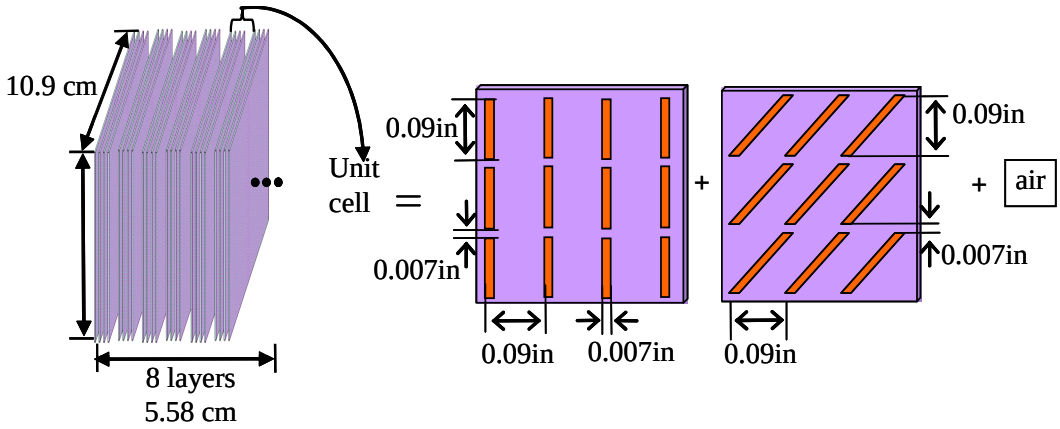

Figure 3.16: Geometry of the 8-layer DBE slab. Each unit cell is a compromised of two anisotropic layers and one isotropic layer each of thickness 0.02 inches. The third is just an air layer and the other two are Rogers RO4350B PCB with the printed metallic strips.

agreements with the simulated S_{21} carried out from a finite element boundary (FE-BI) code [59]. Indeed, Fabry-Perot transmission peaks are clearly identified at 8, 10.25, and 13.4 GHz as in Fig. 3.18(a), corresponding to the regular band edge (RBE),

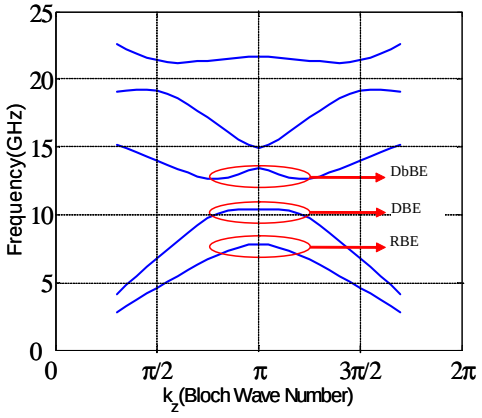

Figure 3.17: Band diagram of the assembled degenerate band edge slab. RBE, DBE, and DbBE refer to regular band edge, degenerate band edge, and double band edge, respectively.

degenerate band edge (DBE), and double band edge (DbBE) resonances indicated in [9].

Lastly, the measured S_{21} of air, the $\varepsilon_r = 9$ dielectric slab and DBE using the spherical virtual aperture set-up are visualized in Fig. 3.19. As can be seen, the measurements of the DBE shows strong field concentration at the middle when its polarization is tilted by $\phi = 55°$. This angle matches to the optimum illumination angle of the tested DBE slab [9].

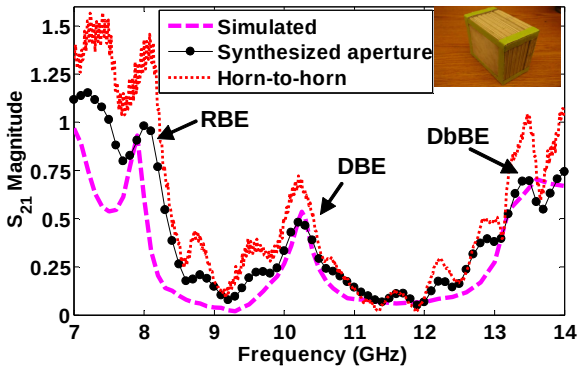

(a)

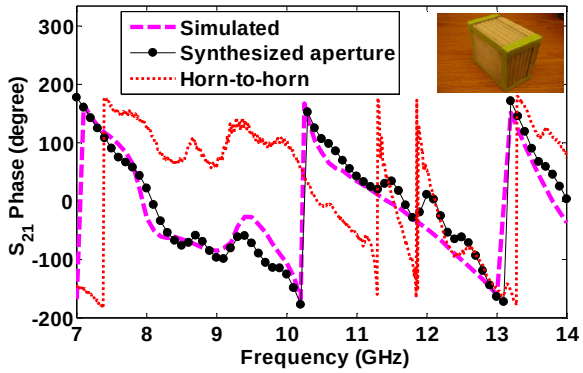

(b)

Figure 3.18: S_{21} data for DBE slab: (a) magnitude and (b) phase.

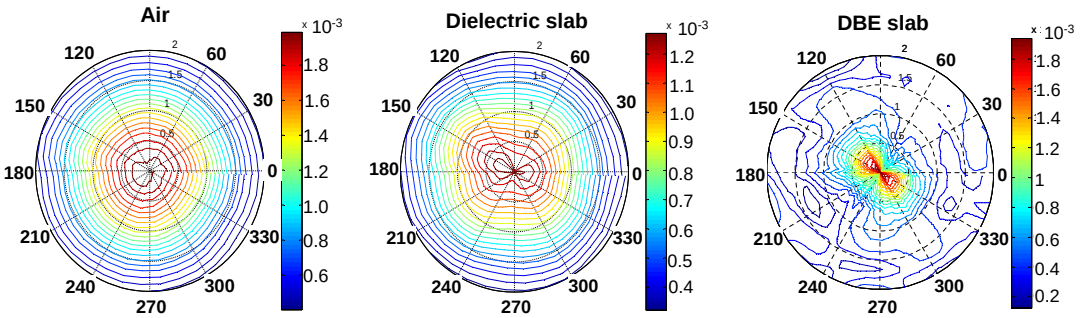

(a) (b) (c)

Figure 3.19: Polar contour plots of S_{21} magnitude with (a) air, (b) dielectric slab, and (c) degenerate band edge slab.

3.5 Error Analysis

Several factors contribute to the uncertainty of the FSM system: internal errors in network analyzer, incorrect information of sample thickness, imperfection in cable and connectors, remained diffraction effects, etc. As mentioned in Chapter 3.3, these systematic uncertainties can be significantly reduced by the S_{21} calibration and time-gating technique. In this section, we investigate other two possible error sources for the synthetic Gaussian beam method. We first describe the effect of the transmitting probe misalignment on the reconstructed Gaussian beam. Another error source considered is the sample misalignment. An analysis for the sample misalignment error presented in here is not limited to the synthetic Gaussian beam method but can be applied to any T/R method.

3.5.1 Transmitting Probe Misalignment

In the synthetic Gaussian beam method, misalignments of the scanning probes may contribute to the error in the final result. To investigate this effect, a Monte Carlo analysis was performed by assuming the presence of random misalignment errors. Suppose that each probe location on the spherical scanning aperture is misaligned by a random error of $\Delta\theta$ as depicted in Fig. 3.20. As the spherical aperture is located in the far-field, the wave generated by each probe can be approximated to a plane wave. Thus, the sum of the weighted plane waves is expressed by

$$E_{tot} = \sum_{n} \sum_{m} U\left(\theta_m, \phi_n\right) E\left(\theta_m, \phi_n\right), \tag{3.11}$$

where $E\left(\theta_m, \phi_n\right)$ is the plane wave coming from the given elevation (θ_m) and azimuth (ϕ_n) angles, and $U\left(\theta_m, \phi_n\right)$ is the weighting coefficient for the corresponding plane

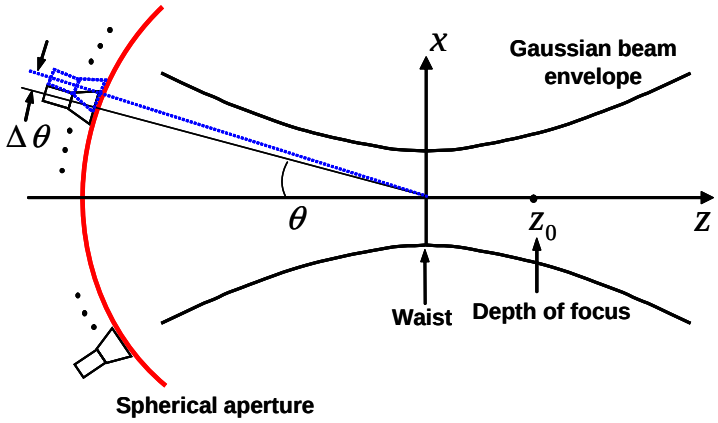

Figure 3.20: Problem set-up to investigate the probe misalignment effect.

wave. The latter is identical to the Gaussian beam complex amplitude given in (3.1). For algebraic convenience, in this problem, the variables in (3.1) are converted from the Cartesian coordinate into the spherical coordinate notation by substituting $x = r\cos\theta$, $y = r\sin\theta\cos\phi$, and $z = r\sin\theta\cos phi$. This implies the plane wave is always inciding from $-z$-space and the measure of θ and ϕ start from x- and y-axes, respectively, as shown in Fig. 3.21.

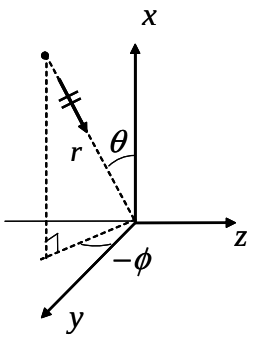

Figure 3.21: The coordinate convention to define the transformation between the Cartesian and spherical coordinate systems.

For the next step, the uniformly distributed positioning errors are generated and then applied into (3.11). It is worth mentioning that these positioning errors only affect the phase terms of each plane wave. In other words, the positioning errors does not affect the Gaussian weighting values, $U(\theta_m, \phi_n)$, but affect the phase of each plane wave term in $E(\theta_m, \phi_n)$. For the overall reconstructed Gaussian beam, however, both the magnitude and phase are affected by these errors. That is, the addition of the erroneous plane waves, although they only have phase errors, also impacts the magnitude of the added beam.

We can observe these error properties in the following figures. Fig. 3.22 illustrates the probability density functions (PDF) of the phase error at the waist of the reconstructed Gaussian beam when the uniformly distributed probe positioning errors of $\Delta\theta = [-1^\circ, 1^\circ]$ are applied at each probe location. Each subplot indicates the PDF of phase error for a single plane wave, or a sum of 2, 5, 15 plane waves, as indicated in the figures' title. As can be observed in Fig. 3.22(a), the standard deviation (STD, i.e., width of PDF) of the resulted phase error decreases as the number of added plane waves increases. This is because a PDF for the sum of independent random variables is given by the convolution integral of their PDFs [60]. For a single plane wave [see Fig. 3.22(a)], the phase error distribution is almost uniform since the positioning error is in the form of uniformly distributed random error. On the other hand, the phase error for the sum of two plane waves [see Fig. 3.22(b)], is resulted in a trapezoidal shape as two independent (but not identical) PDFs are convolved to each other. Successively convolving PDFs with a trapezoidal form is resulted into a narrower PDF as depicted in Fig. 3.22(c) and (d).

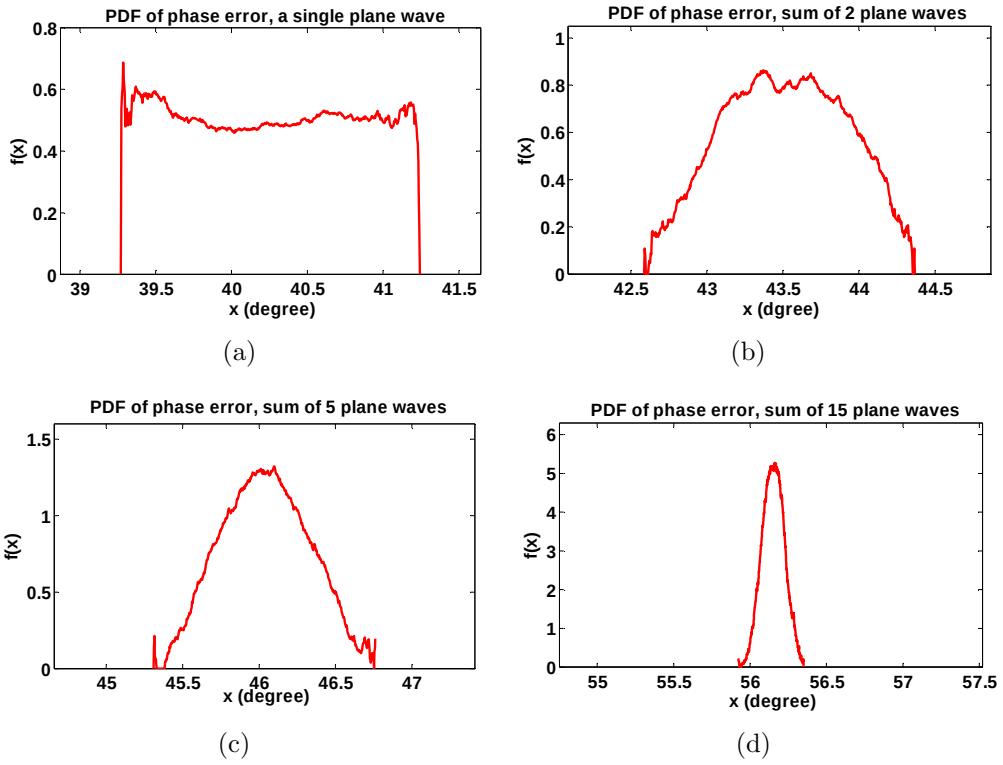

Figure 3.22: PDF for the phase error of the plane wave sum: (a) only one plane wave, (b) sum of 2 plane waves, (3) sum of 5 plane waves, and (d) sum of 15 plane waves.

Next, Fig. 3.23 illustrates the PDFs of the magnitude error. There is no magnitude error for a single plane wave as shown in Fig. 3.23(a). However, adding the plane waves with a phase error produces a magnitude error as depicted in Fig. 3.23(b)-(d). But the trend is different from the PDF of the phase error. The STD of the magnitude error increases by adding the plane waves at the first time but decreases after certain numbers of plane waves are added. For our simulation set-up, this turn-around occurs after adding 5 plane waves.

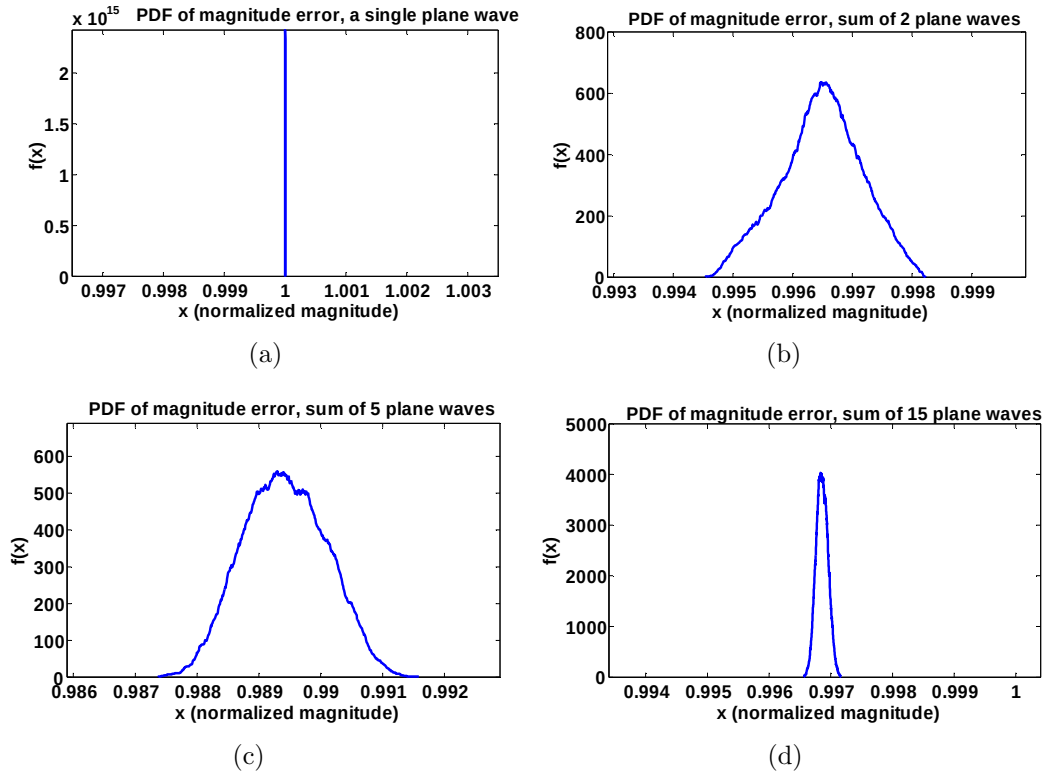

Figure 3.23: PDF for the magnitude error of the plane wave sum: (a) only one plane wave, (b) sum of 2 plane waves, (3) sum of 5 plane waves, and (d) sum of 15 plane waves.

Finally, the PDFs of the phase and magnitude errors after adding all the plane waves with random positioning errors are depicted in Fig. 3.24(a) and (b), respectively. Specifically, $19 \times 19 = 361$ plane waves are added according to the defined scanning range and interval ($\theta = 45°\colon 5°\colon 135°$, $\phi = 225°\colon 5°\colon 315°$). As can be seen, the histograms of both phase and magnitude errors can be approximated to the Gaussian PDFs followed by the central limit theorem.

According to Fig. 3.24, the E-field phase and magnitude errors at the waist due to $[-1°, 1°]$ probe misalignment errors were only 0.009% and 0.01%. Another simulation performed with the misalignment error of $[-5°, 5°]$ returns 0.25% and 0.02% error

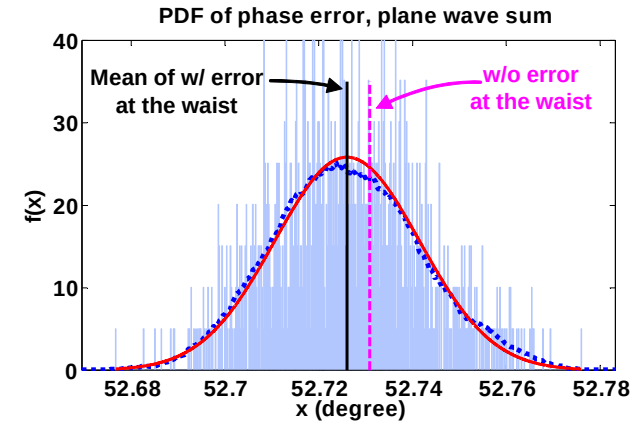

(a)

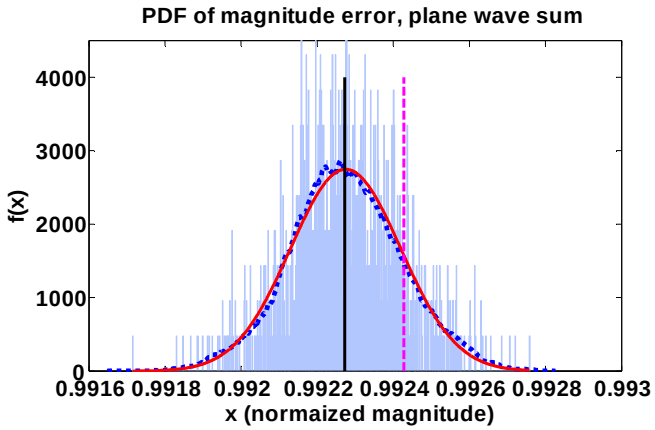

(b)

Figure 3.24: PDFs after adding all plane waves with positioning errors: (a) phase and (b) magnitude.

for each. That is, the overall errors increase as more severe misalignment error is assumed, but still the values are very small (compared to network analyzer transmission tracking errors or calibration errors which are usually larger than 1%).

To investigate this small error behavior, we compared field plots of the reconstructed Gaussian beam. Fig. 3.25(a)-(d) compare the front-views (at the waist) and side-views of the E-field magnitudes for the case without misalignment error and with

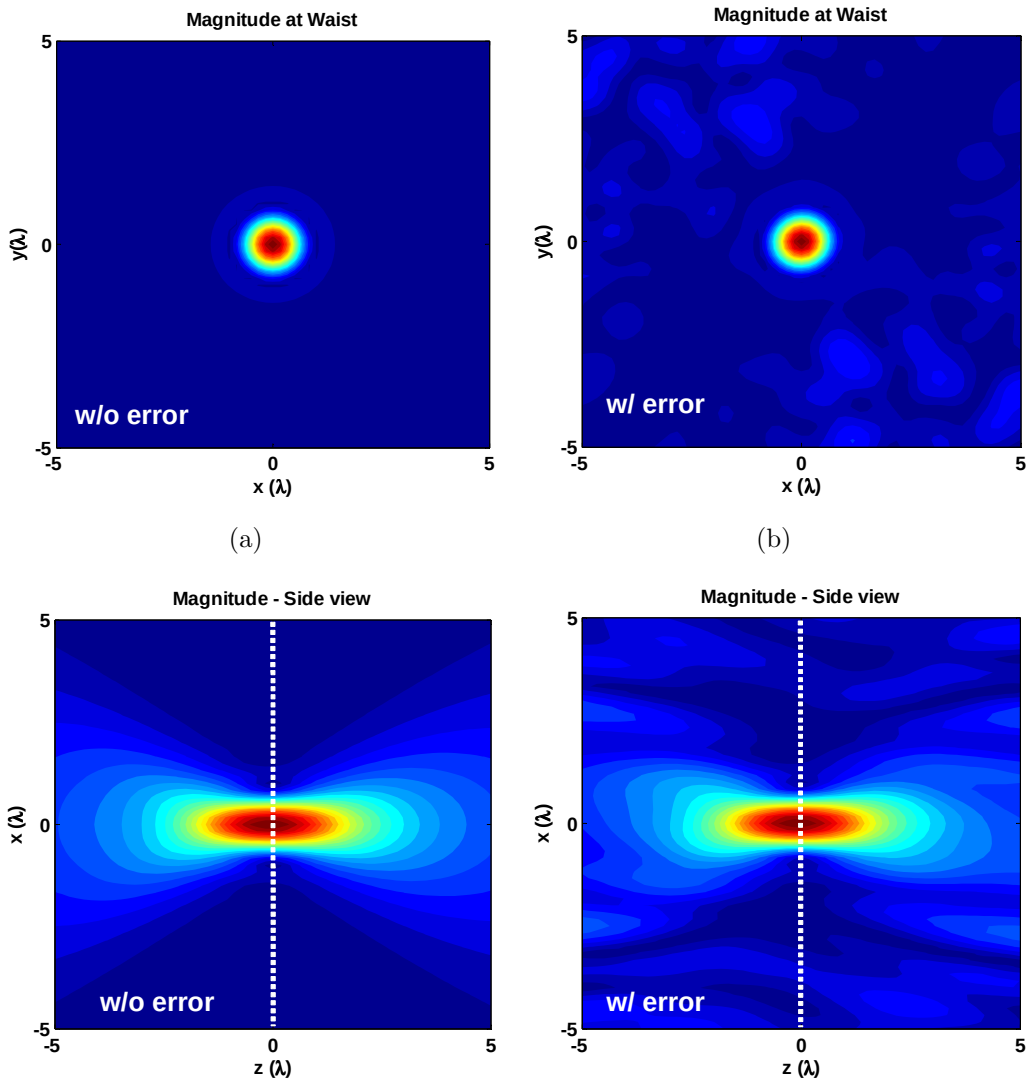

Figure 3.25: Front-views and side-views of the E-field magnitude: (a) front-view without misalignment error and (b) with misalignment error, (c) side-view without misalignment error and (b) with misalignment error.

error. Note that the with-error data is obtained by applying the uniformly distributed random error in the range of $[-5°, 5°]$. As observed, the field at the waist location is well-defined even though such large misalignment error was assigned. This can be

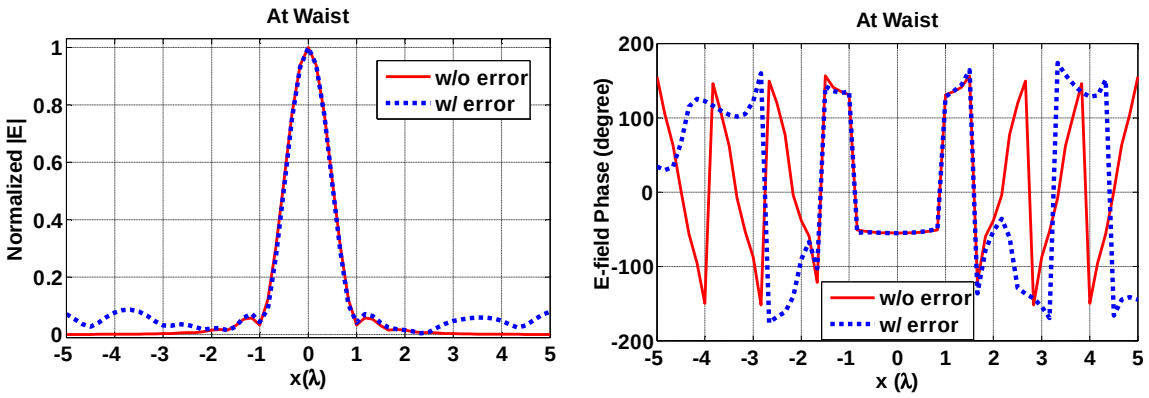

(a) (b)

Figure 3.26: E-field magnitude and phase at the waist [along the white line in Fig. 3.25(b)]: (a) normalized magnitude and (b) phase in degree.

more clearly observed in Fig. 3.26, which shows the normalized magnitude and phase of the reconstructed E-field at the waist [along the white line in Fig. 3.25(b)]. The reason for this error insensitive behavior at the waist is related to the way the probe misalignment error is defined. That is, the probe is still on the surface of the spherical aperture although it is misaligned (see Fig. 3.20). This implies the probe field is still propagating toward the waist. Therefore, the error due to the probe misalignment can be considered as the error of applying a wrong weighting value during the Gaussian reconstruction process. Since the weighting values are defined as a slowly varying function to satisfy the paraxial approximation, the difference of weighting values between adjacent locations (on the spherical aperture) is not significant. This error behavior may explain the smaller error values observed in the spherical aperture set-up as in Chapter 3.4.

3.5.2 Sample Misalignment

Another misalignment factor can be the sample misalignment as depicted in Fig. 3.27. When $\Delta\theta = 0$, there is no sample misalignment error and this is a common assumption in the property de-embedding process of the T/R method.

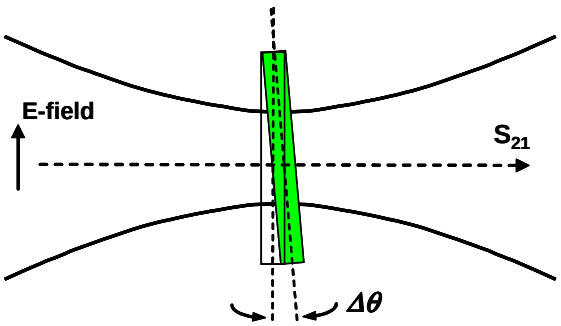

Figure 3.27: Illustration of sample misalignment error in the Gaussian beam measurement method.

To investigate the error caused by the sample misalignment, we first derive the analytical S_{21} when a dielectric slab of ε_r is tilted by $\Delta\theta$. By assuming the sample is illuminated with a well-reconstructed Gaussian beam, the problem can be approximated to a plane wave transmission problem. The problem set-up is depicted in Fig. 3.28. The S_{21} with and without the misalignment error can be defined as

$$S_{21}^{0} = \exp(-jk_0 d_1) S_{21}^{nor} \exp(-jk_0 d_2), \tag{3.12}$$

$$S_{21}^{err} = \exp(-jk_0 d_1) S_{21}^{obl} \exp(-jk_0 \overline{CF}) \exp(-jk_0 d_2), \tag{3.13}$$

where k_0 is the free-space wave number, S_{21}^{nor} and S_{21}^{obl} refer to the transmission coefficients (from the front to rear surface of the sample) with normally and obliquely

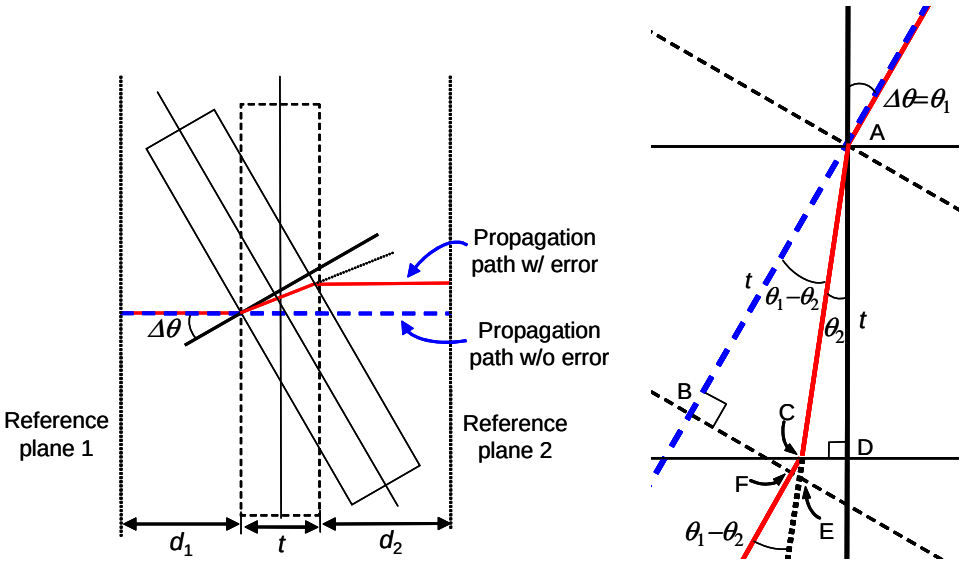

Figure 3.28: (a) Geometry of the problem. (b) Zoomed and rotated picture for the middle section of (a).

incident plan waves, respectively. Also, $\overline{CF}$ is defined by the small air region after the slab as illustrated in Fig. 3.28(b). $\overline{CF}$ can be obtained from simple trigonometric algebras as

$$\overline{CE} = \overline{AE} - \overline{AC} = \frac{t}{\cos(\theta_1 - \theta_2)} - \frac{t}{\cos(\theta_2)}, \tag{3.14}$$

$$\overline{CF} = \overline{CE}\cos(\theta_1 - \theta_2) = t\left[1 - \frac{\cos(\theta_1 - \theta_2)}{\cos(\theta_2)}\right]. \tag{3.15}$$

Next, let us consider the calculation of S_{21}^{obl}. This is a classical EM problem that can be solved by the well-known Fresnel formulae [61]. The problem set-up for S_{21}^{obl} calculation is illustrated in Fig. 3.29. The fields in each layer must satisfy the wave equation:

$$\left(\nabla^2 - k_i^2\right) u_i = 0, \tag{3.16}$$

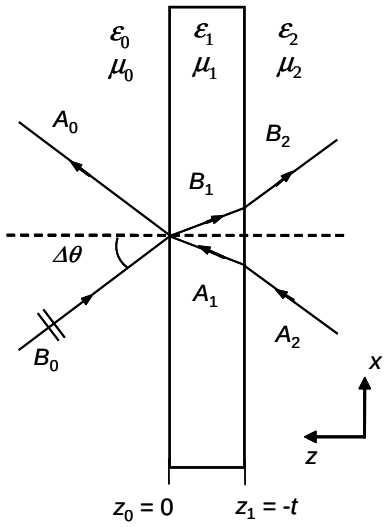

Figure 3.29: The problem set-up for calculating S_{21}^{obl}.

where u_i denotes either y-polarized E-field (TE case) or H-field (TM case) at the ith layer, and k_i is the wave propagation constant at each layer. That is,

$$k_i^2 = \omega^2 \mu_i \varepsilon_i. \tag{3.17}$$

The general solution of (3.16) is given by

$$u_i = [A_i \exp(-j\xi_i z) + B_i \exp(+j\xi_i z)] \exp(-j\eta_i x), \tag{3.18}$$

where A_i and B_i are coefficients of the $+z$-propagating and $-z$-propagating waves in each layer, and ξ_i and η_i are propagation constants in z- and x-directions, respectively. As (3.18) is obtained using the separation of variables, ξ_i and η_i must satisfy the following relationship:

$$k_i^2 = \xi_i^2 + \eta_i^2. \tag{3.19}$$

Note that $\eta_0 = k_0 \sin(\Delta\theta) = \eta_1 = \eta_2$ due to the plane wave matching condition along the z-direction. Since η_i and k_i are known values, ξ_i can be solved from (3.19). In

order to find A_i and B_i in each layer, it is convenient to formulate the relationship between adjacent layers into a matrix form as below [61]:

$$\begin{pmatrix} A_i \\ B_i \end{pmatrix} = (L_i^{e,m}) \begin{pmatrix} A_{i+1} \\ B_{i+1} \end{pmatrix}, \tag{3.20}$$

where the superscript e and m refer to TE and TM cases, respectively. $(L_i^{e,m})$ is a 2 by 2 matrix whose elements can be found via the boundary conditions at each interface. The derivation of $(L_i^{e,m})$ is straightforward but lengthy. Only the result is given as below:

$$(L_i^e) = \begin{pmatrix} \frac{1}{2}\left[1 + \frac{\mu_i}{\mu_{i+1}}\frac{\xi_{i+1}}{\xi_i}\right] \exp\left[-j(\xi_{i+1} - \xi_i)z_i\right] & \frac{1}{2}\left[1 - \frac{\mu_i}{\mu_{i+1}}\frac{\xi_{i+1}}{\xi_i}\right] \exp\left[+j(\xi_{i+1} + \xi_i)z_i\right] \\ \frac{1}{2}\left[1 - \frac{\mu_i}{\mu_{i+1}}\frac{\xi_{i+1}}{\xi_i}\right] \exp\left[-j(\xi_{i+1} + \xi_i)z_i\right] & \frac{1}{2}\left[1 + \frac{\mu_i}{\mu_{i+1}}\frac{\xi_{i+1}}{\xi_i}\right] \exp\left[+j(\xi_{i+1} - \xi_i)z_i\right] \end{pmatrix}, \tag{3.21}$$

$$(L_i^m) = \begin{pmatrix} \frac{1}{2}\left[1 + \frac{\varepsilon_i}{\varepsilon_{i+1}}\frac{\xi_{i+1}}{\xi_i}\right] \exp\left[-j(\xi_{i+1} - \xi_i)z_i\right] & \frac{1}{2}\left[1 - \frac{\varepsilon_i}{\varepsilon_{i+1}}\frac{\xi_{i+1}}{\xi_i}\right] \exp\left[+j(\xi_{i+1} + \xi_i)z_i\right] \\ \frac{1}{2}\left[1 - \frac{\varepsilon_i}{\varepsilon_{i+1}}\frac{\xi_{i+1}}{\xi_i}\right] \exp\left[-j(\xi_{i+1} + \xi_i)z_i\right] & \frac{1}{2}\left[1 + \frac{\varepsilon_i}{\mu_{i+1}}\frac{\xi_{i+1}}{\xi_i}\right] \exp\left[+j(\xi_{i+1} - \xi_i)z_i\right] \end{pmatrix}. \tag{3.22}$$

With the combination of (3.20) and (3.21) or (3.22), any A_i and B_i can be obtained if the incident wave property (B_0) is given. In this problem, we are interested in the resulting transmission coefficient from a TM-polarized plane wave incidence. This can be solved by

$$S_{21}^{obl} = \frac{B_2}{B_0} = \frac{1}{l_{22}}, \tag{3.23}$$

where l_{22} is the $(2,2)$ element in $[L^m]$. With S_{21}^{obl} obtained from (3.23), S_{21}^{err} can be calculated by (3.13).

Using the analytical S_{21}^{err}, ε_r of the sample with misalignment error can be de-embedded. We compared this to the known ε_r of the dielectric slab. The misalignment error used in this study varied from 0 to 5° and a dielectric slab of $\varepsilon_r = 9$, $\tan\delta = 0.1$, and $t = 6.52$ mm was used. Fig. 3.30(a) and (b) depict the de-embedded ε_r and $\tan\delta$

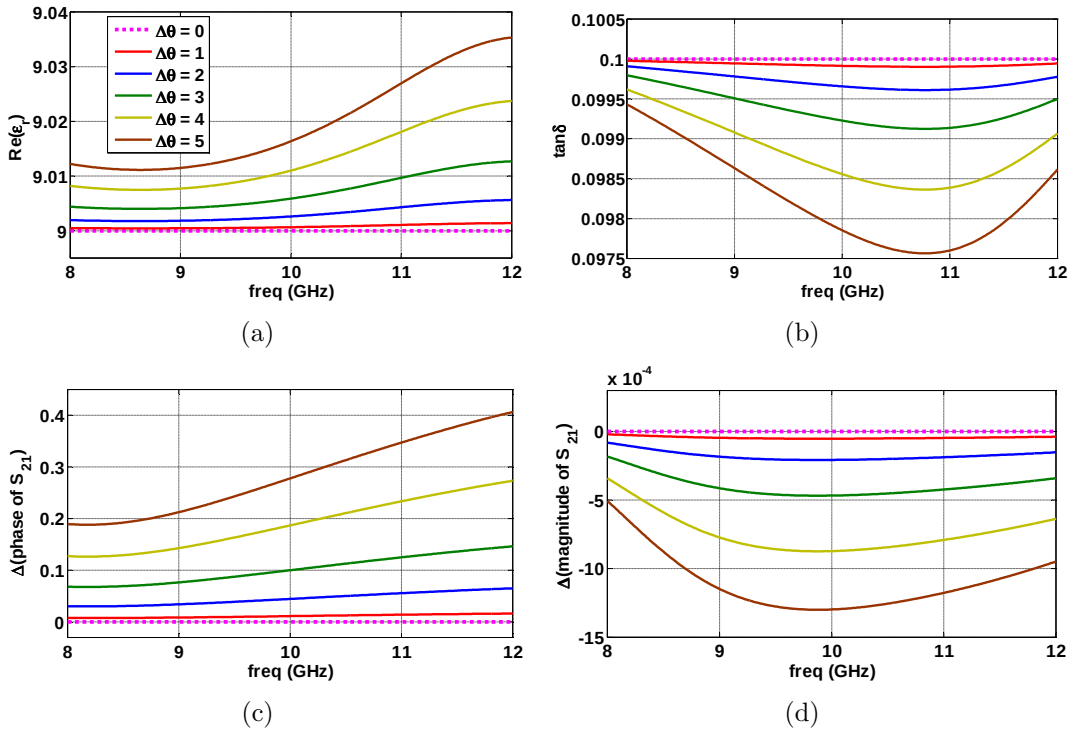

Figure 3.30: (a) The de-embedded ε_r and tanδ by varying the misalignment angle. (b) The errors in the S_{21} phase and magnitude data.

at X-band with different misalignment angles. As can be seen the error increases for larger $\Delta\theta$. For instance, the error in ε_r at 12 GHz (frequency exhibiting the largest variation) increases from 0.01% to 0.35% as $\Delta\theta$ varies from 1 to 5°, and the tanδ error at 10.77 GHz varies from 0.1% to 2.4%. The errors in the S_{21} phase and magnitude responsible to these de-mebedded ε_r and tanδ are also shown in Fig. 3.30(c) and (d). The comparison between (a)-(b) and (c)-(d) informs that the errors in ε_r and tanδ are strongly related to the errors in the S_{21} phase and magnitude, respectively. However, they do not exactly follow one from the other.

3.6 Summary

We described a new non-invasive material characterization technique. The proposed measurement system is based on a virtual transmitting aperture synthesized to produce a Gaussian beam spot-focused on the sample under test. The proposed approach minimizes diffractions from the sample edges making the transmission measurements closer to ideal. Furthermore, unlike the fixed FSM, there is no need to precisely design a lens since a focused beam is synthetically reproduced by the Gaussian weighting process. We also remark that the new system set-up can be easily retrofitted to existing planar and spherical scanning apparatuses available in most EM measurement facilities, and is suitable for cluttered lab environments since the synthesized beam eliminates the scattering from nearby structures. However, the overall measurement time for the proposed system is longer than that of conventional spot-focused horn-pairs (due to mechanical scanning speeds). For instance, the spherical scan used to characterize the metamaterial slab took a little less than 2 hours. Nevertheless, this time is comparable to typical near and far field scanning systems for antenna characterization.

Chapter 4

TAPERED STRIPLINE METHOD FOR MAGNETO-DIELECTRIC SLABS

In the previous chapter, the synthetic Gaussian beam method was introduced and its effectiveness in the characterization of bulk RF materials and engineered composites was demonstrated at X-band. However, this method is not practical at relatively low frequencies ($<$ 5 GHz). As the frequency decreases, the size of the probe (e.g., horn antenna) increases, although the problematic lens is removed from the system. More importantly, the required sample size must increase to avoid the diffraction from the sample edges as the waist size of the reconstructed Gaussian beam is larger for the lower frequencies. For example, a sample larger than λ is required to measure S_{21} without concerning the edge diffraction. Another limitation of the synthetic Gaussian beam method is that only ε *or* μ of the sample can be characterized. To simultaneously characterize ε *and* μ, it is necessary to collect not only S_{21} but also S_{11} data. It may be possible to measure S_{11} using a bi-static measurement set-up [62], but then the system requires two different rotators for tx- and rx-sides. This also implies the enormous increase in the measurement time, system size, and cost.

The above-mentioned practical difficulties led to develop a new Type-I T/R characterization method. More specifically, a tapered stripline is designed to measure the S_{11} and S_{21} at the same time in the frequency range of 50 MHz to 4.5 GHz.

4.1 Introduction

Recent engineered composites most likely have both non-trivial ε and μ values ($\varepsilon_r \neq 1$ and $\mu_r \neq 1$). For example, a composition of ferrite and resin [63] provides adjustable ε and μ based on the mixing ratio. Also, the usefulness of artificial magnetic materials [11,64] is highlighted by their capability of providing a high impedance surface that leads to effective size miniaturization of antennas. Such magneto-dielectric materials require simultaneous characterization of ε and μ to examine the interaction with the electromagnetic wave. Furthermore, it is necessary to characterize composites over a broad bandwidth to identify its applicable frequency range.

Using a type-I T/R set-up and the NRW process (see Chapter 2.4), the broadband and simultaneous characterization of ε and μ is possible by measuring both S_{11} and S_{21}. The most widely used tx-line for this purpose is the coaxial waveguide due to its wideband propagation of TEM wave [16–18]. However, the coaxial waveguide requires a sample to be in the form of toroid. This can be troublesome for hard materials (ferrites, ceramics, etc.), as special tools (diamond or water jet cutter) must be used to trim the sample. Furthermore, it is not practical to measure a series of different samples since the closed structure of the coaxial waveguide limits the accessibility to the inserted sample. For example, once the coaxial waveguide is opened to insert another sample, the whole measurement set-up must be re-calibrated.

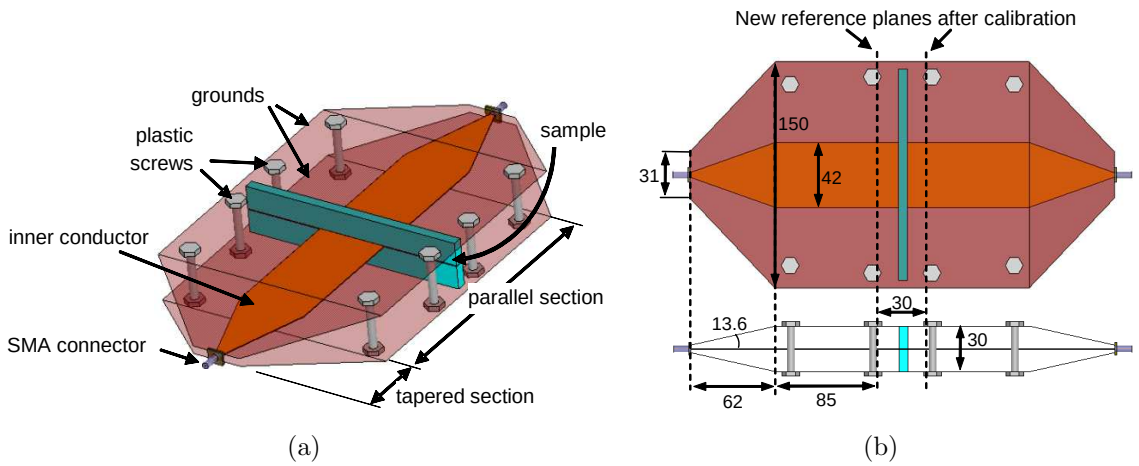

Figure 4.1: Illustration of the tapered stripline: (a) 3D view and (b) top and side views. Unit for dimension is millimeter.

In order to overcome the drawbacks of the coaxial waveguide, the use of other TEM supporting waveguides, such as parallel plates, striplines, and microstrip lines, can be considered [26, 42, 43, 46]. Among them, the stripline offers pure TEM propagation, better field focusing and less radiation loss. Besides TEM wave propagation, the proposed stripline structure has an opened geometry as shown in Fig. 4.1. Therefore, rectangular samples can be inserted through the sidewalls whose height is adjustable depending on the sample size. Two tapered sections attached between the input and output port connectors and the central section increase the fixture's cross-sectional area. It is worth noting that similar tapered stripline structures or the so-called TEM cells have been used for the electromagnetic susceptibility test of electronic devices [65, 66]. Herein, we optimize the geometry to characterize ε and μ of a magneto-dielectric slab over the 50 MHz to 4.5 GHz bandwidth.

4.2 Tapered Stripline Design

The tapered stripline geometry depicted in Fig. 4.1 was designed under the following considerations:

1. The width of the inner conductor is chosen to avoid the resonance of higher order modes [67].

2. To avoid perturbation at the sidewalls, the distance from the inner conductor to the sidewalls must be larger than 1.5×height [68].

3. The flare angle of the tapered section is small ($< 15°$) for smooth impedance transition [69].

4. A sufficient separation between the tapered section and sample is required so that the sample is not affected by evanescent modes excited at the junctions.

It is important to note that the upper operation frequency of the tapered stripline is limited by the cutoff frequency of the higher order modes. In principal, the stripline has no restriction in the frequency of operation if the TEM mode is the only propagating mode. However, in reality, the higher order modes are either excited by the geometry of the stripline itself (TE or TM modes) or by small discontinuities (evanescent modes), and their propagation becomes dominant as the frequency increases. The TE or TM modes are especially troublesome as they cause strong field resonances due to the presence of longitudinal field components. On the other hand, evanescent modes hardly affect the dominant TEM mode if rule 4) above is satisfied.

Assuming the overall length of the tapered stripline is fixed (to 32.4 cm), as in Fig. 4.1(b), the resonant frequency of the higher order mode (f_r) is determined by

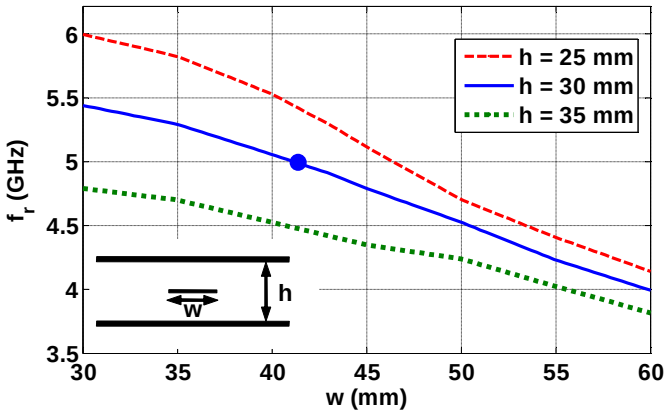

Figure 4.2: Resonant frequencies of TE_{10} mode with different inner conductor width (w) and stripline height (h) values.

the height (h) of the stripline and width (w) of the inner conductor as shown in Fig. 4.2 (obtained by observing resonance behaviors in the simulated S-parameters using Ansoft HFSS). As observed, the resonant frequency shifts higher for a smaller w and h values. Based on this study, we chose the inner conductor width of $w = 42$ mm to guarantee the measurement up to 5 GHz for the given height of $h = 30$ mm (shown as the solid dot datapoint in Fig. 4.2).

The full-wave simulation tool was also used to verify the field distribution inside the final stripline design. Fig. 4.3 shows the front-view for the vector magnitude plots of E- and H-fields. As depicted, typical cross-sectional field distributions of the TEM mode are observed at the middle of the parallel section. Such unidirectional E- and H-field distributions are also useful to characterize material properties with uniaxial or biaxial anisotropy [43].

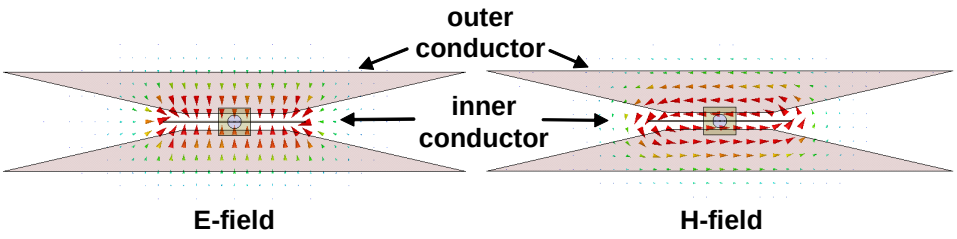

Figure 4.3: Vector magnitude plots of E- and H-fields at the middle of the tapered stripline.

4.3 Measurement Set-up and Calibration

Although the tapered striplne is carefully designed, reflections at ports are inevitable and must be removed using a proper calibration technique. Also, the reference planes must be shifted from the measurement ports to the vicinity of the sample to obtain accurate phase data in the S-parameters. The thru-reflect-line (TRL) calibration is known as the most effective calibration technique for non-coaxial line structures [70, 71]. In the TRL calibration process, the embedded error terms in the measured S-parameters are calculated and compensated via the measurements of three tx-line standards (i.e., thru-, reflect-, and line-standards). This implies there is no need of a matched-load standard whose fabrication is impractical for the stripline. To practice the TRL calibration, we implemented a computer code based on the equations described in Appendix B. Contrast to the TRL calibration software built-in commercial network analyzers, using the customized code ensures immediate check of the calibrated results.

Fig. 4.4 shows the pictures of fabricated TRL-standards. The reflect-standard was built by shorting the inner and outer conductors with a copper plate. The

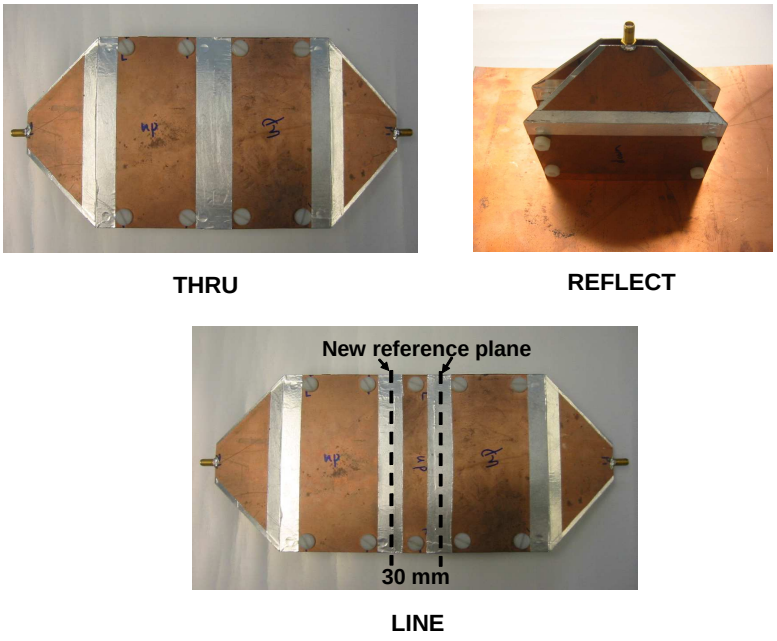

Figure 4.4: TRL calibration standards for the tapered stripline.

line-standard was realized by simply adding a delay-line at the middle of the thru-standard. After the TRL calibration, the reference planes are shifted from the SMA connectors to the new reference planes as in Fig. 4.4(c). Noting that the sample's S_{11} and S_{21} are measured by inserting the sample into the middle of the line-standard.

With the calibrated S-parameters, ε and μ of the sample can be de-embedded using the NRW process described in Chapter 2.4. Fig. 4.5 illustrates the whole measurement procedure in a flow chart.

4.4 Measurement Demonstration

Using the tapered stripline fixture and de-embedding process, we characterized ε and μ of dielectric and ferrite slabs.

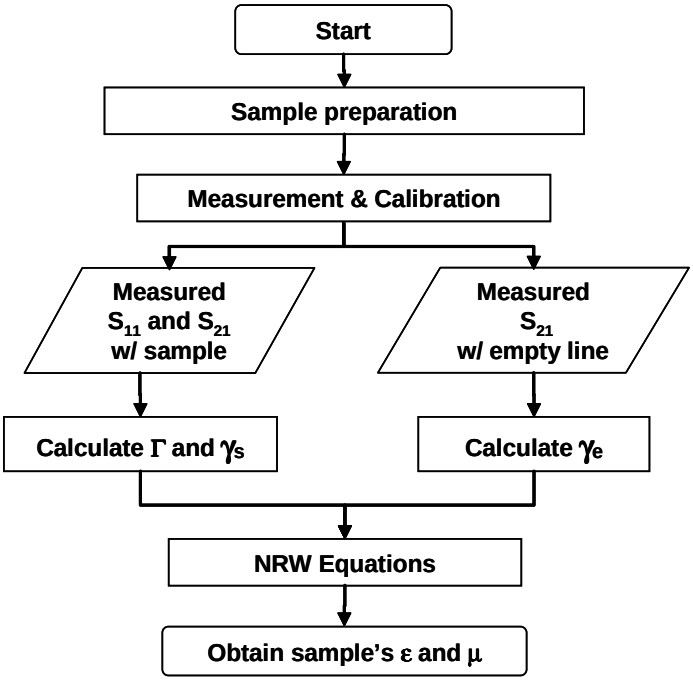

Figure 4.5: Flow chart of the sample property extraction process.

4.4.1 Characterization of a Dielectric Slab

The characterization of a known dielectric slab of $\varepsilon_r = 9$ with a low-loss factor of $\tan\delta_\varepsilon < 0.005$ is first presented. The thickness and height of the slab were $t = 6.52$ mm and $h = 3$ cm, respectively. The slab was inserted in the middle of the tapered stripline as shown in Fig. 4.6. Agilent N5230C network analyzer was connected to the SMA ports of the tapered stripline and the S-parameters were collected with the frequency sweep of 801 points over 50 MHz - 6 GHz.

The measured and calibrated S_{11} of the designated slab are presented in Fig. 4.7. As can be observed in both the (a) magnitude and (b) phase responses, the measurement is not valid after 4.86 GHz (marked by the arrows). The erratic peaks at the high frequency are due to the appearance of the TE_{10} mode resonance. These

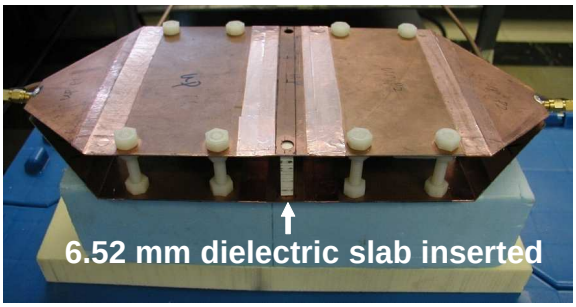

Figure 4.6: The measurement set-up for the $\varepsilon_r = 9$ dielectric slab characterization.

peaks appeared not only in the measured S-parameters of the sample but also in the S-parameters of the empty calibration standards. Otherwise, for the frequencies below the resonance, the TRL-calibration effectively removed the multiple reflections occurred at the ports [see Fig. 4.7(a)] and shifted the reference planes close to the sample [see Fig. 4.7(b)]. Consequently, the measured data after the TRL-calibration have good agreements with the analytical S_{11} calculated from (2.36). These improvements are more clearly observed in the time domain plots as in Fig. 4.8. The time domain responses of the measured S_{11}, Fig. 4.8(a), and S_{21}, Fig. 4.8(a), were obtained by converting the frequency responses with the inverse Fourier transform. As can be seen, the unwanted peaks caused by the port reflections are removed, and the peak representing the sample response is shifted toward the calibration planes (i.e., 0 ns) after calibration.

Next, Fig. 4.9 shows ε_r, μ_r, $\tan\delta_\varepsilon$, $\tan\delta_\mu$ of the dielectric slab de-embedded from the NRW process. The real parts of ε_r and μ_r are slightly smaller ($\varepsilon_r \approx 8.87$) and larger ($\mu_r \approx 1.03$) from the known values. We remark the error of the proposed measurement system is less than 3% for the real parts of ε_r and μ_r up to 4.5 GHz.

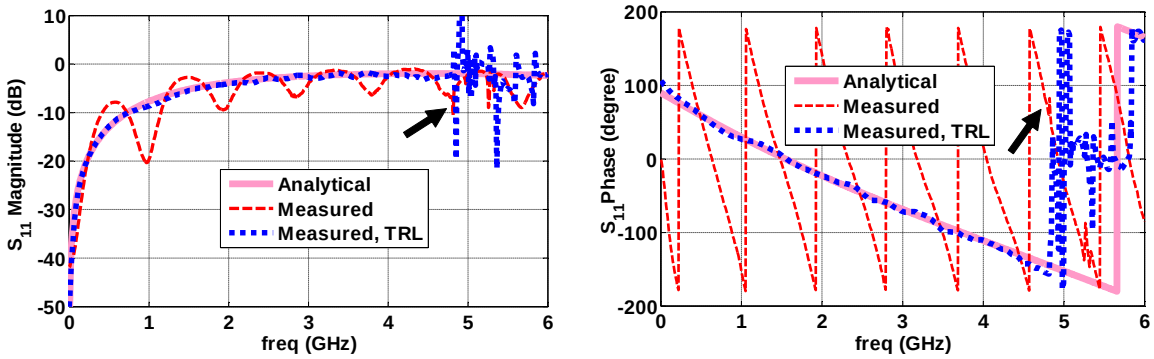

(a) (b)

Figure 4.7: Frequency domain responses for the measured S_{11} of the dielectric slab: (a) magnitude of S_{11} and (b) phase of S_{11}. The arrows indicate the first higher order mode resonance.

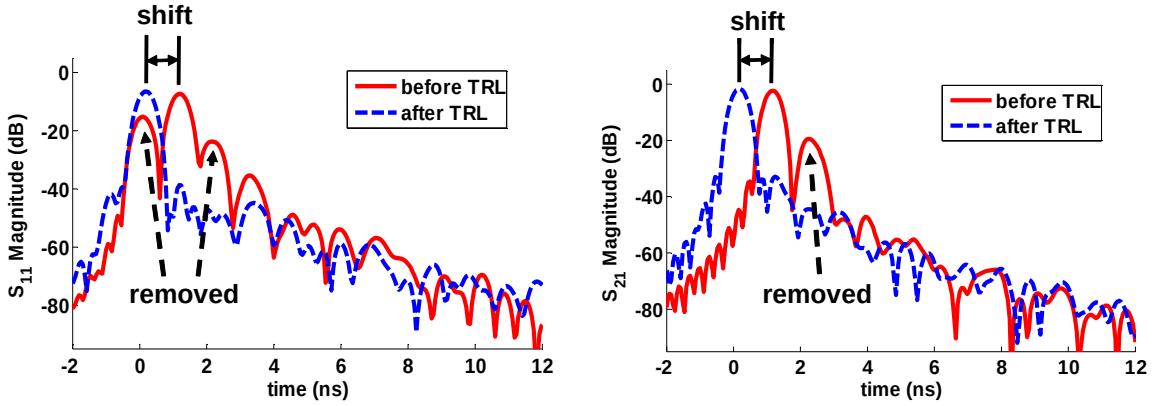

(a) (b)

Figure 4.8: Time domain responses for the measured S-parameters of the dielectric slab: (a) magnitude of S_{11} and (b) magnitude of S_{21}.

The erratic data shown in the shaded region of the figures clearly indicates the usable frequency range of the tapered stripline method is limited by the higher order mode resonance. It is worth noting that the low-loss characteristic of the given slab could be identified from the measured loss tangent data, however, quantatatively accurate

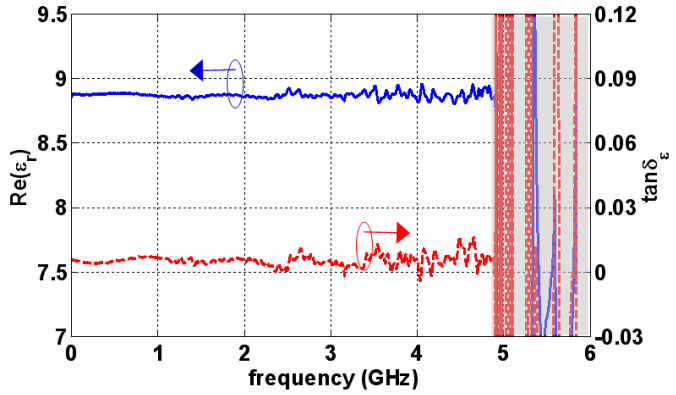

(a)

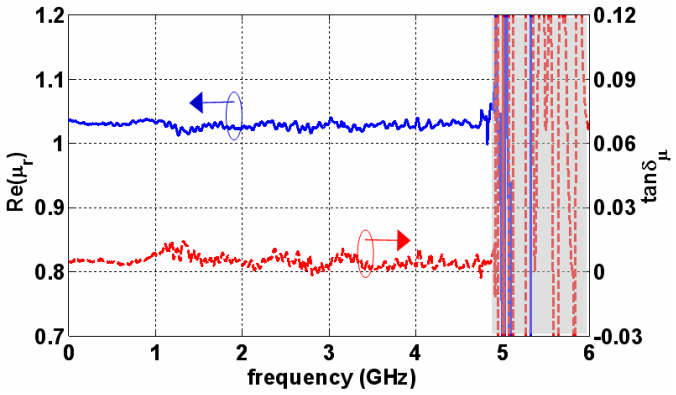

(b)

Figure 4.9: De-embedded properties of the dielectric slab: (a) ε_r and $\tan\delta_\varepsilon$, and (b) μ_r and $\tan\delta_\mu$.

results were not available. This corresponds to the limitation of T/R method discussed in Chapter 2.4. As mentioned, a typical resolution for the loss measurement is around $\tan\delta \approx 0.01$ for the T/R method. Since the measured dielectric slab had a very low-loss characteristic (i.e., $\tan\delta < 0.005$), the exact loss values could not be carried out using the tapered stripline method.

4.4.2 Characterization of a Ferrite Slab

Using the same set-up as described in the dielectric slab measurement, we proceeded to characterize an NiZn ferrite slab. The ferrite slab was simply inserted after removing the dielectric slab through the sidewall of the tapered stripline [see Fig. 4.10(a)], as the height of the ferrite slab was identical to the dielectric slab (3 cm). As long as the prepared samples have the same height, successive measurements can be made without detaching or re-calibrating the structure.

The measured data from the tapered stripline were compared to the the data obtained from the conventional inductance measurement method (Agilent E4991A impedance analyzer with 16453A fixture). Its set-up is illustrated in Fig. 4.10(b). In case of the inductance measurement method, the ferrite slab was tailored into a toroidal form. For this, we had to use a water jet cutter to precisely trim the rounded part of the ferrite slab.

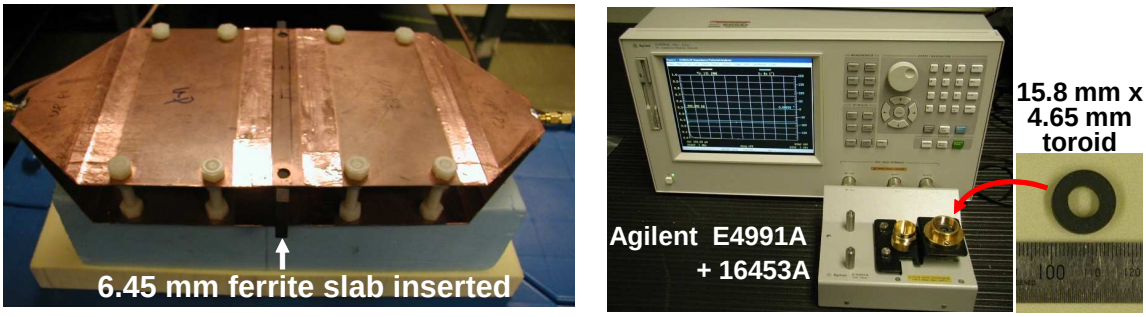

(a) (b)

Figure 4.10: The measurement set-up for the NiZn ferrite slab: (a) with the tapered stripline and (b) with the impedance analyzer

Fig. 4.11 shows the de-embedded Re(μ_r) and tanδ_μ of the NiZn ferrite. The dotted curves refer to the results from the inductance measurement. As observed, they have excellent agreement up to 1 GHz. For the frequencies above 1 GHz, the inductance measurement is not correct since the capacitance inside the measurement fixture cannot be ignored [28]. This capacitance forms a parallel LC resonator together with the inductance inside the magnetic sample. As a result, the measured data is distorted by the resonance at the higher frequencies. On the other hand, the stripline measurement is feasible until the appearance of the first higher order mode resonance at 4.86 GHz.

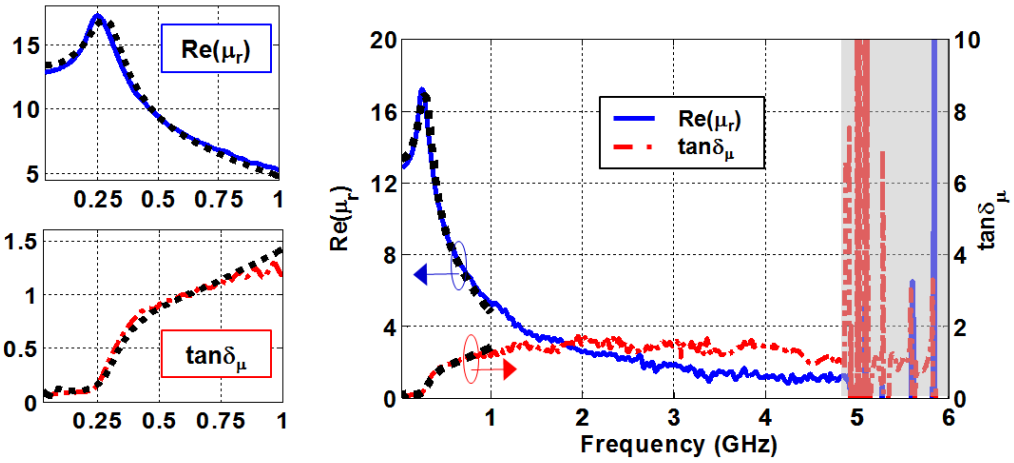

Figure 4.11: De-embedded Re(μ_r) and tanδ_μ of the NiZn ferrite slab. The dotted curves indicate the measured data from the inductance method (Agilent E4991A with 16453A). The insets to the left are the zoomed in pictures of the measurements below 1 GHz.

The dielectric properties, Re(ε_r) and tanδ_ε, are also compared. Fig. 4.12 shows their measurement set-ups. The measurement fixture attached to the impedance analyzer had to be switched from 16453A to 16454A for the characterization of dielectric

properties (see Chapter 2.2). Moreover, additional sample preparation steps were required as the sample must be prepared in the form of a thin plate. Such exhausting preparation was not required for the tapered stripline method as the dielectric and magnetic properties were simultaneously obtained via a single measurement.

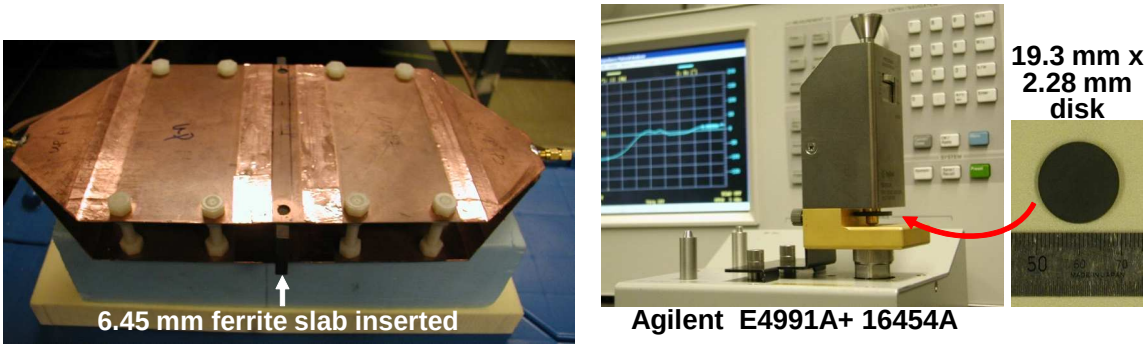

(a) (b)

Figure 4.12: The measurement set-up for the dielectric properties of the NiZn ferrite slab: (a) with the tapered stripline and (b) with the impedance analyzer

Fig. 4.13 shows the measured Re(ε_r) and tanδ_ε. As can be seen, the results from the impedance analyzer exhibit notable variations versus the frequencies, although the Re(ε_r) and tanδ_ε of the given ferrite slab were expected to have the frequency independent premittivity, which are correctly captured in the tapered stripline measurement results. The variation in the capacitance measurement method may due to non-uniform field distributions inside the ferrite slab [72]. The study in [72] showed that the capacitance method is less accurate for a sample with larger permeability and at higher measurement frequencies as the distortion in E- and H-field distributions are more pronounced.

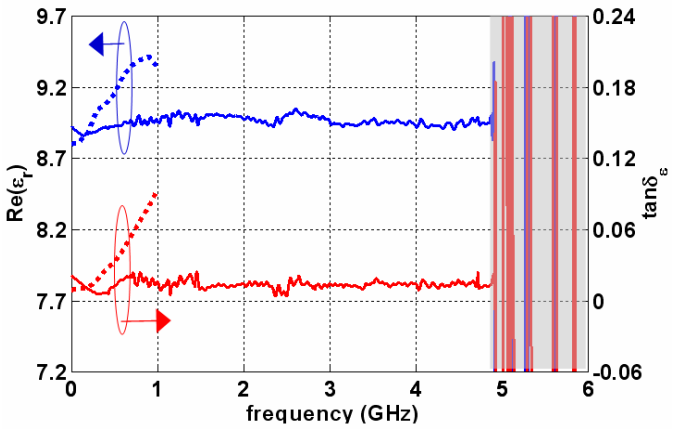

Figure 4.13: Measured Re(ε_r) and tanδ_ε of the NiZn ferrite slab. The dotted curves indicate the measured data from the impedance analyzer (Agilent E4991A with 16454A).

4.4.3 Characterization of Ferrite Slabs under DC Magnetic Field

If only the AC (or RF) magnetic field is applied on ferrites, the domain wall resonance is presented in the complex permeability spectra at relatively low frequencies [73]. A good example is the domain wall resonance at 250 MHz in Fig. 4.11. This resonance occurs when the frequency of the domain wall vibration is equal to the frequency of the AC magnetic field. On the other hand, the ferromagnetic resonance, resulting from the alignment of permanent magnetic moments, is presented when the DC magnetic field (DC biased field) is applied. Although this resonance usually appears at a relatively high frequency, the permeability spectra at the lower frequency range is also significantly affected.

Using the tapered stripline method, we examined the effect of external DC magnetic field on the permeability spectra. As can be seen in Fig. 4.14, the DC magnetic

field is applied by placing permanent magnets on the top and bottom conductors of the stripline. Noting that it is necessary to apply the DC magnetic field perpendicular to the AC magnetic field to harness the magnetic torque inside the ferrite. Three different configurations of permanent magnets were used in this experiment. The strength of the applied field for each configuration is described in the insets at the bottom. These values were measured with a Gauss meter (AlphaLab M1ST). The strength is not uniform along the sample height, therefore, both the values close to the magnet and at the middle of the stripline were measured.

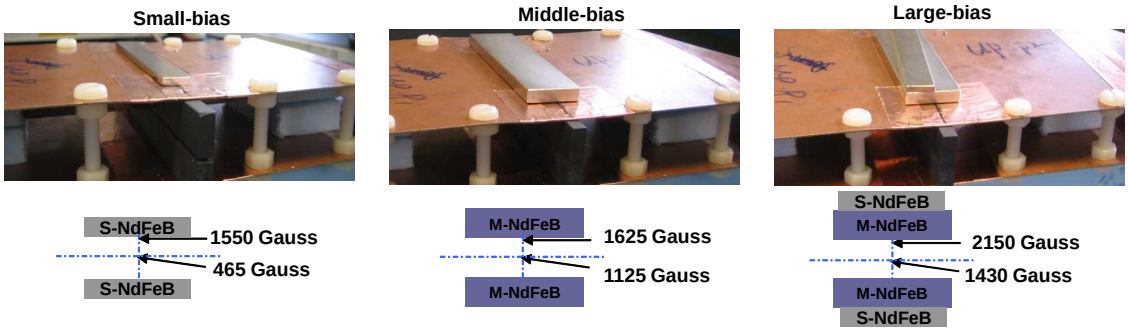

Figure 4.14: Measurement configurations with different strengths of DC magnetic field: (a) small, (b) middle, and (c) large biased field.

With the above set-up, two different ferrite slabs were characterized: spinel and garnet. They have distinguished formulas of compounds (e.g., $NiZnFe_2O_4$ and $Y_3Fe_5O_2$) led their applications in microwave unique [74]. Typically, The garnet families are used for low-loss applications and the spinels for high μ applications. However, their general properties do not hold when the DC magnetic field is applied and varied in

strength. Fig. 4.15 demonstrate how the permeability spectra is affected by the external DC field. As observed in the data for the spinel [Fig. 4.15(a) and (b)], in the absence of biased field, Re(μ_r) begins to decrease at about 230 MHz and Im(μ_r) has a maximum around 380 GHz. When the DC field is applied, Re(μ_r) at low frequencies decreases with increasing the strength. Also the obvious domain wall resonance shown for the zero-bias case is dispersed and flattened as stronger field is applied. Similar trends are shown in the garnet measurement data [Fig. 4.15(c) and (d)]. This phenomena can be explained by the magnetization mechanism of ferrites [75]. As the applied DC magnetic field decreases the domain walls, the permeability at low frequency is reduced. Simultaneously, the ferromagnetic resonance frequency is increased as the applied field is increased (i.e., magnetic dipoles are more aligned). Subsequetly, the ferromagnetic resonance at the upper frequency contributes to the permeability spectra to be flat at the low frequency range.

4.5 Limitation of the Tapered Stripline Method

Besides the operation frequency limit described in the previous sections, the accuracy of the tapered stripline method is restricted by the thickness of the sample. Since the electromagnetic wave primarily interacts with the sample along its thickness, the measured S-parameters cannot accumulate sufficient information for accurate deembedding of sample properties if the sample is too thin [76].

This limitation is demonstrated below using full-wave simulations. For this, the tapered stripline was numerically modeled, and the S-parameters were computed for several dielectric and magnetic samples with varying thickness from 150 μm to 6.5 mm. Fig. 4.16(a) and (b)shows the maximum error values in the simulated dielectric

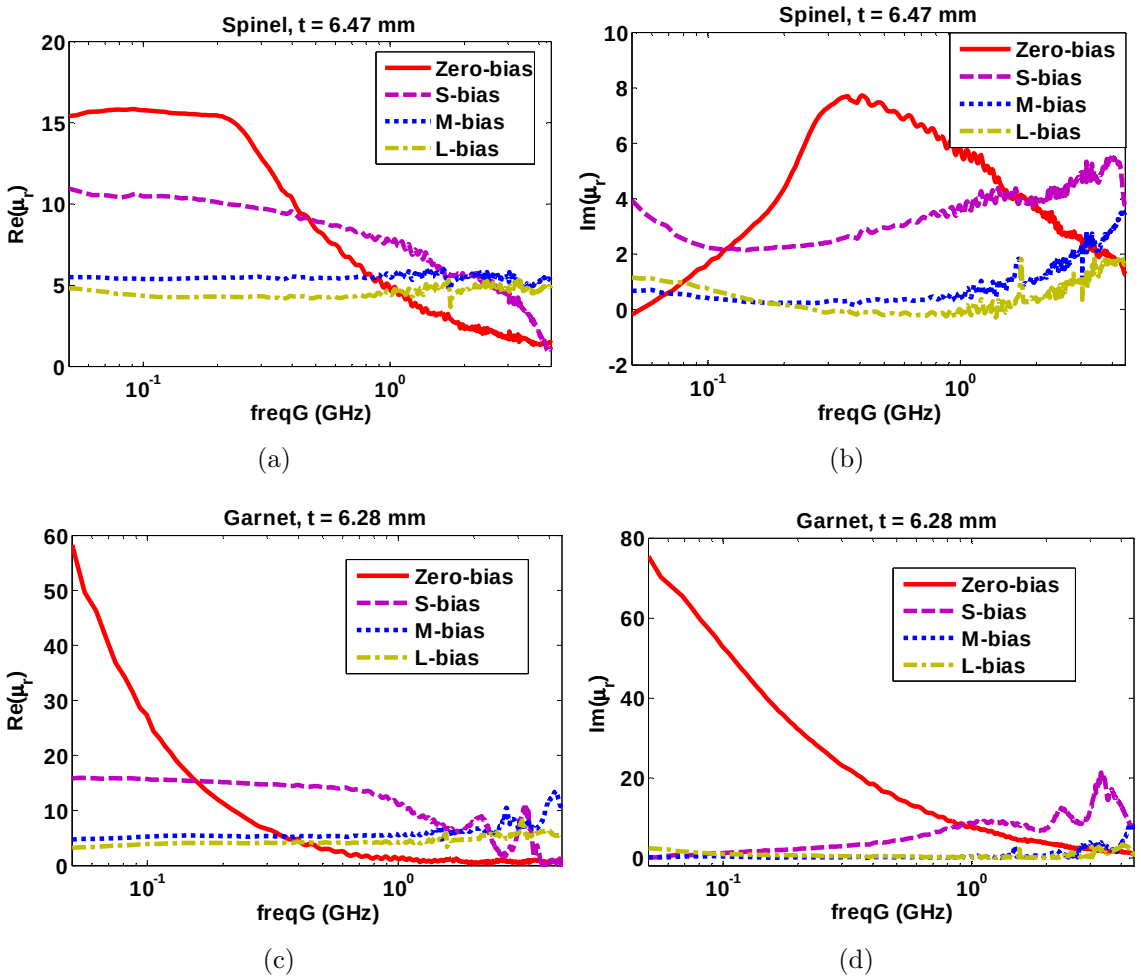

Figure 4.15: Real part and imagninary part of μ_r affected by the biased field: (a) real μ_r of spinel, (b) imaginary μ_r of spinel, (c) real μ_r of garnet, and (d) imaginary μ_r of garnet

and magnetic properties for various thickness values. Here, the error is calculated using

$$|\text{error}|\,(\%) = \left|\frac{S-K}{K}\right| \times 100,$$

where S and K refer to the simulated and known properties of the sample. As in Fig. 4.16, the maximum error exponentially increases as the thickness of the sample

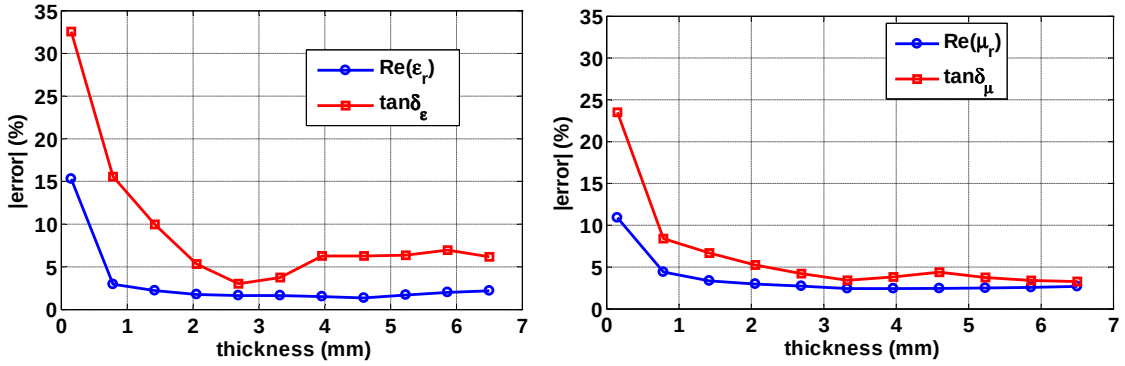

(a) (b)

Figure 4.16: Maximum error in de-embedded permittivity and permeability versus thickness of the sample.

decreases down to several hundreds of microns. For example, more than 5% and 10% errors are observed for $\mathrm{Re}(\varepsilon_r)$ (or $\mathrm{Re}(\mu_r)$) and loss-tangents, respectively, when the sample is thinner than 0.7 mm.

Another limitation of the tapered stripline method is that a rather large piece of sample is needed to sufficiently fill the tx-line cross-section. For instance, the proposed fixture requires a sample with the transverse dimension more than 10 cm to neglect the effect from the sample edges.

4.6 Summary

We described the material characterization technique utilizing a tapered stripline test fixture. With this technique, the broadband characteristic of material's ε and μ could be simultaneously characterized from the measured S-parameters. Compared to traditional measurement techniques, the proposed approach is simple in measurement process and requires less effort in the sample preparation and test fixture fabrication.

The design rules of tapered stripline discussed in section 4.2 are applicable to a new design for different frequency ranges or different sizes of sample. We also defined the operation frequency limit of the tapered stripline by observing the resonance of the higher order mode. The current stripline fixture is available up to 4.8 GHz, but the study showed that this upper frequency limit can be shifted toward a higher frequency by adjusting the height and width values of the stripline. Based on simulations, we showed that the errors in de-embedded results exponentially increase for a sample thinner than 1 mm. That is, the tapered stripline method is not feasible for the measurement of thin materials such as film type composites. With this issue in mind, in the next chapter, we develop a microstrip line based characterization method for thin material composites.

Chapter 5

MICROSTRIP LINE METHOD FOR THIN COMPOSITES

The limitation in the measurable sample thickness of the tapered stripline method (Chapter 4) led to develop a new T/R technique based on a microstrip line structure for the characterization of in-plane properties of thin composites (thickness $t < 1$ mm). In this method, a thin composite is conveniently placed on a flat sample holder and the S-parameters are measured along the length of the sample surface. As mentioned in Chapter 2.4, such Type-II T/R configuration provides better interactions between a thin sample and the propagating electromagnetic waves so that the insensitivity issue for Type-I T/R methods can be avoided. However, a secondary de-embedding process must be incorporated with the proposed measurement set-up as the cross-section of the microstrip line is not completely-filled with the sample but consists of air, substrate, and sample. Herein, we develop a new secondary de-embedding algorithm by means of full-wave simulations. Utilizing the full-wave simulated data, instead of conventional quasi-static solutions, enable us to measure not only thin but small samples.

5.1 Introduction

Thin film composites has received growing attentions for the improvement of microwave applications. With advanced deposition techniques, multiple layers of thin films can be stacked and patterned on substrates for circuitry and antennas. Also their flexible forms are suitable for conformal installation on curved surface such as radomes. On the material viewpoint, some composites are required to be in the form of thin film. For instance, magnetic composites are very thin (maximum a few hundreds of micron) to suppress the eddy current loss originating from their low resistance at microwave frequency [1]. Moreover, their film surface is often patterned to further suppress in-plane eddy current by introducing in-plane anisotropy [4, 5, 77, 78].

In light of recent research on thin film composites, a measurement system for accurate material property characterization is necessary. In particular, for microwave applications, the characterization of in-plane ε and μ is often required since the fields are applied parallel to the surface of the associated composites. Conventional thin film characterization systems utilize planar tx-lines [26, 44–46, 79] as illustrated in Fig. 5.1. Typically, the film is deposited under or over the center conductor of a microstrip line or a coplanar waveguide, and ε and μ are de-embedded from the S-parameters measured along the length of the sample surface (y-direction in Fig. 5.1). As observed in the field distributions, the in-plane μ can be characterized since the H-field illuminates the film surface and such in-plane interactions are captured in the S-parameters. However, since the E-field is primarily vertical to the sample thickness, the characterization of in-plane ε cannot be carried out with the illustrated measurement set-ups.

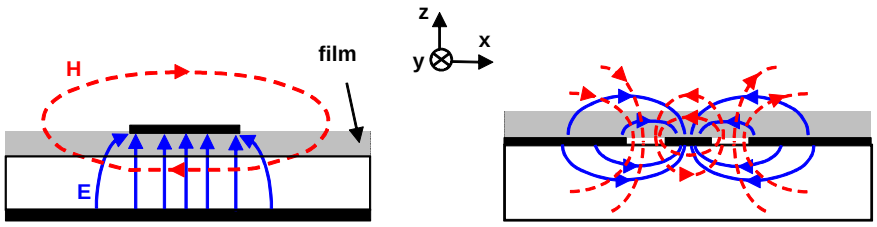

Figure 5.1: Cross-section field distributions of conventional planar transmission line methods: (a) microstrip line and (b) coplanar waveguide.

Alternatively, the arrangement of sample and planar tx-line can be modified to realize the broadband characterization of in-plane ε and μ. Specifically, we propose two individual microstrip line fixtures, as shown in Fig. 5.2(a) and (b). With such field-sample alignments, the sample surface is uniformly illuminated by the E- and H-fields, respectively. For the in-plane ε characterization [see Fig. 5.2(a)], the film is vertically standing between the ground and the upper conductor whose width is adequately narrow to detect slight E-field perturbation along the sample. In contrast, the microstrip line for the in-plane μ characterization [see Fig. 5.2(b)] employs a rather broad upper conductor to uniformly excite the H-field onto the film surface. As the cross-section of the proposed set-ups are a combination of air-holder-sample, the initially de-embedded ε or μ from the measured S-parameters is not the actual sample properties but includes the surrounding effects. Again, such type-II T/R method must employ a secondary de-embedding process to separate the properties of the sample from the "raw" data. The latter refers to the initial ε and μ that includes all interactions with air-holder-sample.

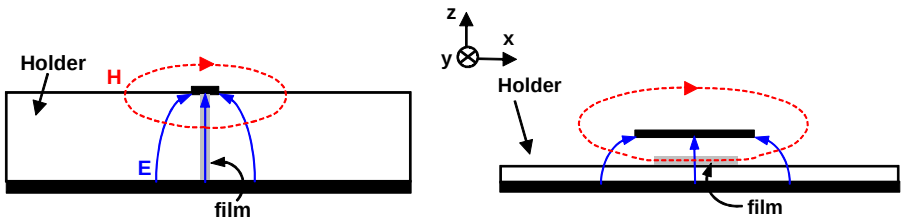

(a) (b)

Figure 5.2: Proposed microstrip line structures for (a) in-plane ε and (b) in-plane μ measurements.

5.2 ε and μ De-embedding Process

As we pursue the determination of ε and μ using two individual microstrip line fixtures, only the measurement of one S-parameter, either a reflection (S_{11}) or transmission (S_{21}) coefficient, is required for each fixture. Although the reflection-only technique [46,79] is commonly used due to its simplicity in measurement, the transmission-only technique [80,81] is known for better accuracy. Specifically, compared to the S_{11} measurement, the S_{21} is less affected by the position offset of a sample inside the tx-line. Moreover, the dynamic range of S_{21} measurement is larger than that of S_{11}, so that small perturbation from the insertion of small and thin samples can be captured with more precision. As we decided to use the S_{21} to take advantage of the above aspects, in the following, the de-embedding process of ε (or μ) from the measured S_{21} is discussed.

5.2.1 De-embedding of Raw Parameters

As a reminder, we indicate the initial ε (or μ) de-embedded from S_{21} as the "raw" parameters. The raw parameters include the interaction of E- and H-field not only

with the sample but also with the air and holder material. In microstrip line theory, it is often referred to as the "effective" ε (or μ). However, this term can be confused with the same terminology in the effective medium theory (EMT) [82]. As the EMT will be introduced later in this chapter, we use the term "raw" instead of "effective" through out this chapter.

The raw parameters can be retrieved using the NRW process discussed in Chapter 2.4. These closed-form equations offer direct calculation of ε and μ. On the other hand, the NRW process requires a special care if the length of the sample corresponds to one half of the wavelength in the sample. Specifically, the integer multiple of the phase term of $1/\tau$ in (2.46) must be chosen properly to avoid phase wrapping. For the broadband measurement of a sample with low-loss and short length, it is difficult to rule out this ambiguity. Instead of using the NRW process, therefore, an iterative solver is often employed in the de-embedding algorithm [18, 76]. The iterative solver is also suitable when only one S-parameter, either S_{21} or S_{11}, is provided, which is the case for our microstrip line method.

Let us first derive the equations relating ε (or μ) to the measured S_{21} from fundamental tx-line analyses. A general type-II T/R set-up is depicted in Fig. 5.3. This is similar to Fig. 2.11 in Chapter 2.4 except for the sample section is filled with sample-air-holder. The wave propagation constants in the empty (γ_e) and sample (γ_s) sections are given by

$$\gamma_e = jk_0\sqrt{\mu_{re}\varepsilon_{re}}, \tag{5.1}$$

$$\gamma_s = jk_0\sqrt{\mu_{Rs}\varepsilon_{Rs}}, \tag{5.2}$$

where k_0 is the wave propagation constant in the free-space, and μ_{re} and ε_{re} are the permeability and permittivity of the empty section. Otherwise, μ_{Rs} and ε_{Rs} are

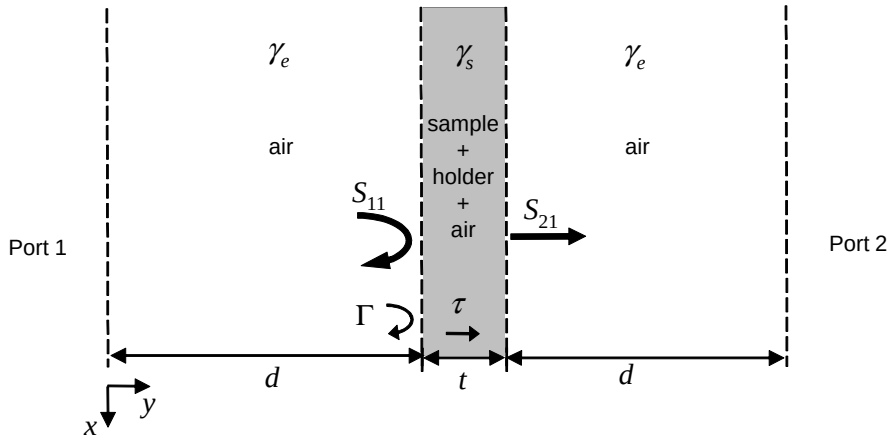

Figure 5.3: General set-up for type-II T/R method.

the raw permeability and permittivity in the sample section with the subscript "Rs" referring to the raw parameters. We will use a subscript "rs" later to express the permeability and permittivity of the sample itself. Since the empty section is filled with the air, μ_{re} is equal to 1, but ε_{re} may not be equal to 1 due to the fringing field occurring at the edges of the center conductor, namely the structural effect discussed in Chapter 2.4.. Thus, we will continue to derive equations with $\mu_{re} = 1$ and $\varepsilon_{re} \neq 1$. Similar to (2.37), the analytical solution for S_{21} is given by

$$S_{21} = \exp\left(-2\gamma_e d\right)\left[\frac{\tau\left(1-\Gamma^2\right)}{1-\Gamma^2\tau^2}\right], \tag{5.3}$$

where

$$\tau = \exp\left(-\gamma_s t\right), \tag{5.4}$$

$$\Gamma = \frac{\gamma_e \mu_{Rs} - \gamma_s}{\gamma_e \mu_{Rs} + \gamma_s}. \tag{5.5}$$

Substituting (5.1) and (5.2) into (5.3)-(5.5) provides

$$S_{21} = \exp\left(-j2k_0 d\sqrt{\varepsilon_{re}}\right)\left[\frac{\tau\left(1-\Gamma^2\right)}{1-\Gamma^2\tau^2}\right], \tag{5.6}$$

$$\tau = \exp\left(-jk_0 t\sqrt{\mu_{Rs}\varepsilon_{Rs}}\right), \tag{5.7}$$

$$\Gamma = \frac{\sqrt{\mu_{Rs}\varepsilon_{re}} - \sqrt{\varepsilon_{Rs}}}{\sqrt{\mu_{Rs}\varepsilon_{re}} + \sqrt{\varepsilon_{Rs}}}. \tag{5.8}$$

For the in-plane ε set-up in Fig. 5.2(a), μ_{Rs} can be approximated to 1 as the holder is made of a non-magnetic material (e.g., Acrylic) and as the H-field is hardly perturbed by the permeability along the film thickness (off-plane μ). With these assumptions, (5.6)-(5.8) are re-written by

$$S_{21\varepsilon} = \exp\left(-j2k_0 d\sqrt{\varepsilon_{re}}\right)\left[\frac{\tau_\varepsilon\left(1-\Gamma_\varepsilon^2\right)}{1-\Gamma_\varepsilon^2\tau_\varepsilon^2}\right], \tag{5.9}$$

$$\tau_\varepsilon = \exp\left(-jk_0 t\sqrt{\varepsilon_{Rs}}\right), \tag{5.10}$$

$$\Gamma_\varepsilon = \frac{\sqrt{\varepsilon_{re}} - \sqrt{\varepsilon_{Rs}}}{\sqrt{\varepsilon_{re}} + \sqrt{\varepsilon_{Rs}}}. \tag{5.11}$$

where the subscript "ε" indicates parameters for the in-plane ε characterization. Likewise for the in-plane μ set-up in Fig. 5.2(b), ε_{Rs} is hardly perturbed by the permittivity along the film thickness (off-plane ε). That is, ε_{Rs} can be approximated to ε_{Rh}, the raw permittivity without the film (holder only). Substituting ε_{Rs} in (5.6)-(5.8) to ε_{Rh} provides

$$S_{21\mu} = \exp\left(-j2k_0 d\sqrt{\varepsilon_{re}}\right)\left[\frac{\tau_\mu\left(1-\Gamma_\mu^2\right)}{1-\Gamma_\mu^2\tau_\mu^2}\right], \tag{5.12}$$

$$\tau_\mu = \exp\left(-jk_0 t\sqrt{\mu_{Rs}\varepsilon_{Rh}}\right), \tag{5.13}$$

$$\Gamma_\mu = \frac{\sqrt{\mu_{Rs}\varepsilon_{re}} - \sqrt{\varepsilon_{Rh}}}{\sqrt{\mu_{Rs}\varepsilon_{re}} + \sqrt{\varepsilon_{Rh}}}. \tag{5.14}$$

Similar to in-plane ε set-up, the subscript "μ" refers to the equations for the in-plane μ characterization.

(5.9)-(5.11) and (5.12)-(5.14) are the equations implemented in an iterative solver to find the solutions for ε_{Rs} and μ_{Rs}, respectively. To obtain ε_{Rs} from (5.9)-(5.11), two different S_{21} measurements are needed as two unknowns (i.e., ε_{re}, ε_{Rs}) are presented in the equations. First of all, ε_{re} can be calculated from the S_{21} measured with an empty line (S_{21}^{e}). The analytical solution of S_{21}^{e} is written by

$$S_{21}^{e} = \exp\left[-jk_0\left(2d+t\right)\sqrt{\varepsilon_{re}}\right]. \tag{5.15}$$

Subsequently, ε_{re} is obtained from (5.15) as

$$\varepsilon_{re} = \frac{1}{k_0^2\left(2d+t\right)^2}\ln\left(\frac{1}{S_{21}^{e}}\right). \tag{5.16}$$

Once ε_{re} is known, the right hand side of (5.9) becomes a function of ε_{Rs} only. In the iterative solver, an initial estimate of ε_{Rs} is given and continuously updated for each iteration until the analytical S_{21} matches to the measured S_{21}.

In the equations for the in-plane μ set-up, (5.12)-(5.14), three S_{21} measurements are required as three unknowns are presented (ε_{re}, ε_{Rh}, μ_{Rs}). Same to the in-plane ε case, ε_{re} is obtained from the measurement of the empty line. Another unknown ε_{Rh} can be determined from the S_{21} measured with the holder only. Finally, with the knowledge of ε_{re} and ε_{Rh}, the iterative solver is used to determine μ_{Rs} in (5.12).

5.2.2 De-embedding of Sample Parameters

Having solved for the raw parameters (ε_{Rs} and μ_{Rs}), a secondary de-embedding process is then used to calculate the sample's parameters (ε_{rs} and μ_{rs}). A secondary de-embedding process can be developed by finding a mathematical relation of ε_{rs} (or μ_{rs}) to ε_{Rs} (or μ_{Rs}). Traditionally, their relationship is estimated by the so-called "filling factor" in the quasi-static planar tx-line analyses such as conformal mapping

[83] and variational method [84]. However, the quasi-static solutions are valid only when the sample's length is infinitely long in the x-direction (see the coordinate convention in Fig. 5.2). As our microstrip line geometries contain a small sample with a finite length in the x-direction, we proceed to formulate the mathematical relation based on full-wave simulation data. That is, the filling factor is numerically determined by curve fitting a set of data from full-wave simulations.

Firstly, a fit function that relates ε_{Rs} and μ_{Rs} to ε_{rs} and μ_{rs} must be formulated. This can be done by approximating the microstrip line problems to a lumped capacitor or inductor model. Let us first consider the in-plane ε set-up. Fig. 5.4(a) and (b) depict the E-field lines and their corresponding capacitances for the set-ups with and without the film. C_s denoted in Fig. 5.4(a) is the capacitance per unit length along the film. C_h in Fig. 5.4(b) also represents the capacitance at the same location as C_s but in the absence of the film (i.e., the area is filled with the holder material). If we assume the E-field is not significantly perturbed by the thin and small film, the total capacitances in the cross-section of Fig. 5.4(a) and (b) are given by

$$C_s^{tot} = C_s + C_1 + C_2 + \cdots + C_n, \tag{5.17}$$

$$C_h^{tot} = C_h + C_1 + C_2 + \cdots + C_n, \tag{5.18}$$

where $C_1, C_2, \cdots, C_n$ are independent shunt capacitances in the other E-field lines. Subtracting (5.18) from (5.17) yields

$$C_s^{tot} - C_h^{tot} = C_s - C_h. \tag{5.19}$$

As the capacitance is proportional to permittivity, (5.19) may be re-written in terms of permittivity values. That is,

$$\varepsilon_{Rs} - \varepsilon_{Rh} = p\left(\varepsilon_{rs} - \varepsilon_{rh}\right), \tag{5.20}$$

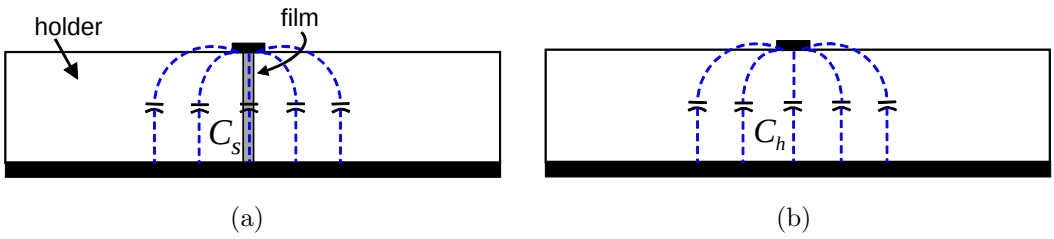

Figure 5.4: Lumped capacitance models for the in-plane ε characterization set-up: (a) with the film and (b) without the film.

where p is the frequency dependent coefficient that relates the capacitance to the corresponding permittivity values. This coefficients is determined by full-wave simulations and subsequent curve fitting. That is, for a given sample size, a set of ε_{Rs} with different ε_{rs} values are collected from a full-wave simulation tool, and these data are used in (5.20) to determine p. As in (5.20), a linear fit function can be used to search p in a curve fitting computer code (e.g., implemented with Matlab). Subsequently, the computed p is used to determine ε_{rs} from the measured ε_{Rs} using

$$\varepsilon_{rs} = \frac{1}{p}\left(\varepsilon_{Rs} - \varepsilon_{Rh}\right) + \varepsilon_{rh}, \tag{5.21}$$

Unlike the in-plane ε, the in-plane μ of the film cannot be de-embedded from a linear curve fitting model. As can be seen in Fig. 5.5, inductances are arranged not only in a parallel but in a series manner. Instead, it is found that a rational fit function with two unknown coefficients can be used. This rational function is derived by approximating the H-field interactions with lumped inductors. Assuming the H-field lines are not significantly perturbed by the film, the total inductances in the

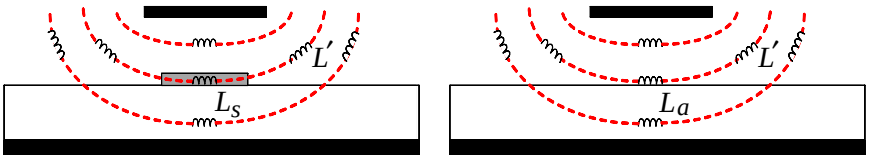

(a) (b)

Figure 5.5: Lumped inductance models for the in-plane μ measurement set-up: (a) with the film and (b) without the film.

cross-section of Fig. 5.5(a) and (b) are given by

$$\frac{1}{L_s^{tot}} = \frac{1}{L_s + L'} + \frac{1}{L_1} + \frac{1}{L_2} + \cdots + \frac{1}{L_n}, \tag{5.22}$$

$$\frac{1}{L_a^{tot}} = \frac{1}{L_a + L'} + \frac{1}{L_1} + \frac{1}{L_2} + \cdots + \frac{1}{L_n}, \tag{5.23}$$

where L' refers to the series inductance connected with L_s or L_a along the same H-field line. All other inductive factors, $L_1, L_2, \cdots, L_n$, are independent shunt inductances in the remaining H-field lines. Subtracting (5.23) from (5.22) yields

$$\frac{1}{L_s^{tot}} - \frac{1}{L_a^{tot}} = \frac{1}{L_s + L'} - \frac{1}{L_a + L'}. \tag{5.24}$$

As the inductance is proportional to permeability, we can rewrite (5.24) in terms of permeability values. To do so, we introduce the following coefficients to correlate the inductances to their corresponding permeability values:

$$q_1 = \frac{L_s}{\mu_{rs}} = \frac{L_a}{\mu_{ra}}; \quad q_2 = \frac{L'}{\mu'_r}; \quad q_3 = \frac{L_s^{tot}}{\mu_{Rs}} = \frac{L_a^{tot}}{\mu_{Ra}}, \tag{5.25}$$

where μ_{Rs} and μ_{Ra} are the raw permeabilities for the microstrip lines with the film and without the film. Otherwise, μ_{rs} and μ_{ra} are the permeabilities of the film and air, respectively. Using these coefficients together with $\mu_{Ra} = \mu_{ra} = \mu'_r = 1$ (i.e., air

and non-magnetic holder), (5.24) becomes

$$\mu_{Rs} = \frac{\mu_{rs} + \frac{q_2}{q_1}}{\mu_{rs}\left(1 - \frac{q_3}{q_1+q_2}\right) + \frac{q_2}{q_1} + \frac{q_3}{q_1+q_2}}. \tag{5.26}$$

(5.26) can be further simplified by introducing new variables $p_1 = q_2/q_1$ and $p_2 = q_3/q_1$:

$$\mu_{Rs} = \frac{\mu_{rs}\,(1+p_1) + p_1\,(1+p_1)}{\mu_{rs}\,(1+p_1-p_2) + p_1\,(1+p_1) + p_2}, \tag{5.27}$$

The above gives the raw permeability in terms of the sample's permeability and two unknown coefficients, (p_1, p_2). These coefficients are determined by curve fitting full-wave simulation data with a rational fit function as in (5.27). After solving for (p_1, p_2), μ_{rs} is de-embedded from the measured μ_{Rs} with

$$\mu_{rs} = \frac{p_2\mu_{Rs} - p_1\,(1+p_1)\,(1-\mu_{Rs})}{p_2\mu_{Rs} + (1+p_1)\,(1-\mu_{Rs})}, \tag{5.28}$$

Hence, the permeability of the sample can be de-embedded from the measured μ_{Rs} with the numerically determined (p_1, p_2). Demonstration of the de-embedding process is given in the measurement section.

5.3 Microstrip Line Design

Prior to the de-embedding process, the S_{21} data must be accurately measured using properly designed microstrip lines. Illustrations of the actual microstrip line set-ups are shown in Fig. 5.6(a) and (b) for the ε and μ characterization. The prepared film is placed in between (for ε) or over (for μ) the Acrylic holder, and then inserted under the upper conductor. The figures also describe the way to characterize a film with in-plane anisotropy. For example, the E- and H-fields can be excited along different axes of the film by rotating it.

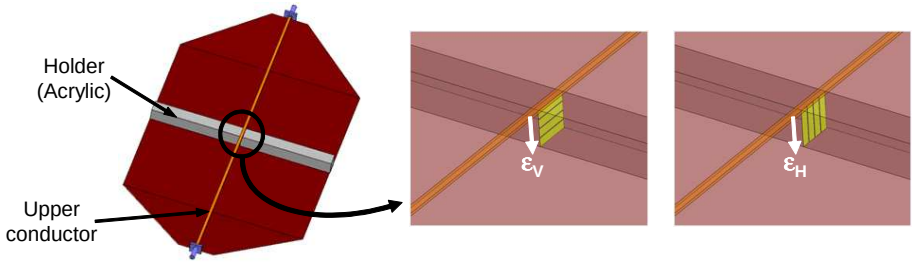

(a)

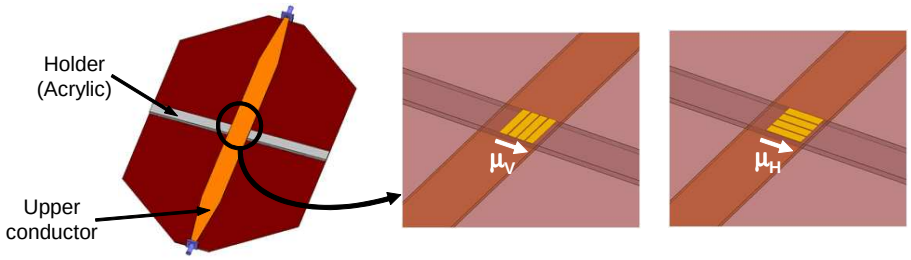

(b)

Figure 5.6: Illustration of microstrip line set-ups for (a) in-plane ε and (b) in-plane μ characterization.

The most critical design parameter for these microstrip lines is the width of the upper conductor. As mentioned in the introduction, narrow and broad upper conductors are needed for ε and μ characterizations. We used a full-wave simulation tool (Ansoft HFSS) to investigate the effect of the upper conductor width on the de-embedded results. Based on this study, the optimized width values were carried out and used in the actual designs.

5.3.1 Microstrip Line for In-plane ε

In general, the width of the upper conductor is determined to match the characteristic impedance of the microstrip line to the port impedance (e.g., 50 Ω). Assuming the height of the microstrip line is 1 cm to characterize a film with a size of 1 cm $\times$

1 cm, the width of the upper conductor should be around 47 mm to achieve 50 Ω match [83]. However, such broad upper conductor is not suitable for our in-plane ε set-up, since the field is mostly concentrated on the edges of the conductor, while the film is positioned under the middle of the conductor.

This issue is illustrated in Fig. 5.7(a), which show the simulated surface current distributions at the upper conductors with different width values (w_1). For the upper conductor with $w_1 = 47.7$ mm, the current is concentrated on the edges. As a result, the magnitude of the E-field is much weaker at the middle of the conductor compared to the edges as shown in Fig. 5.7(b). With such weak E-field, it may not be able to detect slight perturbation caused by the inserted thin film. To resolve this problem, the width of the upper conductor is reduced as shown in the successive current and E-field distribution plots in Fig. 5.7(a) and (b). As can be seen, the surface current (or E-field) is more concentrated at the middle of the upper conductor for the narrower upper conductor. Fig. 5.8 provides a better comparison of this effect by plotting the the E-field magnitudes across "Line 1" denoted in Fig. 5.7(b). Note that all curves in Fig. 5.8 are normalized to the E- field magnitude of $w_1 = 47.7$ mm at $x = 0$. As observed, the E-field is uniformly distributed along the observation line for the wide conductor ($w_1 = 47.7$ mm) and tightly concentrated for the narrow one ($w_1 = 2$ mm). It is worth noting that the reduce of the upper conductor width generates significant mismatch at the ports as the microstrip line characteristic impedance greatly exceeds the port impedance. However, such mismatch can be minimized using the TRL calibration technique similar to the tapered stripline method in Chapter 4.

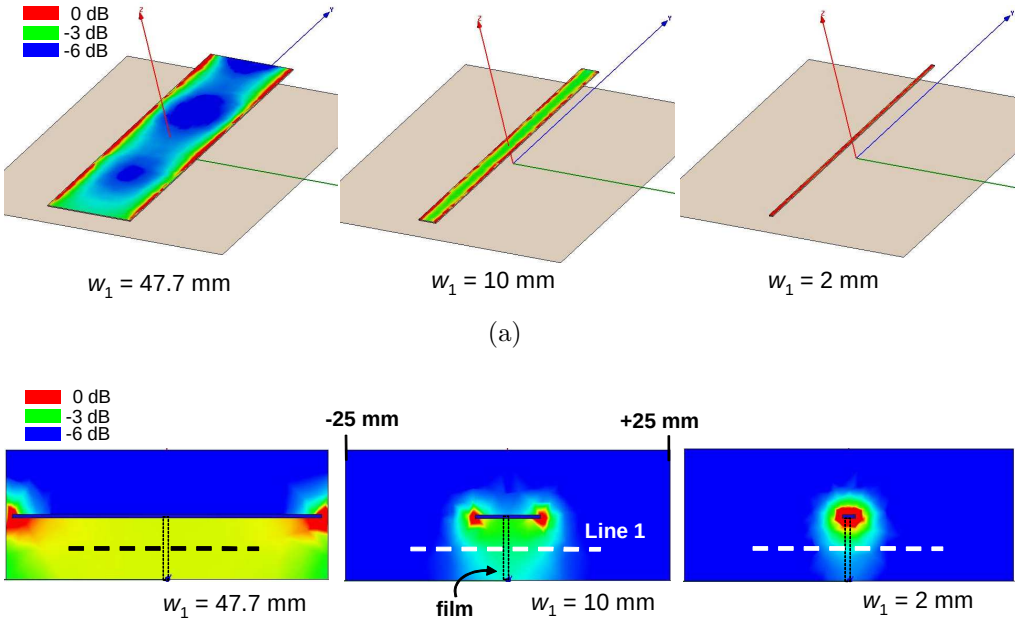

Figure 5.7: Simulated data of (a) the magnitude of surface current (3D view) and (b) the magnitude of the E-field (cross-sectional view).

Next, let us compare the raw permittivity data (ε_{Rs}) de-embedded from the simulated S_{21} with different conductor widths. Fig. 5.9(a) and (b) show the raw permittivities obtained from microstrip lines with 2 mm and 10 mm upper conductors, respectively. ε_{rs} values next to each curve refer to the sample permittivities assigned in the simulations. The size of the sample was 1 cm $\times$ 1 cm $\times$ 150 μm. As observed, the dynamic range of ε_{Rs} measured with $w_1 = 2$ mm conductor is much wider than the $w_1 = 10$ mm case. This implies the narrower conductor is less affected by errors during the measurement. If the dynamic range is small, for example, a slight error in the measured S_{21} may mislead the interpretation of the de-embedded ε_{Rs} to the adjacent value.

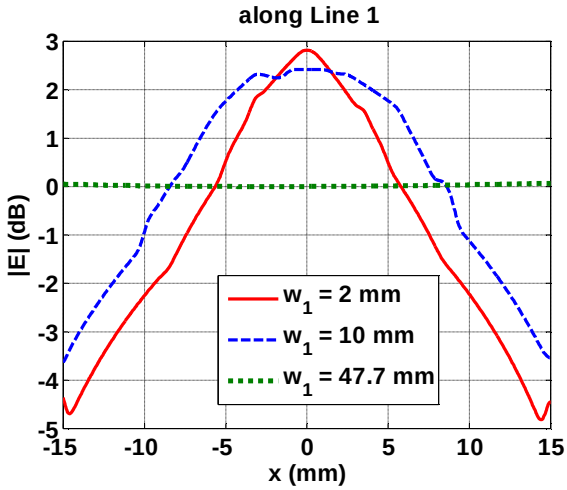

Figure 5.8: The magnitude of E-field along "Line 1" for different width values. All curves are normalized to the magnitude of $w_1 = 47.7$ mm at $x = 0$.

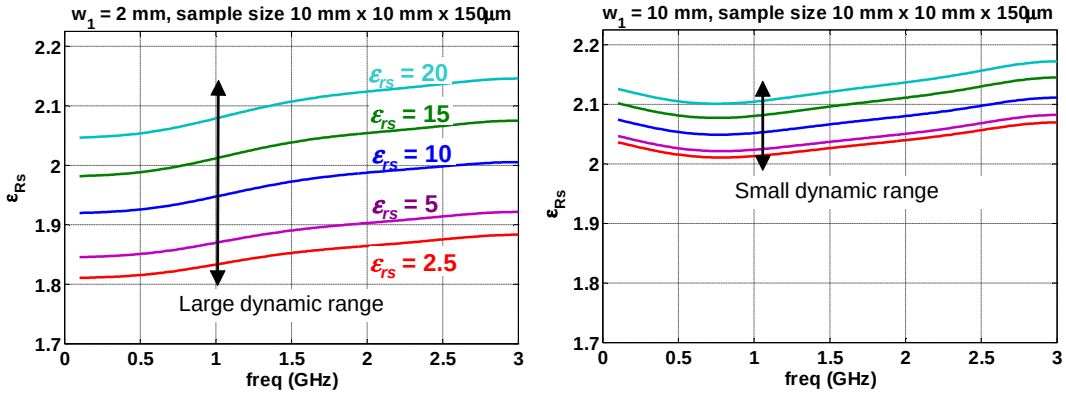

(a) (b)

Figure 5.9: De-embedded ε_{Rs} by varying ε_{rs} using (a) a 2 mm upper conductor and (b) a 10 mm upper conductor.

The above simulation studies indicate that better field concentration and larger dynamic range can be achieved using a narrower upper conductor. However, in the

real world, a narrow conductor can be easily bent and misaligned so that the calibration or measurement results may have poor repeatability. Therefore, a trade off between accuracy, manufacturing capability, and measurement repeatability should be considered. A 2 mm wide upper conductor was chosen for our microstrip line design considering these aspects.

5.3.2 Microstrip Line for In-plane μ

For the in-plane μ measurement set-up, the H-field should uniformly excite the film surface. This matter is the primary concern in the characterization of inhomogeneous composites (e.g., patterned film). Using the full-wave simulation tool, therefore, we checked the uniformity of the H-field along the length of the film with different the upper conductor widths (w_2). In this study, the height of the microstrip line was fixed to 3 mm. For this, noting that 50Ω match can be provided when $w_2 = 14.3$ mm. However, such mismatch effect was not considered since TRL calibration was used to remove it. Similar to the analysis for the in-plane ε microstrip line, the magnitudes of the H-field with different w_2 values were observed as in Fig. 5.10. Also, the normalized H-field magnitudes along "Line 2" are depicted in Fig. 5.11. Note that the length of Line 2 is 1 cm which corresponds to the length of the sample. Also, the data in Fig. 5.11 are normalized to the magnitude of $w_2 = 24$ mm conductor at $x = 0$. As in Fig. 5.11, the narrower conductor provides the higher H-field magnitude, but the better field uniformity is provided for broader upper conductor value.

The dynamic ranges of raw permeabilities (μ_{Rs}) obtained from the simulated S_{21} with different conductor widths (14 mm and 24 mm) are compared in Fig. 5.12. The similar trend as in the study of the in-plane ε set-up can be observed: the narrower

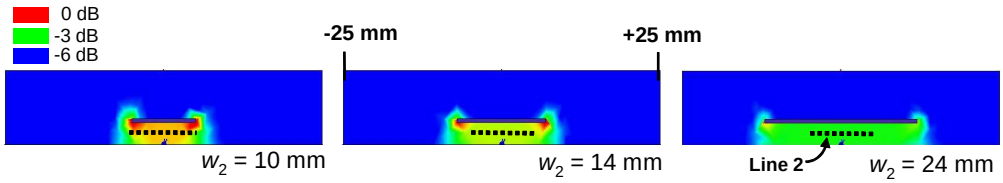

Figure 5.10: Magnitude of the H-field with different upper conductor width values.

conductor offers a larger dynamic range. Based on the simulation study, the width of the upper conductor for the in-plane μ set-up needs be chosen with respect to two opposite criteria: 1) the width should be broad enough for uniform illumination, but 2) it should be narrow enough to provide large dynamic range. We selected a conductor width of $w_2 = 14$ mm in our microstrip line design considering this trade off. With $w_2 = 14$ mm, a rather uniform H-field distribution is provided as in Fig. 5.10, and the dynamic range is reasonably wide as in Fig. 5.12(a).

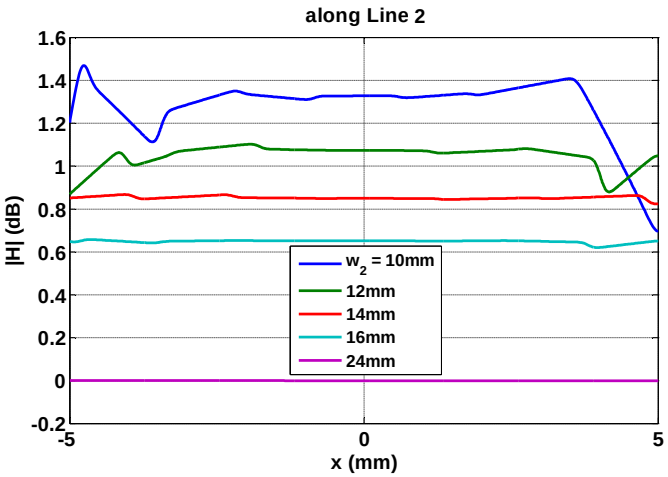

Figure 5.11: Magnitude of H-field along "Line 2" for different width values. All curves are normalized to the magnitude of $w_2 = 24$ mm at $x = 0$.

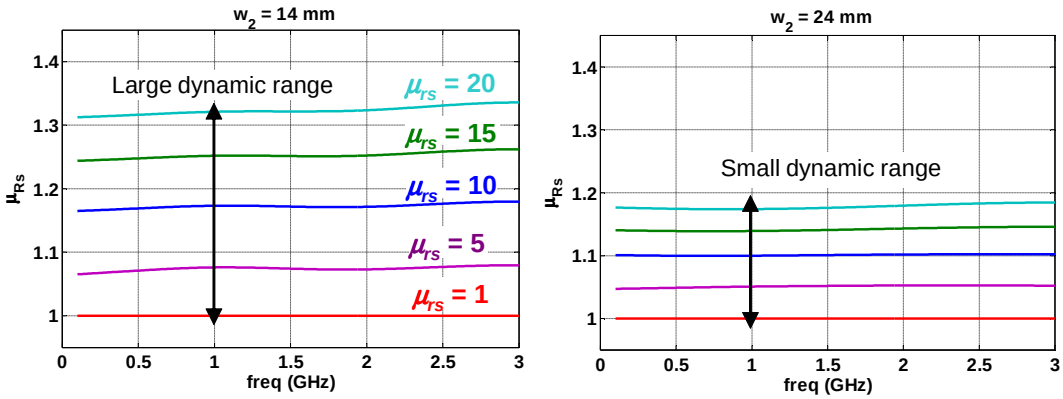

(a) (b)

Figure 5.12: De-embedded μ_{Rs} by varying μ_{rs} using (a) a 14 mm upper conductor and (b) 24 mm upper conductor.

5.4 Measurement Demonstration

The overall measurement and de-embedding procedures are arranged in a flow chart as in Fig. 5.13. Following the procedure, the in-plane ε and μ of a patterned magnetic alloy film was characterized. Since the measured data is not allowed to be published (by the film manufacturer), only the measurement procedure and brief error analysis of the results are discussed. To avoid such restriction, we collaborated with Material Science Department in the Ohio State University to manufacture patterned ferrite films. The detailed analyses for the characterization of the patterned ferrite films are provided in this section.

5.4.1 Characterization of Patterned Magnetic Alloy Films

A thickness of 150 μm patterned magnetic alloy film was characterized using the set-up as depicted in Fig. 5.14. The film was prepared in the size of 1 cm $\times$ 1 cm, and then sandwiched by the Acrylic holder for in-plane ε measurement and placed

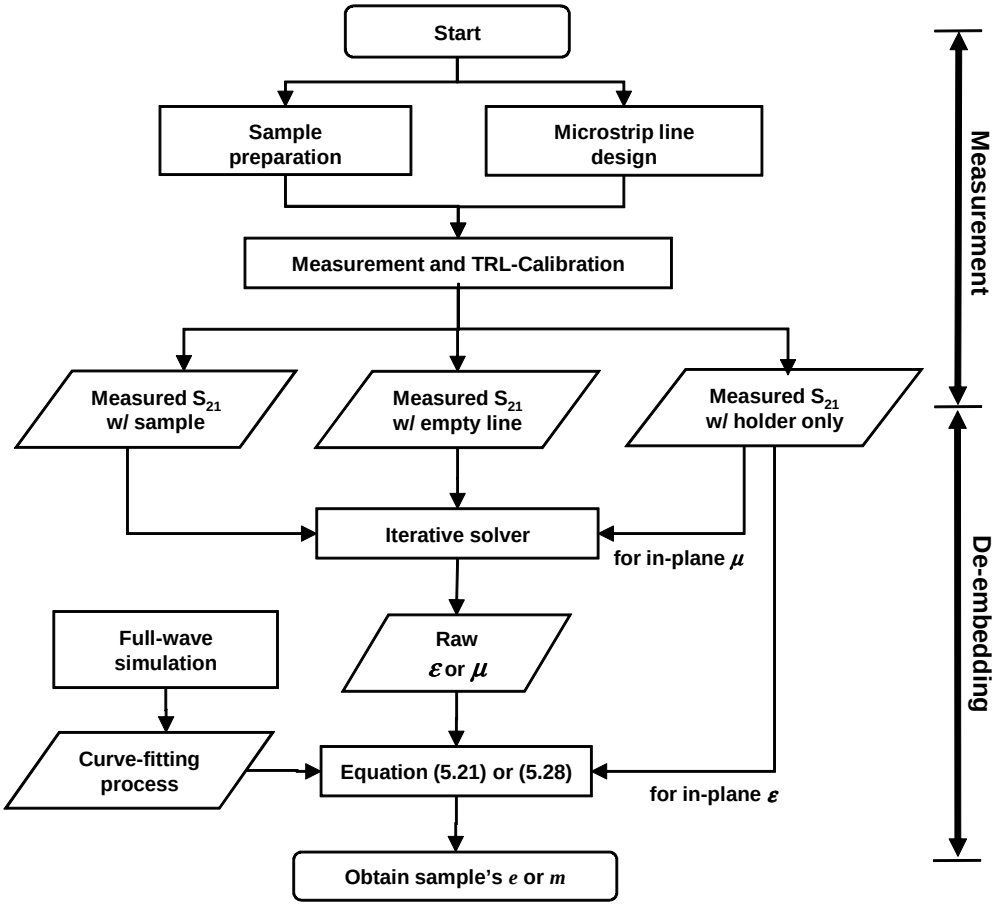

Figure 5.13: Flow chart of the measurement and de-embedding procedures for the microstrip line method.

over the Acrylic bar for in-plane μ measurement. The microstrip lines consist of the upper conductor width of 2 mm and 14 mm for each configuration. With these set-ups, the largest errors in the de-embedded in-plane ε and μ were 5.4% and 3.7% from the known values. On the other hand, the errors in dielectric- and magnetic-loss factors (i.e., $\tan\delta_\varepsilon$ and $\tan\delta_\mu$) were 10.8% and 7.2%. The higher error in the loss measurements is typical for T/R methods as discussed in Chapter 2.4. Moreover, these error values are higher than the loss measurement error in the tapered stripline

method (Chapter 4) as the half-opened structure of the microstrip line generates more radiation loss compared to the relatively closed stripline structure.

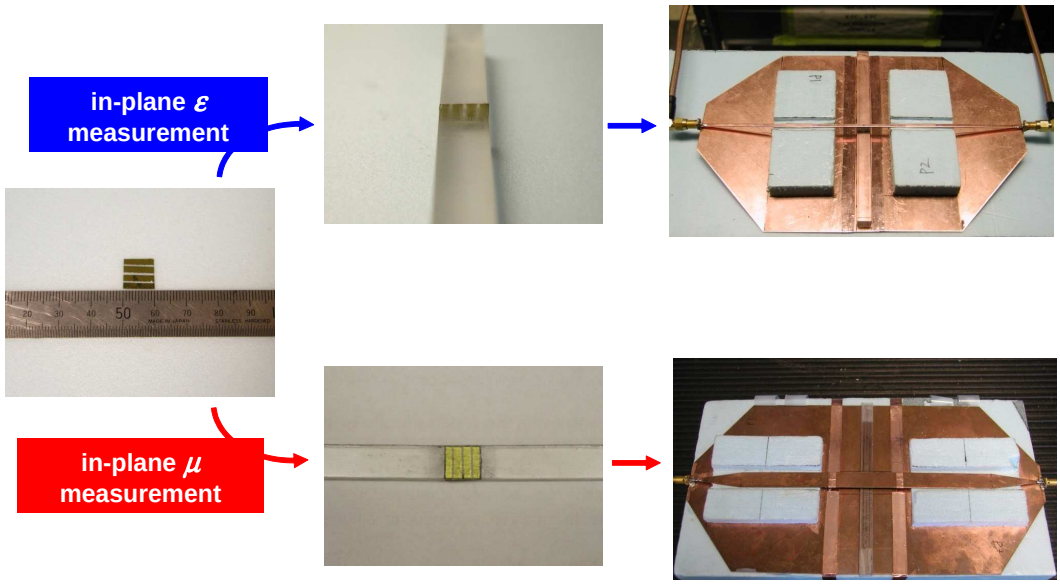

Figure 5.14: Pictures of measurement set-ups for a patterend magnetic alloy film: (a) in-plane ε and (b) in-plane μ.

5.4.2 Characterization of Patterned Ferrite Films

We proceeded to characterize a patterned ferrite composite whose geometry is shown in Fig. 5.15. The films were prepared by filling the gaps between magnetic material strips (ferrite) with dielectric materials (PDMS). With such patterned geometry, the measured in-plane μ is expected to present in-plane anisotropy depending on the direction of the applied H-field. Herein, two patterned ferrite composites were fabricated and characterized. These corresponded to NiCo-PDMS and NiZn-PDMS

composites. Note that the thicknesses of the NiCo-PDMS and NiZn-PDMS composites were 480 μm and 610 μm, respectively. Also, the volume ratios of the NiCo and NiZn ferrites were approximately 50% and 60% of the overall volume.

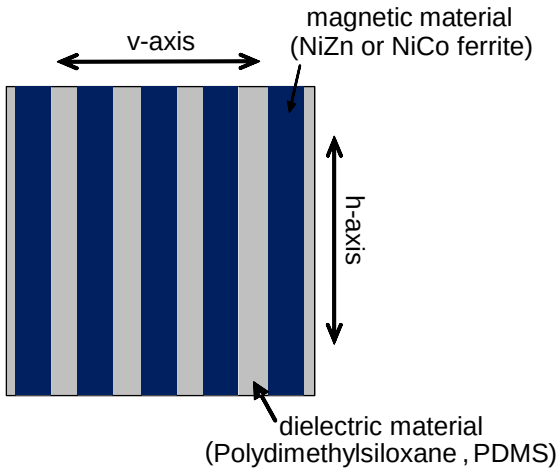

Figure 5.15: Geometry of the patterned ferrite composite.

Using the microstrip line set-up for the in-plane μ measurement [see Fig. 5.14(b)], the sample is placed over a 1.25 mm thick Acrylic holder, and then inserted under a 14 mm wide upper conductor. The separation between the upper conductor and the ground was 3 mm. The S-parameters were measured using Agilent N5230C network analyzer from 50 MHz to 4.5 GHz, and the TRL-calibration technique was employed to remove the embedded error terms. With the calibrated S_{21} data the raw permeability of NiCo and NiZn composites were calculated from the procedure in section 5.2.1. They are shown in Fig. 5.16(a) and (b). The insets to the right show the fabricated sample and direction of the applied H-field for each measurement. Overlaid with these raw permeabilities are simulated curves (dotted lines), obtained from a

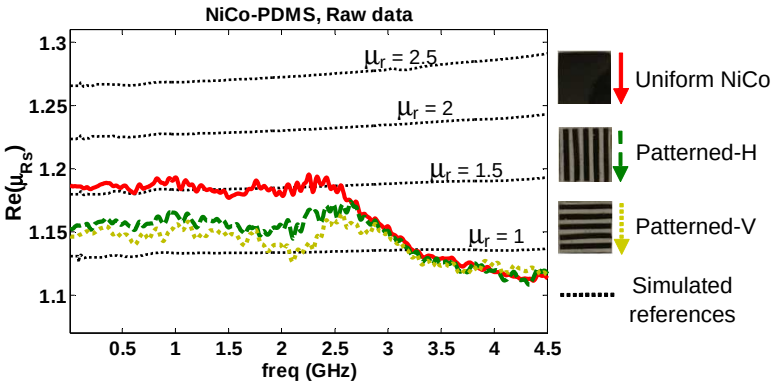

(a)

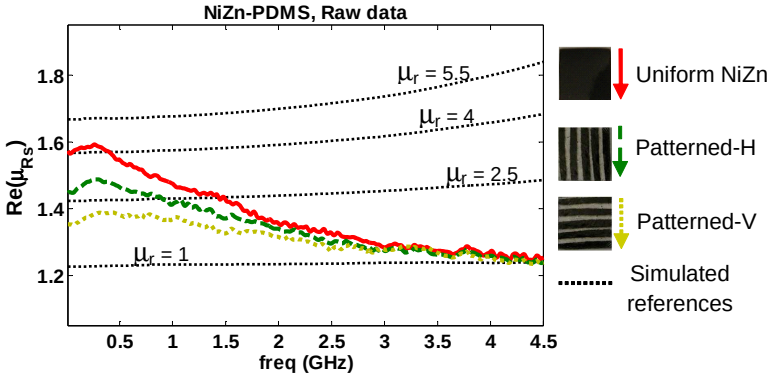

(b)

Figure 5.16: Raw permeability data of (a) NiCo composite and (b) NiZn composite.

full-wave simulation tool (Ansoft HFSS). μ_r values next to each curve denote the permeabilities of the sample assigned in the simulations. These simulated curves were used to calculate (p_1, p_2) in (5.27). The calculated (p_1, p_2) are given in Fig. 5.17(a) and (b) for the two composites. As observed, (p_1, p_2) are functions of frequency since the dispersive characteristic of the microstrip line was taken into account in the full-wave simulations. Such characteristic is not captured in the quasi-static solutions. Therefore, the proposed approach works in a much broader frequency range to characterize magnetic composites.

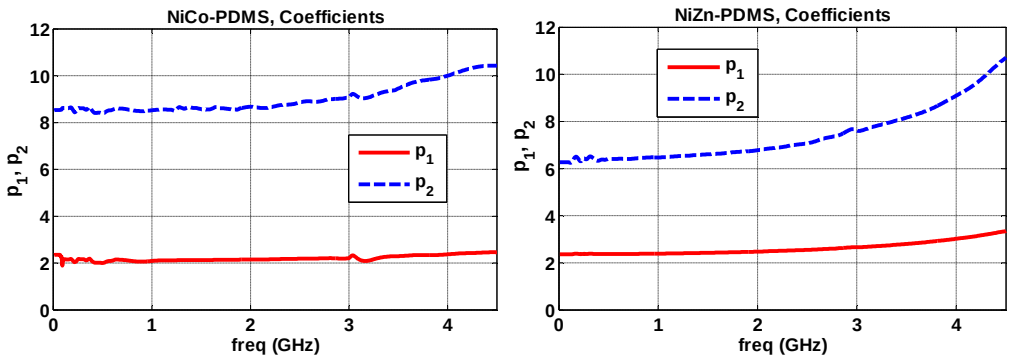

(a) (b)

Figure 5.17: p_1 and p_2 for (a) NiCo composite and (b) NiZn composite.

Having obtained (p_1, p_2), the sample permeabilities were calculated using (5.28). Fig. 5.18 depicts the de-embedded permeability (μ_{rs}) and magnetic loss-tangent ($\tan\delta_\mu$) data of the two composites. It is observed that μ_{rs} and $\tan\delta_\mu$ are both reduced due to patterning. Also, the measured results of the patterned composites exhibit the in-plane anisotropy depending on the direction of the excited H-field. It is worth noting that the loss-tangent data was also de-embedded using the same procedure as the permeability calculation. This is valid since the imaginary part of permeability also follows the same rules as the real part if macroscopic permeability of the composite is considered [82]. We also compare the results of the uniform sample measurements to the results obtained from the inductance measurement method. As can be observed in Fig. 5.18, they have good agreements up to 1 GHz.

To validate the patterned composite measurements, we compared the measured results with effective permeabilities of the composites calculated from mixing rules [82].

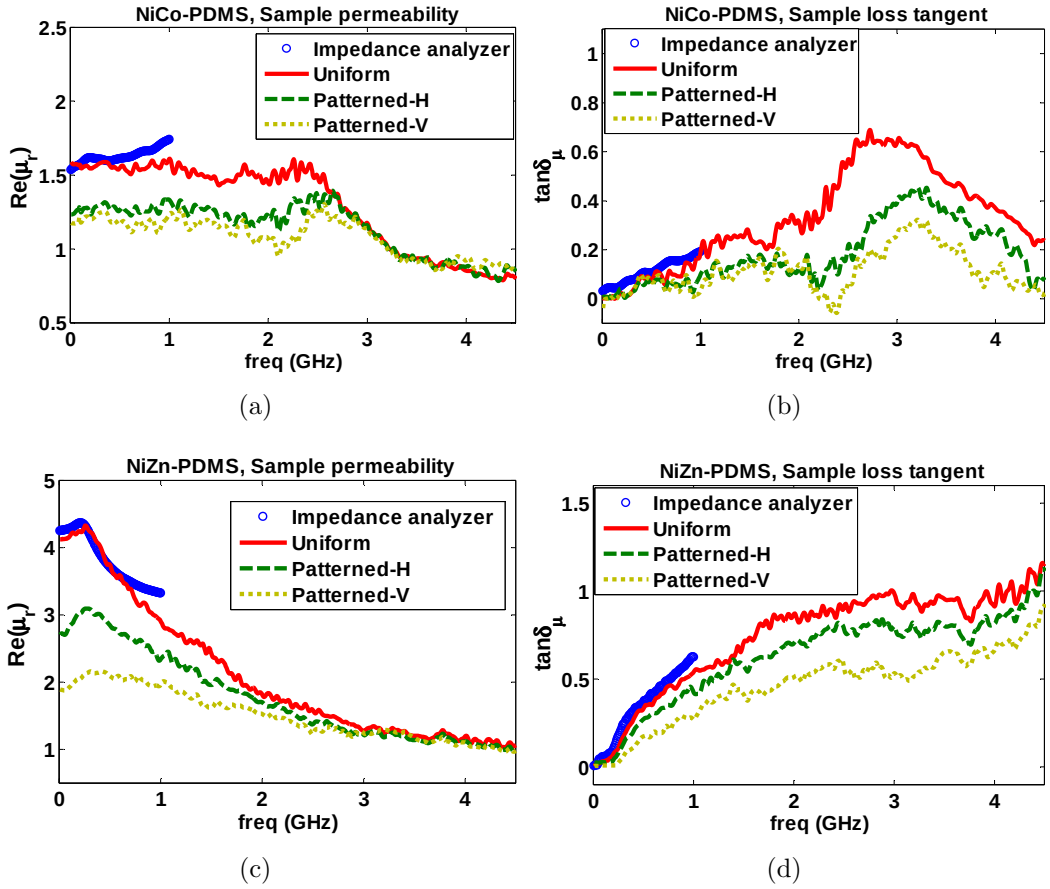

Figure 5.18: De-embedded magnetic properties of the patterned ferrite composites: (a) Re(μ_r) of the NiCo composite, (b) tanδ_μ of the NiCo composite, (c) Re(μ_r) of the NiZn composite, and (d) tanδ_μ of the NiZn composite.

Followed by the effective medium theory, the measured permeabilities with the patterned-H and -V configurations (see the insets in Fig. 5.17) should correspond to the maximum and minimum effective permeabilities of the patterned composites. They are given by

$$\mu_{eff,H} = r\mu_{ferrite} + (1-r)\,\mu_{pdms}, \tag{5.29}$$

$$\mu_{eff,V} = \frac{\mu_{ferrite}\mu_{pdms}}{r\mu_{ferrite} + (1-r)\,\mu_{pdms}}, \tag{5.30}$$

where r is the volume ratio of the ferrites. Fig. 5.19 shows $\mu_{eff,H}$ and $\mu_{eff,V}$ of the NiCo and NiZn composites with different volume ratios. $\mu_{ferrite}$ values used here are the DC permeability values of the uniform ferrite samples. As indicated by the circles in Fig. 5.19(a) and (b), the measured effective permeabilities of the patterned ferrite composites are close to the analytical ones when $r = 0.5$ and 0.6 for NiCo and NiZn composites. These r values correspond with the actual volume ratios of the ferrites in the composites.

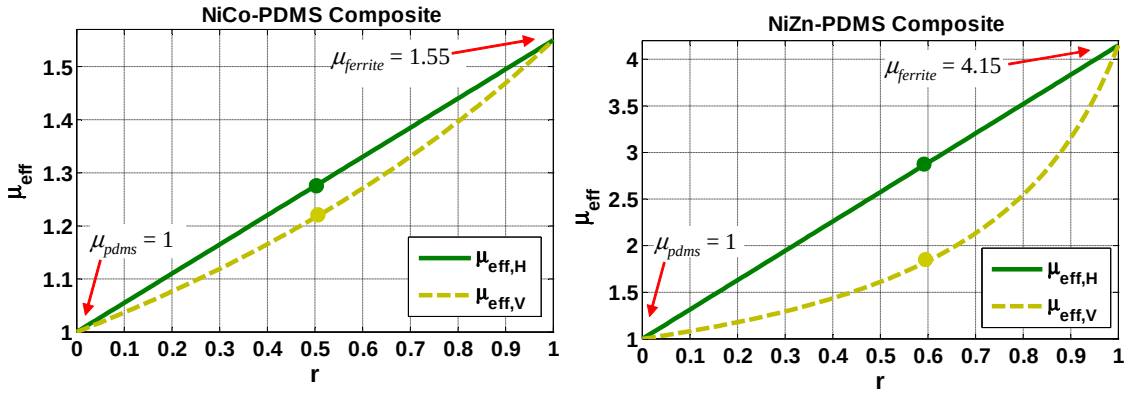

(a) (b)

Figure 5.19: The effective permeabilities calculated from (5.29) and (5.30): (a) NiCo composite and (b) NiZn composite. r is the volume ratio of the ferrite materials

5.5 Summary

This chapter presented a microstrip line material characterization method utilizing the type-II T/R configuration. In contrast to conventional de-embedding processes using quasi-static solutions, a new de-embedding process for the new microstrip line method was developed using full-wave simulations. This enable us to characterize thin

composites with small surface dimension by considering the dispersive characteristic in the test fixture. To effectively measure the sample response, the upper conductor of the microstrip line was optimized based on full-wave simulations. The measured results of patterned ferrite films showed that the proposed approach provides a much broader permeability spectrum (< 4.5 GHz) compared to a commercial inductance measurement method (< 1 GHz). Moreover, the characterization of anisotropic and non-uniform composites, not available in the inductance measurement method, could be achieved.

Chapter 6

COAXIAL PROBE METHOD FOR CONDUCTIVE FILMS

The discussions so far have emphasized broadband characterization of permittivity (ε) and permeability (μ) for low-conductive dielectric and magnetic composites. ε and μ are the properties of bound electrons inside a media. They are measures of how much the orbits of bound electrons can be stretched, thereby induce polarization, when external E- and H-fields are applied. On the other hand, highly conductive materials have an abundance of free electrons instead of bound ones. Therefore, the characterization of ε and μ hardly provides useful information for these materials. Instead, their electrical behaviors are described by conductivity (σ), which is a measure of how much free electrons are pushed by an external field, or more directly, the ability to conduct an electric current.

The such clear difference in the microscopic mechanism infers that the characterization of σ may require a completely different methodology from ε and μ characterization. In fact, however, the T/R method is still available since the interaction between the electromagnetic wave and a conductive sample can be represented by the surface impedance. Similar to the T/R methods for ε and μ characterization, once the surface impedance is captured in a certain form (e.g., S-parameters), σ of the sample can be obtained via an appropriate de-embedding algorithm. In this chapter,

we present a 1-port reflection method utilizing an open-ended coaxial probe for the characterization of σ and its inverse, resistivity (ρ), of metallic thin film composites.

6.1 Introduction

The material under interest is a transparent conductive film. It is also called "metallo-dielectric film" as its structure is formed by a periodic stack of thin metals and dielectrics (thickness of 10 to 40 nm for a layer) as illustrated in Fig. 6.1. Due to their high conductivity in the microwave range and transparency in the visible range, the transparent conductive films are considered as a promising candidate to substitute relatively heavy and opaque metals (e.g., copper, silver, gold, etc.) in applications such as EMI shielding [13], conformal antennas [85, 86], and sub-wavelength focusing [12].

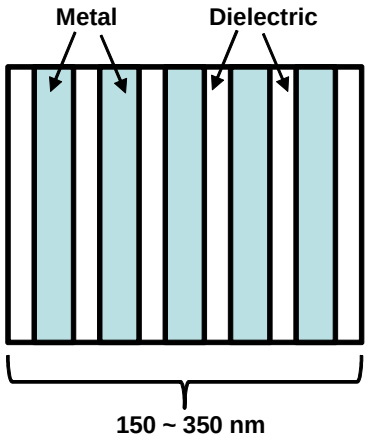

Figure 6.1: Side-view of a transparent conductive film.

To examine the validity of the transparent conductive film, its conductivity (σ) must be characterized. For a practical use, σ should be comparable to that of good

conductors (orders of 10^6 to 10^7 Siemens/meter) to carry electric currents without significant attenuation. The simplest technique to measure σ of a conductive film is the 4-point probe method [87]. With this method, σ is calculated from the surface impedance measured by separate pairs of current-carrying and voltage-sensing electrodes. However, the 4-point probe method is not available to measure RF conductivity as its source is the direct current (DC). There has been alternating current (AC) measurement methods using eddy currents instead of DC [88], but their operation is still limited to few Hz. The primary purpose of these AC methods is to avoid the requirement of a good contact between the conductor and electrodes in the 4-point probe method rather than to characterize σ at the higher frequency regime. For the RF conductivity characterization, the resonant methods are widely used [89]. While they provide highly accurate results, the resonant methods are limited to the measurements of narrow frequency ranges or discrete frequency points. Thus, they cannot be used to study the continuous frequency dependence of the sample's σ.

Analogous to the ε and μ characterizations, the T/R method can be employed to carry out broadband characterization of σ. That is, the impedance, especially the surface impedance for highly conductive materials, can be measured over a broadband, and then σ can be de-embedded from the measured impedance using a proper de-embedding process. Two-port T/R methods using waveguides have been developed to characterize transmittance and reflectance of superconducting films [90,91]. However, the bandwidth of such techniques are restricted by the operation frequency of the waveguides used. Moreover, the measurement of transmission coefficient (S_{21}) is often not feasible for highly conductive materials as their small skin depth (δ) limits the penetration of the electromagnetic waves. Specifically, most of the waves are

reflected back if a tx-line is terminated by a material with high σ as δ is inversely proportional to a square of σ and frequency (i.e., $\delta = 1/\sqrt{\pi f \sigma \mu_0}$). On the other hand, the measurement of S_{11} is sufficient for σ characterization. Since S_{11} is a complex number, it is adequate to inform the properties of the complex surface impedance, and furthermore the complex conductivity.

Herein, we employ a 1-port reflection method to characterize σ, specifically using an open-ended coaxial probe (OECP) for broadband operation (100 MHz to 15 GHz). The OECP method was first used for the permittivity characterization of dielectrics and liquids [92,93]. During the last two decades, their applications have been extended to the measurement of surface impedance of superconductors [94–96]. It is worth noting that the use of metallic probe such as the OECP is considered as an invasive characterization technique for the sample with metallic inclusions. For a conductive film, however, the OECP method is suitable as the probe is contacted to a uniform conductive surface. Also, since the penetration depth of the highly conductive film is small at the microwave frequencies, the measured result is less affected by the fringing field and radiation loss.

In the following, the theory behind the calculation of σ from the measured S_{11} is provided in details. We also describe a calibration technique for the OECP by means of short-open-load standard measurements. At the end, the measured conductivity and resistivity of optically transparent films (stack of Ag-SiO_2 or Ag-ZnS with the total thickness of 150 and 300 nm) are presented and discussed.

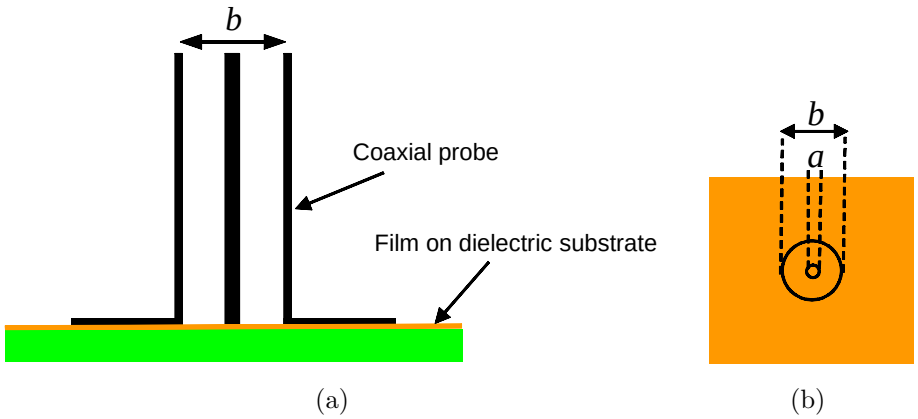

Figure 6.2: Illustration of the measurement set-up: (a) side view (b) top view of the sample surface.

6.2 Measurement Set-up and De-embedding Process

Fig. 6.2 shows a 1-port reflection measurement set-up for a thin film composite deposited on a dielectric substrate (e.g., glass). The inner and outer conductors of the OECP are contacted with the film surface. With this configuration, the measured S_{11} corresponds to the reflection of the TEM wave guided in between the inner and outer conductors [i.e., $a < r < b$ in Fig. 6.2(b)]. The main idea is to de-embed σ of the film from this S_{11}. As σ is related to the impedance, we first derive the equations for the effective impedance of the sample (film+substrate). Two different solutions for the effective impedance are provided in the following. They are based on 1) measurement (direct problem) and 2) analytical calculation (inverse problem). For the latter, we adopt the so-called "thin-film approximation" to simplify the equation. At the end, these two solutions are compared to find the closed-form expression of σ.

6.2.1 Direct Problem (Measured Solution)

The measurement set-up, as depicted in Fig. 6.2, can be considered as an electromagnetic wave transmission-reflection problem onto a multilayer structure. The simplified picture for the problem is shown in Fig. 6.3. With this set-up, the effective impedance of the film+substrate, Z_l^{eff}, is calculated by

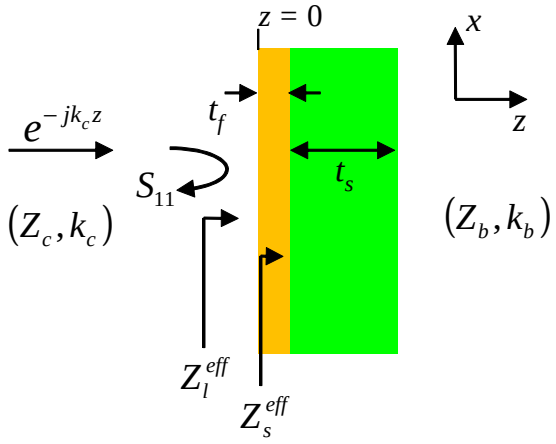

Figure 6.3: Simplified problem set-up.

$$Z_l^{eff} = Z_c \frac{1 + S_{11}}{1 - S_{11}}, \tag{6.1}$$

where Z_c is the characteristic impedance of the coaxial waveguide and S_{11} is the reflection coefficient measured at the sample surface. For a coaxial probe, Z_c is given by

$$Z_c = Z_0 G / \sqrt{\varepsilon_r}, \tag{6.2}$$

where Z_0 is 377 Ω and ε_r is the dielectric material inside the coaxial probe (e.g., Teflon or Polyethylene). G is a geometrical factor of the coaxial probe determined by

the inner (a) and outer conductor (b) diameters of the probe:

$$G = \frac{\ln(b/a)}{2\pi}. \tag{6.3}$$

G must be involved in the calculation of the impedance since the voltage and current applied on the sample are restricted by the aperture dimension of the coaxial probe. Substituting (6.2) and (6.3) into (6.1) yields

$$Z_l^{eff} = Z_0 \frac{\ln(b/a)}{2\pi\sqrt{\varepsilon_r}} \frac{1+S_{11}}{1-S_{11}}. \tag{6.4}$$

The above is the solution for the direct problem derived from the measured S_{11} and the properties of the coaxial probe. Next, we consider the solution for the indirect problem formulated by the general tx-line and surface impedance theories.

6.2.2 Inverse Problem (Analytical Solution)

The multilayer problem set-up in Fig. 6.3 is a combination of four different tx-lines with their own impedance characteristics. We are interested in formulating an analytical solution for Z_l^{eff} that represents the impedance looked toward the sample at $z = 0$. Using the general transmission line equation, the effective impedances, Z_l^{eff} and Z_s^{eff} in Fig. 6.3, are expressed by

$$Z_l^{eff} = GZ_f^{\infty} \frac{Z_s^{eff} + Z_f^{\infty}\tanh(jk_f t_f)}{Z_f^{\infty} + Z_s^{eff}\tanh(jk_f t_f)}, \tag{6.5}$$

$$Z_s^{eff} = Z_s^{\infty} \frac{Z_b + Z_s^{\infty}\tanh(jk_s t_s)}{Z_s^{\infty} + Z_b\tanh(jk_s t_s)}, \tag{6.6}$$

where Z_f^{∞} in (6.5) and Z_s^{∞} in (6.6) stand for the characteristic impedances of film and substrate materials, respectively. Contrary to "effective" impedances, these represent the impedances of "bulk" materials (thickness = ∞). Z_b in (6.6) is the impedance of the backing material as noted in Fig. 6.3. The backing material can be either air

($Z_b = \infty$) or PEC ($Z_b = 0$) depending on the measurement set-up. Also, k_f and k_s are the wave propagation constants in the film and in the substrate. Followed by the definition of impedance,

$$Z_f^{\infty} = \sqrt{\frac{\mu_0}{\varepsilon_f}} = \sqrt{\frac{\mu_0}{\varepsilon_f' - j\sigma/\omega}}, \tag{6.7}$$

where ε_f' and σ is the permittivity and conductivity of the film. We stress that ε_f' and σ are real numbers. Similarly,

$$Z_s^{\infty} = \sqrt{\frac{\mu_0}{\varepsilon_s}} = \sqrt{\frac{\mu_0}{\varepsilon_s' - j\varepsilon_s''}}. \tag{6.8}$$

In case of (6.8), we express the permittivity in real and imaginary parts instead of σ since the substrate is a low-conductive material. With the defined Z_f^{∞} and Z_s^{∞}, k_f and k_s are expressed by

$$k_f = \frac{\mu_0\omega}{Z_f^{\infty}} = \omega\sqrt{\mu_0}\sqrt{\varepsilon_f' - j\sigma/\omega}, \tag{6.9}$$

$$k_s = \frac{\mu_0\omega}{Z_s^{\infty}} = \omega\sqrt{\mu_0}\sqrt{\varepsilon_s' - j\varepsilon_s''}. \tag{6.10}$$

By plugging in (6.6)-(6.10) into (6.5), the analytical solution for Z_l^{eff} can be calculated.

6.2.3 Closed-form Expression of σ

To this end, we can solve for two unknowns (i.e., σ and ε_f') by comparing two equations for Z_l^{eff} [i.e., (6.4) and (6.5)] with the knowledge of thickness values (t_f, t_d), substrate properties (ε_s', ε_s''), coaxial probe properties (a, b, ε_r) and the measured S_{11}. An iterative solver with a good initial guess can be used to solve these two unknowns. However, there is a high possibility of non-convergence since σ and ε_f' are usually large numbers for highly conductive materials. Alternatively, the so-called

thin film approximation can be applied to carry out the closed-form expressions for σ and ε'_f. To apply the thin film approximation, the following conditions must be satisfied [97]:

$$\left|Z_s^{eff}\right| >> \left|Z_f^{\infty}\right|, \tag{6.11}$$

$$|k_f t_f| << 1. \tag{6.12}$$

If (6.11) is the case, (6.5) is simplified to

$$Z_l^{eff} \approx G Z_f^{\infty} \coth\left(jk_f t_f\right). \tag{6.13}$$

The Taylor series expansion of $\coth\left(jk_f t_f\right)$ term is given by

$$\coth\left(jk_f t_f\right) = \left(jk_f t_f\right)^{-1} + \frac{\left(jk_f t_f\right)}{3} - \frac{\left(jk_f t_f\right)^3}{45} + \frac{2\left(jk_f t_f\right)^5}{945} + \cdots . \tag{6.14}$$

The higher order terms in the above can be ignored if (6.12) is also satisfied. (6.12) implies the penetration depth is much longer than the film thickness, which is commonly accepted for very thin films at the microwave range. Dropping the high order terms in (6.14) simplifies (6.13) to

$$Z_l^{eff} \approx G Z_f^{\infty} \frac{1}{jk_f t_f}. \tag{6.15}$$

Substituting (6.7) and (6.9) into (6.15) gives

$$Z_l^{eff} \approx \frac{G}{t_f\left(\sigma + j\omega\varepsilon'_f\right)}. \tag{6.16}$$

Together with (6.4) and (6.16), σ and ε'_f are expressed in closed-forms by

$$\sigma = \frac{1}{t_f Z_0}\mathrm{Re}\left[\sqrt{\varepsilon_r}\left(\frac{1-S_{11}}{1+S_{11}}\right)\right] \ (\mathrm{S/m}), \tag{6.17}$$

$$\varepsilon'_f = \frac{1}{\omega t_f Z_0}\mathrm{Im}\left[\sqrt{\varepsilon_r}\left(\frac{1-S_{11}}{1+S_{11}}\right)\right] \ (\mathrm{F/m}). \tag{6.18}$$

That is, if the conditions for the thin film approximation are satisfied, the conductivity and permittivity of the film are simply calculated from the measured S_{11}, the given film thickness (t_f), and the given relative permittivity of the dielectric inclusion in the coaxial line (ε_r). Furthermore, the resistivity (ρ) and reactivity (X) of the film can be obtained by

$$\rho = \mathrm{Re}\left[\frac{1}{\sigma + j\omega\varepsilon'_f}\right] \ (\Omega\text{-m})\,, \tag{6.19}$$

$$X = \mathrm{Im}\left[\frac{1}{\sigma + j\omega\varepsilon'_f}\right] \ (\Omega\text{-m})\,. \tag{6.20}$$

6.3 Coaxial Probe Calibration

The accuracy of the de-embedded σ strongly depends on the error in the measured S_{11}. Without calibration, the measured S_{11} includes undesirable errors originated from cable attenuation, probe imperfection, and the most of all, the difference in reference planes. In the previous chapters, we associated with the 2-port TRL-calibration for various T/R techniques. For the coaxial probe method, however, only 1-port calibration is necessary. The general error model for a 1-port reflection measurement is illustrated in Fig. 6.4. S_{11}^a and S_{11}^m in the figure are the actual (i.e., desirable) and measured reflection coefficients, respectively. Also, the three error terms refer to as

- E_D (Directivity): Signal reaches the detector directly without interacting with the sample.

- E_S (Source mismatch): Signal coming from the sample is reflected back to the sample and this reflected signal is added up to the signal going to the sample.

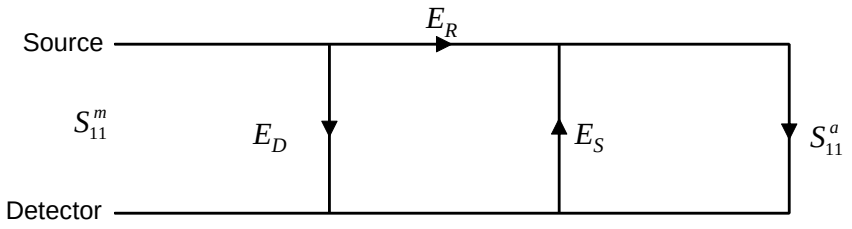

Figure 6.4: Error model for the 1-port reflection measurement set-up.

- E_R (Reflection tracking): Attenuation and phase shift in the transmission line.

Due to these three error terms S_{11}^m is altered from S_{11}^a. More specifically, from the signal flow graph analysis of Fig. 3, S_{11}^m is expressed by [49, 98]

$$S_{11}^m = E_D \frac{E_R S_{11}^a}{1 - E_S S_{11}^a} \tag{6.21}$$

To calibrate out the error terms, measurements of three known calibration standards are needed (e.g., short-open-load). With these measured S_{11} of the calibration standards, the three error terms are determined by [96]

$$E_D = \frac{M_1 (M_2 - M_3) A_2 A_3 + M_2 (M_3 - M_1) A_3 A_1 + M_3 (M_1 - M_2) A_1 A_2}{(M_1 - M_2) A_1 A_2 + (M_2 - M_3) A_2 A_3 + (M_3 - M_1) A_3 A_1}, \tag{6.22}$$

$$E_R = \frac{(M_1 - M_2)(M_2 - M_3)(M_3 - M_1)(A_1 - A_2)(A_2 - A_3)(A_3 - A_1)}{\left[(M_1 - M_2) A_1 A_2 + (M_2 - M_3) A_2 A_3 + (M_3 - M_1) A_3 A_1\right]^2}, \tag{6.23}$$

$$E_S = \frac{M_1 (A_2 - A_3) + M_2 (A_3 - A_1) + M_3 (A_1 - A_2)}{(M_1 - M_2) A_1 A_2 + (M_2 - M_3) A_2 A_3 + (M_3 - M_1) A_3 A_1}, \tag{6.24}$$

where M_i and A_i are measured and analytical S_{11} values of the three standards for open ($i = 1$), load ($i = 2$), and short ($i = 3$). Obviously, the ideal values for A_1, A_2, and A_3 are 1, 0, and -1. However, for the calibration over a wide bandwidth, A_i values are not constant (versus frequencies) since the higher order modes affect the propagating wave. Although we can assume only the fundamental TEM mode

is propagating inside the coaxial line, the higher order modes are excited at the coaxial probe aperture and must be considered for accurate A_i calculation for wide-band calibration. Another difficulty in conventional 1-port calibration methods is the fabrication of a matched load that provides $M_2 \approx 0$. There has been a report [95] using lossy NiCr films emulating a long lossy transmission line to achieve $M_2 < -30dB$. However, it is also reported that the calibrated results still included unwanted peaks and small oscillations above 8 GHz.

With these issues in mind, we proceeded to use the analytical formulae in Bakhtiari et al. [99] to calculate accurate A_i values. The paper provides solutions of the reflection coefficients considering the higher order modes radiated from the OECP into stratified dielectrics. The equations of A_i for open, short, and load standards are given in Appendix C. Moreover, the capability to calculate A_i with high precision enables us to use an ordinary low-loss dielectric slab as the load-standard. That is, instead of trying to acquire an accurate M_2 value, we calculate the accurate A_2 value based on the known properties of the load-standard.

After solving for the three error terms from (6.22)-(6.24) using this new calibration procedure, the calibrated S_{11} (S_{11}^c) of the sample is obtained by inverting (6.21) as

$$S_{11}^c = \frac{S_{11}^m - E_D}{E_R + E_S\,(S_{11}^m - E_D)}. \tag{6.25}$$

This S_{11}^c must be used in (6.17)-(6.20) to de-embed correct properties of the sample.

6.4 Measurement Demonstration

Two different transparent conductive films were tested using the proposed technique. They are compositions of Ag-SiO_2 and Ag-ZnS. The thicknesses of the films were 150 nm and 300 nm, respectively, and they were deposited on a 1 mm thick

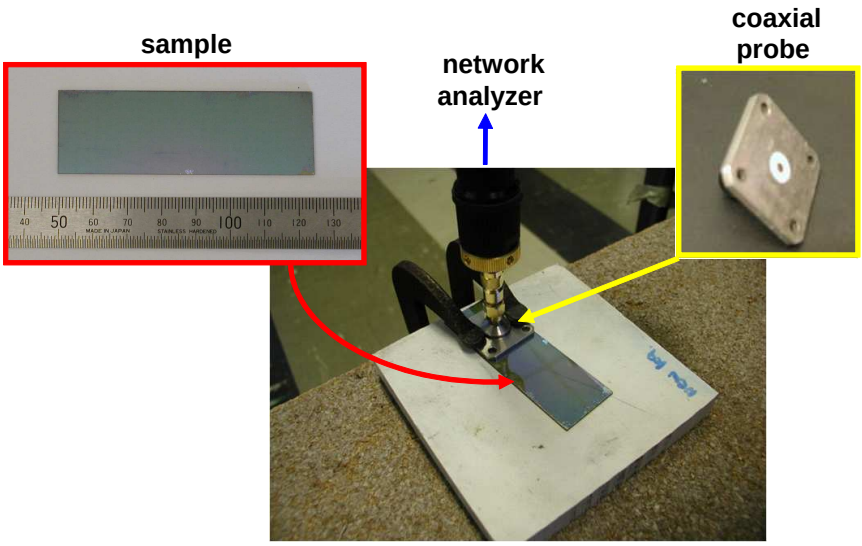

Figure 6.5: Picture of the measurement set-up.

glass substrate. An OECP whose diameters are equivalent to RG-12 A/U coaxial cable standard (a = 1.13 mm, b = 3.63 mm) was used for the measurements. A picture of the measurement set-up is given in Fig. 6.5. The sample was clamped to the rectangular flange of the OECP. The S_{11} response were collected by Agilent N5452A network analyzer in the range of 100 MHz to 15 GHz. Noting that the measurements of calibration standards were realized by leaving the OECP in the air (open), clamping it on a copper block (short) and on a 1 inch thick dielectric slab of $\varepsilon_r = 4(1 - j0.001)$ (load).

We first checked the effectiveness of the calibration. Fig. 6.6 shows the measured and analytical S_{11} magnitude data of the calibration standards. The three error terms (E_D, E_S, and E_R in Chapter 6.3) were calculated by comparing the differences in Fig. 6.6(a) and (b). These systematical error terms were used to calibrate the sample measurement data as described in (6.25). Fig. 6.7(a) and (b) compare the

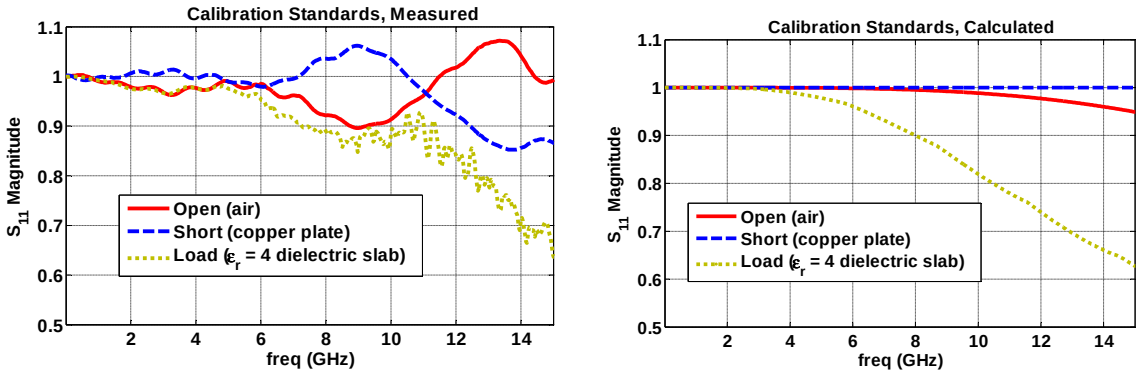

(a) (b)

Figure 6.6: S_{11} magnitudes of the calibration standards: (a) measured data and (b) analytical data.

S_{11} magnitude and phase of the Ag-SiO_2 film before and after the calibration. Non-calibrated data is labeled as "raw" in the figures. As can be seen in Fig. 6.7(a), the magnitude variations presented in the raw data are removed after calibration. Consequently, the magnitude of the calibrated data become close to 1, implying most of the wave impinged on the sample was reflected back. For the phase data [see Fig. 6.7(b)], the multiple wrappings in the raw data correspond to the electrical delay in the coaxial cable and probe. These are eliminated after calibration, implying the measurement reference plane is moved to the aperture of the coaxial probe. The S_{11} of the Ag-ZnS showed similar results.

With the calibrated S_{11}, we first checked the validity of the thin film approximation using the measured data. Fig. 6.8(a) and (b) correspond to the validity of the condition (6.11) and (6.12). As can be seen, both conditions were satisfied for our sample measurements in the frequency range of interest (100 MHz to 15 GHz), i.e., $\left|Z_s^{eff}\right| / \left|Z_f^{\infty}\right| >> 1$ and $|k_f t_f| << 1$. Specifically, the lowest value in Fig. 6.8(a) is

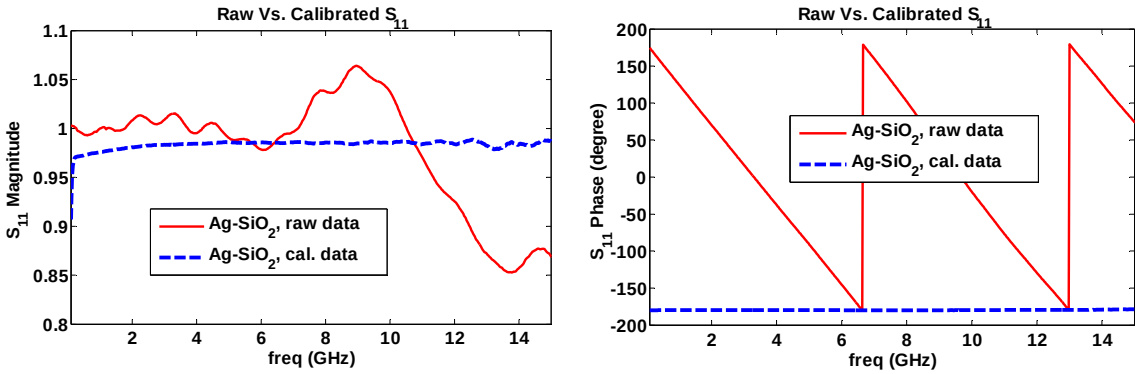

(a) (b)

Figure 6.7: Measured and calibrated S_{11} responses of the Ag-SiO_2 composite: (a) magnitude and (b) phase.

360.7 and the highest value in Fig. 6.8(b) is only 0.07. The skin depth (δ) was also calculated from the measured data and illustrated in Fig. 6.9. δ of both films are high at low frequencies and significantly reduces as the frequency increases followed by $1/\sqrt{f}$ dependence in its equation (i.e., $\delta = 1/\sqrt{\pi f \sigma \mu_0}$). It is also shown that δ is much larger than the thickness of the film even at the lowest frequency (40 μm versus 150 nm), which is another proof for the validity of condition (6.12).

Followed by confirming the validity of conditions for the thin film approximation, we proceeded to de-embed the film's σ and ρ using the closed-form equations described in Chapter 6.2.3. Fig. 6.10 shows the de-embedded σ and ρ. The obvious difference in σ values for the Ag-SiO_2 and Ag-ZnS films originated from their difference in structural properties such as the layer thickness and permittivities of dielectric layers. The Ag-ZnS film has higher conductivity than the Ag-SiO_2 below 4 GHz. Above 4 GHz, however, the Ag-SiO_2 film exhibits higher and more stable conductivity performance. The ρ values depicted in Fig. 6.10(b) show opposite trends

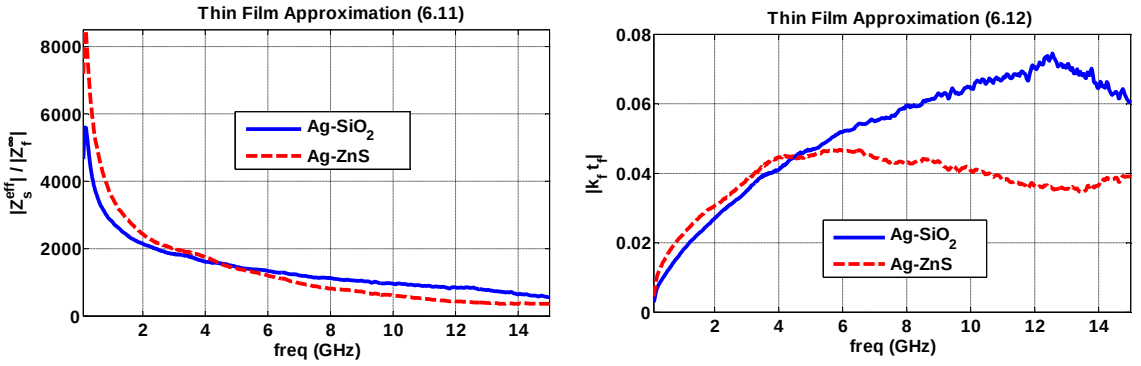

(a) (b)

Figure 6.8: Validity of the thin film approximation: (a) condition (6.11) and (b) condition (6.12).

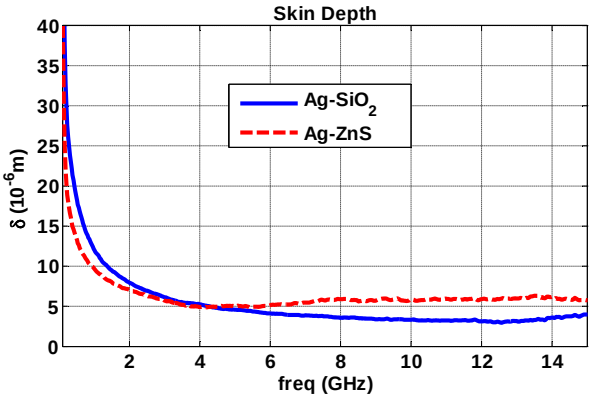

Figure 6.9: Skin depth values obtained from the measured data.

to the σ. This is expected since ρ is inversely proportional to σ as in (6.19). However, ρ of the films are not exactly the inverse of σ, since ε'_f is involved in the equation. It is worth noting that the characterized films' σ and ρ values are in the order of 10^6 and 10^{-6}, which is much lower and higher than those of good conductors (e.g., σ and ρ of

copper are 5.8×10^7 and 1.7×10^{-8}). They are close to Manganin ($\sigma = 2.07 \times 10^6$) and Mercury ($\sigma = 1.02 \times 10^6$).

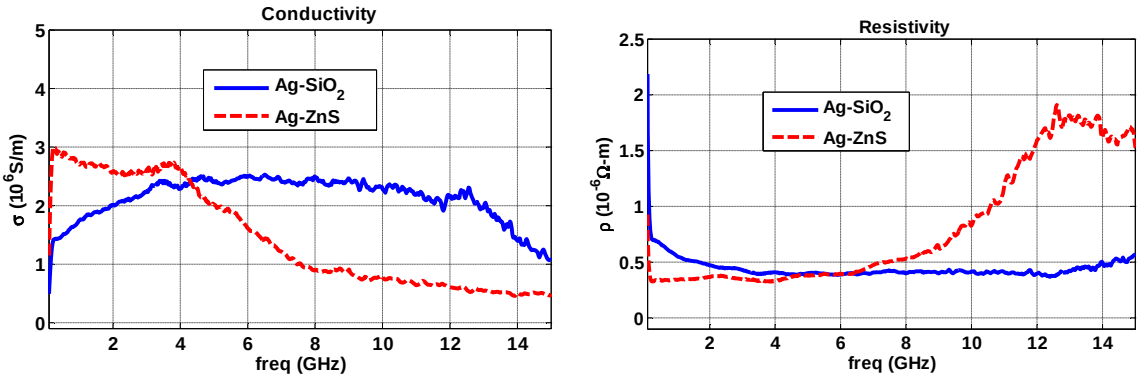

(a) (b)

Figure 6.10: De-embedded (a) conductivity and (b) resistivity of Ag-SiO_2 and Ag-ZnS composites.

6.5 Summary

In this chapter, an open-ended coaxial probe was employed for the characterization of conductivity (σ) and resistivity (ρ) of conductive films. We developed a de-embedding algorithm to retrieve σ and ρ from the S_{11} response measured upon the films. Using the thin film approximation applicable to highly conductive and thin materials, closed-form solutions for σ and ρ could be obtained and used as the primary equations in the de-embedding process. Furthermore, a calibration technique that considers the higher order mode effects was developed to effectively remove undesirable error terms in the S_{11} measurements. Together with the proposed OECP

measurement set-up, de-embedding and calibration techniques, the σ and ρ of transparent films could be characterized over a frequency range of 150:1 (100 MHz to 15 GHz).

Chapter 7

CONCLUSIONS AND FUTURE WORK

7.1 Summary and Conclusions

Broadband material characterization is indispensable for the research of emerging microwave technologies, particular in the design of novel engineered composites. To carry out appropriate design rules, the electromagnetic wave behaviors in the engineered composites must be quantified using an accurate characterization technique. Depending on the requirements of characterization, a best method for a specific composite might be simply not good enough for the others. In this context, we have developed four unique characterization methods suitable for different engineered composites. The reasonings for the development of these methods were clearly identified in the beginning of each chapter. Subsequently, theoretical backgrounds, simulated studies and experimental results were presented in details to pursue the completeness of this dissertation.

Specifically, Chapter 2 provided considerations in engineered composite characterization from a general viewpoint. We also reviewed fundamentals of three most widely

used techniques: the capacitance/inductance (C/L), resonant cavity, and transmission/reflection (T/R) methods. Based on this, we have learned the T/R method is the most effective technique for broadband and non-invasive characterization.

In Chapter 3, the synthetic Gaussian beam method was developed to non-invasively characterize a multi-layered metamaterial slab at 8-12 GHz. This method synthetically generates a Gaussian beam spotted on a material sample. The principle mean of this is to overcome drawbacks in using dielectric lenses in conventional free-space measurement systems. The criteria to reconstruct a valid Gaussian beam were discussed based on numerical examples. The experimental results from a known dielectric slab and a degenerate band edge slab measurements were also provided with good agreements to the calculated data.

Recognizing that the synthetic Gaussian beam method is not available at the lower frequencies (< 5 GHz), in Chapter 4, a tapered stripline method was developed. With this method, the broadband characteristic (100 MHz to 4.8 GHz) of material's ε and μ could be simultaneously characterized by measuring S-parameters. A uniform ferrite-resin composite was characterized with good agreements to the data from conventional impedance analyzer measurements. We pointed out that the operation frequency range of the tapered stripline is much broader than the impedance analyzer (< 1 GHz). However, studies based on full-wave simulations showed the error in the tapered stripline method exponentially increases if the sample is thinner than 1 mm. With this issue in mind, in Chapter 5, we developed a microstrip line based fixture to characterize thin and small film composites.

The microstrip line method presented in Chapter 5 was able to effectively illuminate the surface of thin samples with E- and H- fields, therefore, in-plane permittivity

and permeability could be captured in the measured S-parameters. However, it required a secondary de-embedding process to remove the effects originated from the illumination of the surroundings such as the substrate or sample holder. For this, we developed a de-embedding algorithm based on curve-fitting a set of full-wave simulation data. Compared to the previously reported quasi-static de-embedding algorithms, the new one was capable of de-embedding the film's properties considering the dispersive characteristics of the microstrip line. Using this method, patterned ferrite films with in-plane anisotropy were characterized up to 4.5 GHz.

Chapter 6 tackled on the characterization of conductivity instead of permittivity and permeability as in the previous sections. A 1-port reflection measurement set-up was implemented with an open-ended coaxial probe and a de-embedding process to retrieve the conductivity was developed based on surface impedance calculation and thin film approximations. We also developed a new 1-port calibration technique that considers the higher order mode excitation at the coaxial aperture. Using the proposed method, transparent conductive films deposited on a glass substrate were characterized in the frequency range of 100 MHz to 15 GHz.

7.2 Future Work

For broadband material characterization, the use of T/R methods is strongly considered since no other technique has been so far provided a capability to operate in more than 3: 1 to 10: 1 bandwidth at microwave frequencies. Such *sine qua non* led us to develop several improved T/R techniques as presented in this text. Some future research topics for further improvements may include the following.

7.2.1 Multi-line TRL for Improved Error Calibration

Compared to narrowband resonant methods whose error in de-embedded parameters is less than 1%, broadband T/R methods typically have more than 3% error or even 10% for loss characterization. It is important to note that such error values are not consistant along the measurement frequency range. For example, the tapered stipline method in Chapter 4 often showed higher error value ($> 3\%$) at the low-end and at multiple frequency spots while the other frequencies show relatively good error performance ($< 2\%$).

One way to improve this error behavior can be the use of advanced calibration techniques. The TRL-calibration method frequently used in this text, although powerful for non-coaxial line structures, has a limitation in accuracy for broadband measurements. As the main idea of the TRL-calibration is to utilize the phase difference between thru- and line-standards, their physical length should be chosen properly to obtain the best calibration result. Specifically, the optimum phase difference between the two is 90° (quarter-wavelength). However, a line length providing 90° phase difference at a certain frequency does not provide the same phase difference at other frequencies. It is, therefore, often recommended to employ a line-standard having at least 20° to 160° phase difference from the thru for reasonably accurate calibration over bandwidth of interest. This criteria may degrade the sensitivity in the T/R method since the error of using a line-standard with 20° (or 160°) difference exhibits 2.92 times more error than the optimal length, 90° [100].

The above-mentioned accuracy problem can be resolved using multiline TRL-calibration technique implemented by National Institute of Standard and Technology

(NIST) [100]. This technique reduces the error by employing not only multiple line-standards but also a search algorithm to estimate the optimum line pair.

The principle of multiline TRL can be understood from the following example. Let us first consider the phase difference in 2-18 GHz when the length difference between a thru- and a line-standard is 0.625 cm (Line1) as depicted in Fig. 7.1(a). With such wide bandwidth, it is unavoidable to have a phase difference less than 20° at the lower end, which violates the $20° - 160°$ phase difference rule recommended for the original TRL. Noting that the most accurate calibration data is expected at 12 GHz whose phase difference is 90°. A similar interpretation can be given for Fig. 7.1(b). The length difference in this case is 1.875 cm (Line2). Particularly at 8 and 16 GHz, the phase difference is zero, therefore large uncertainty will be resulted in the calibrated data. Next, we may consider setting Line1 as the thru-standard and check the phase difference to Line2. This is effectively the same as having a zero-length thru and 1.875-0.625 = 1.25 cm line-standard. The phase difference for this case is shown in Fig. 7.1(c). The way to fully utilize these three line-pairs is described in Fig. 7.1(d). Using a search algorithm (e.g., least-squares estimator), the optimum line pairs (closest to 90°) are assigned at each frequency point as depicted with the black-dotted line. As can be observed, the phase difference is always larger than 45° in the entire frequency band, thus more accurate calibration data can be obtained. The improvement described here also implies that adding more line-standards may result more accurate data over a broader frequency range. Thus, the use of multiline TRL is promising to improve error performance in T/R methods such as the tapered stripline and microstrip line methods presented in Chapter 3 and 4.

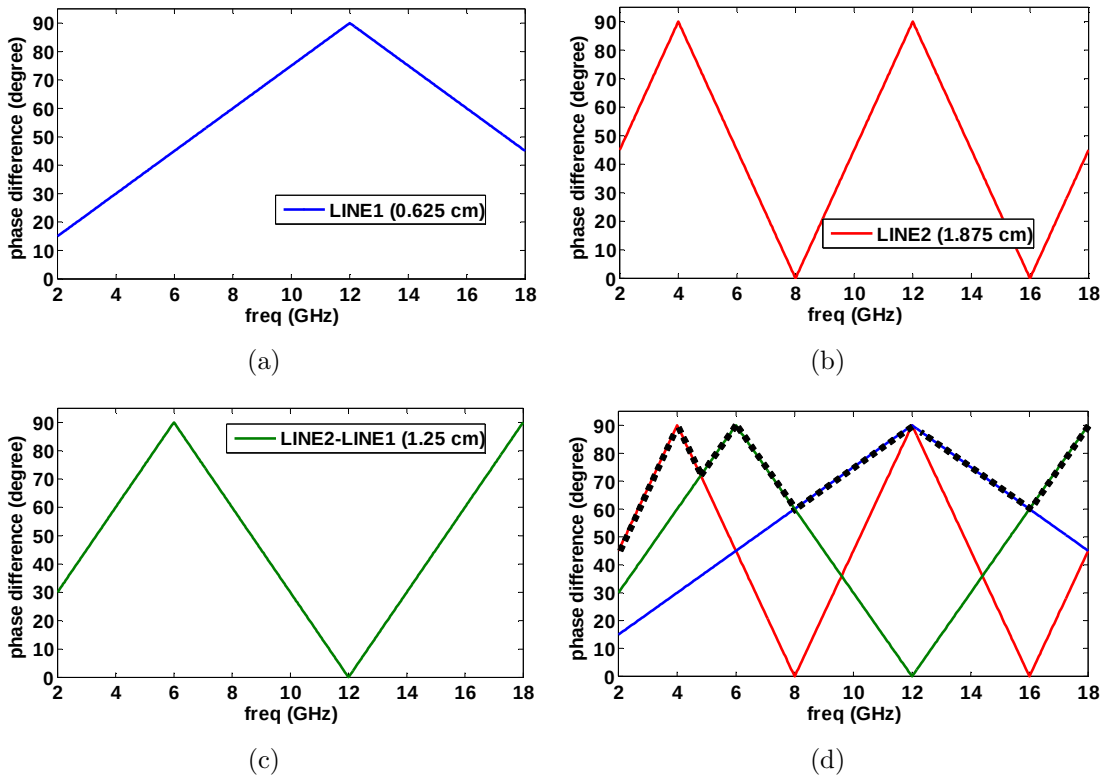

Figure 7.1: Demonstration of the multiline TRL calibration procedure. The phase difference between a thru- to line-standard for (a) Line1, (b) Line2, (c) Line2−Line1, and (d) after multiline TRL process.

7.2.2 Characterization of Anisotropic Tensors

There is a great interest in characterizing the off-diagonal elements in ε and μ tensor matrices [101–104]. For example, ferroelectric and ferromagnetic materials contain off-diagonal terms in their constitutive relations due to crystalline misalignments. This implies the transmitted and reflected responses on such materials can result in elliptically polarized field and in some cases result in non-reciprocal properties.

The microstrip line method in Chapter 4 is capable to characterize materials with biaxial-anisotropy. That is, the diagonal elements in ε or μ tensor matrix can be characterized by rotating a sample by 90°. Accordingly, it seems possible to retrieve the values of other elements, including off-diagonal terms, from the sample responses measured with more angular diversity. Previously, Hashimoto et al. [104] measured the off-diagonal permittivity of rubber sheets using a bi-static free-space measurement set-up. In this method, $\bar{\bar{\varepsilon}}$ elements were de-embedded from measured reflection coefficients with various sample orientations. For example, 4 unknowns in the $\bar{\bar{\varepsilon}}$ matrix can be retrieved from 6 S-parameter measurements with different angles. However, with such free-space measurement method, a very large sample (30 cm) was required for the characterization at X-band to avoid diffraction at sample's edges. Moreover, a large distance between the transmitter (parabolic antenna) and sample was required (13.95 m) to achieve far-field illumination.

To reduce the system size, a circular waveguide blocked by a rotatable shorting plate can be used (see Fig. 7.2). Similar to the free-space bi-static set-up, the coaxial feeds excite the dominant guiding mode (TE_{11}) with two orthogonal polarization and capable of receiving both TE and TM reflection coefficients. The sample orientations are varied by rotating the end short where the holder and sample are attached. The de-embedding algorithm can be implemented by comparing the measured reflection coefficients (direct problem) to analytical ones (indirect problem) in an iterative solver. The analytical reflection coefficients can be obtained by applying three boundary conditions [see Fig. 7.2(b)] on four coupled first-order differential equations [105, 106].

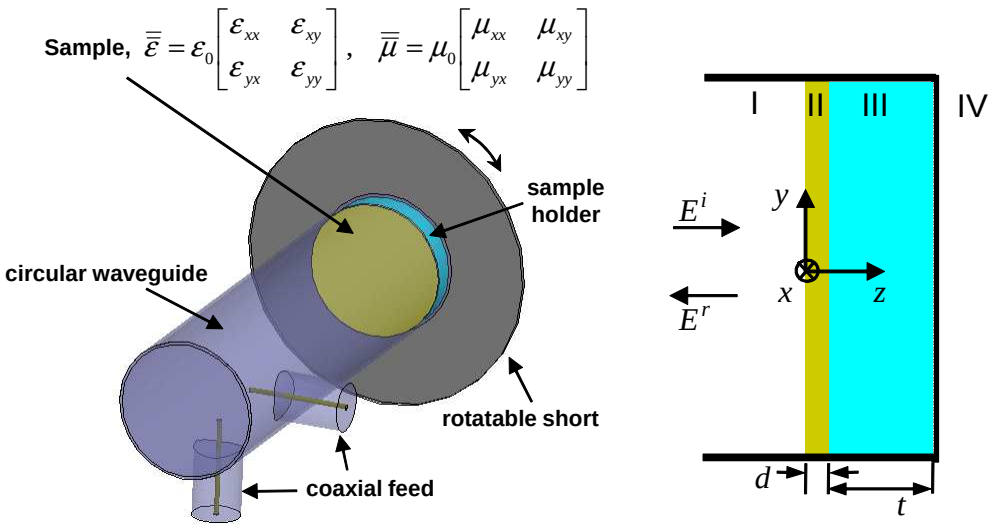

Figure 7.2: Circular waveguide backed by the rotatable short: (a) Geometry and (b) Side-view for analytical problem.

Appendix A

RADIATION FIELD FROM A GAUSSIAN DISTRIBUTED HERTZIAN DIPOLE ARRAY

For the parametric study of Gaussian beam reconstruction in Chapter 3, we have implemented a simulation code to observe the radiated E-field from a virtual (scanned) aperture. A planar array of weighted Hertzian dipoles was used to emulate the virtual aperture in this problem as depicted in Fig. A.1. In the following, the E-field at an arbitrary point, (x, y, z), from a Hertzian dipole located at (x', y', z') is derived using Huygen's principle: The field at any point external to the surface is the sum or superposition of the radiations from all the elemental radiators.

In the problem set-up, we assume all dipoles are x-polarized. The E-field of the Gaussian weighted Hertzian dipole is given by [58, 107]

$$\mathbf{E}\left(\mathbf{r}'\right) = E_0 \left(-\hat{x} + \frac{x'}{z' + jz_0}\right) U\left(\mathbf{r}'\right), \tag{A.1}$$

where E_0 is the magnitude of the E-field and $U\left(\mathbf{r}'\right)$ is the Gaussian complex amplitude at (x', y', z'), which is given in (3.1). z_0, the depth of focus of the Gaussian beam, is also given in (3.1). From this E-field expression, the H-field of the weighted Hertzian dipole is obtained from the Maxwell's equation as

$$\mathbf{H}\left(\mathbf{r}'\right) = \frac{1}{j\omega\mu_0} \nabla \times \mathbf{E}(\mathbf{r}'), \tag{A.2}$$

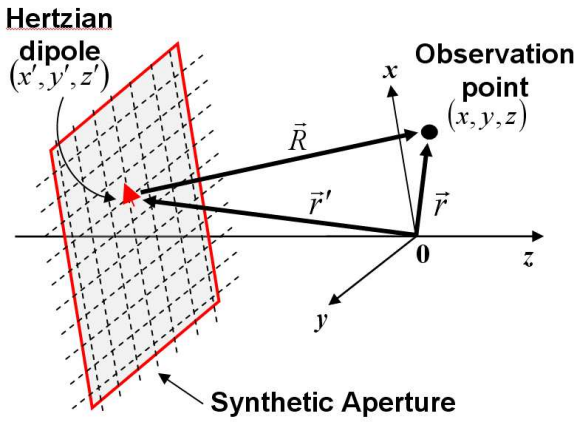

(a)

Figure A.1: Geometry of the problem.

where ω and μ_0 refer to the angular frequency and permeability in the free-space. Followed by the surface equivalence theorem [107], the E- and H-fields at the aperture can be replaced by equivalent electric and magnetic currents:

$$\mathbf{J}_s(\mathbf{r}') = \hat{z} \times \mathbf{H}(\mathbf{r}'), \tag{A.3}$$

$$\mathbf{M}_s(\mathbf{r}') = -\hat{z} \times \mathbf{E}(\mathbf{r}'). \tag{A.4}$$

Using these currents, the E-field radiated from each current source can be calculated using the free-space Green's function. The E-fields at an observation point $\mathbf{r} = (x, y, z)$ due to $\mathbf{J}_s$ and $\mathbf{M}_s$ at $\mathbf{r}' = (x', y', z')$ are calculated by

$$d\mathbf{E}^J(\mathbf{r}) = \bar{\bar{G}}_{ee} \cdot \mathbf{J}_s(\mathbf{r}'), \tag{A.5}$$

$$d\mathbf{E}^M(\mathbf{r}) = \bar{\bar{G}}_{em} \cdot \mathbf{M}_s(\mathbf{r}'), \tag{A.6}$$

where

$$\bar{\bar{G}}_{ee} = -\frac{jkZ_0}{4\pi}\left[\bar{\bar{I}}\left(1-\frac{j}{kR}-\frac{j}{(kR)^2}\right)-\hat{R}\hat{R}\left(1-\frac{j3}{kR}-\frac{3}{(kR)^2}\right)\right]\frac{e^{-jkR}}{R}, \tag{A.7}$$

$$\bar{\bar{G}}_{em} = \frac{jk}{4\pi}\left(\widehat{R}\times\bar{\bar{I}}\right)\left(1-\frac{j}{kR}\right)\frac{e^{-jkR}}{R}. \tag{A.8}$$

$\bar{\bar{G}}_{ee}$ and $\bar{\bar{G}}_{em}$ are the Green's function that relates the E-field and electrical current and the E-field and magnetic current. k in the above is the free-space wave number and Z_0 is the free-space impedance. After several but straightforward algebraic steps, (A.5) and (A.6) are expressed by

$$d\mathbf{E}^J(\mathbf{r}') = \frac{1}{4\pi}\left(\hat{x}dE_x^J+\hat{y}dE_y^J+\hat{z}dE_z^J\right)U(\mathbf{r}')\frac{e^{-jkR}}{R}, \tag{A.9}$$

$$d\mathbf{E}^M(\mathbf{r}') = \frac{jkE_0}{4\pi}\left(\hat{x}dE_x^M+\hat{y}dE_y^M+\hat{z}dE_z^M\right)U(\mathbf{r}')\frac{e^{-jkR}}{R}, \tag{A.10}$$

where the scalar values are

$$dE_x^J = \left(\frac{\partial E_z}{\partial x'}-\frac{\partial E_x}{\partial z'}\right)X_1+\frac{R_x}{R^2}\left(R_x\frac{\partial E_z}{\partial x'}+R_y\frac{\partial E_z}{\partial y'}-R_x\frac{\partial E_x}{\partial z'}\right)X_2, \tag{A.11}$$

$$dE_y^J = \frac{\partial E_z}{\partial y'}X_1+\frac{R_y}{R^2}\left(R_x\frac{\partial E_z}{\partial x'}+R_y\frac{\partial E_z}{\partial y'}-R_x\frac{\partial E_x}{\partial z'}\right)X_2, \tag{A.12}$$

$$dE_z^J = \frac{R_z}{R^2}\left(R_x\frac{\partial E_z}{\partial x'}+R_y\frac{\partial E_z}{\partial y'}-R_x\frac{\partial E_x}{\partial z'}\right)X_2, \tag{A.13}$$

$$dE_x^M = -\frac{R_z}{R}X_3, \tag{A.14}$$

$$dE_y^M = 0, \tag{A.15}$$

$$dE_z^M = \frac{R_x}{R}X_3, \tag{A.16}$$

also with

$$X_1 = 1-\frac{j}{kR}-\frac{1}{kR^2}, \tag{A.17}$$

$$X_2 = 1-\frac{j3}{kR}-\frac{3}{kR^2}, \tag{A.18}$$

$$X_3 = 1-\frac{j}{kR}. \tag{A.19}$$

Using (A.9) and (A.10), the partial E-field at each point on the planar aperture can be obtained. The addition of these E-fields gives the total E-field observed at (x, y, z). Indeed, the simulated results in Fig. 3.4 are the total fields with different parameters.

Appendix B

THRU-REFLECT-LINE CALIBRATION

The measured S-parameters must be calibrated account for the imperfections in the network analyzer itself as well as in the external RF components such as connectors, cables, etc. For the measurement of non-coaxial structures, the TRL-calibration is mainly used due to the correction capability in the absence of a matching load. Here, we derive the equations for the TRL-calibration to implement an in-house calibration computer code. The derivation given in the following is based on [49, 70, 108]. We tried to include every detail in order that anyone can implement his or her own code by following this appendix.

The block diagram of a two port network with a sample under test (MUT) in the middle is described in Fig. B.1. As can be observed, the calibrated S-parameters of the MUT can be obtained by adjusting the measured S-parameters with the knowledge of the S-parameters of the error boxes. It must be noted that there are two different matrix conventions. The $[S]$ matrix consists of S-parameters, otherwise the $[R]$ matrix refers to the wave cascading matrix which is used for the convenience in calculating matrix multiplications. The relationship between $[R]$ and $[S]$ is given by

$$[R] = \frac{1}{s_{21}} \begin{bmatrix} -\Delta & s_{11} \\ -s_{22} & 1 \end{bmatrix},$$

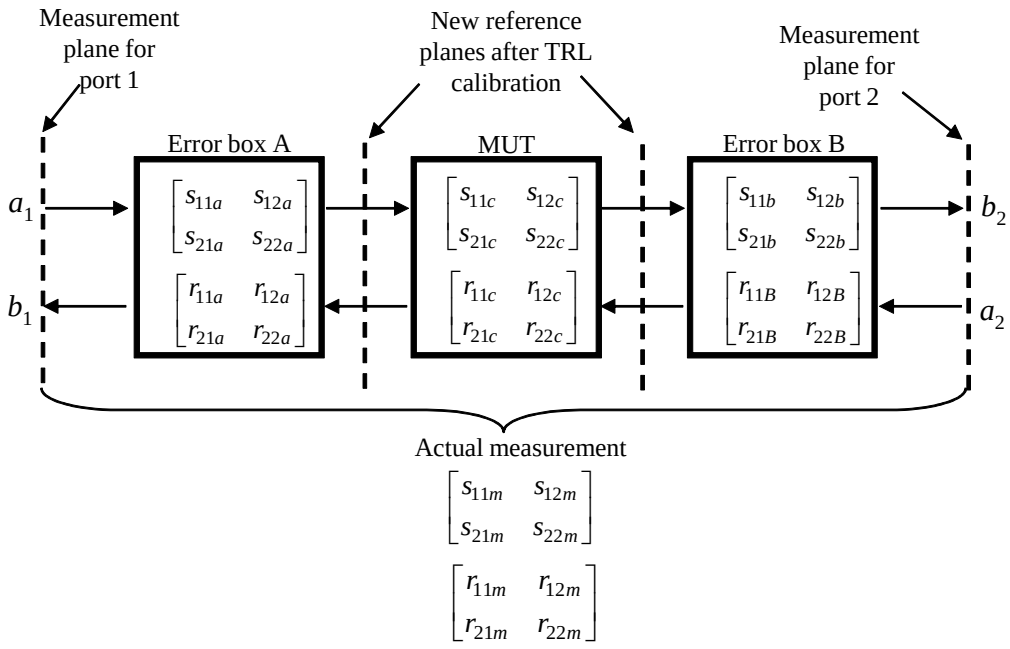

Figure B.1: Simplified problem set-up

where $\Delta = s_{11}s_{22} - s_{12}s_{21}$.

From Fig. B.1, the calibrated response is expressed by

$$\begin{bmatrix} r_{11}^c & r_{12}^c \\ r_{21}^c & r_{22}^c \end{bmatrix} = \begin{bmatrix} r_{11a} & r_{12a} \\ r_{21a} & r_{22a} \end{bmatrix}^{-1} \begin{bmatrix} r_{11}^m & r_{12}^m \\ r_{21}^m & r_{22}^m \end{bmatrix} \begin{bmatrix} r_{11b} & r_{12b} \\ r_{21b} & r_{22b} \end{bmatrix}. \tag{B.1}$$

The goal is to solve for the error terms, denoted with subscript "a" and "b" in (B.1), to calibrate out their effects from the measured response. In the TRL-calibration, measurements of three different standards are used for this process. The three standards are thru, reflect, line. Block diagrams of their measurement set-ups are depicted in Fig. B.2 to B.4. Herein, we use a zero-length thru-standard. That is, the thru-standard is realized by directly attaching the two ports. Also, we assume the reflection

coefficients at the reflect-standard (Γ_R) are same for the waves coming from both directions. Note that this does not mean the measured reflection coefficients read at port-1 and -2 are the same.

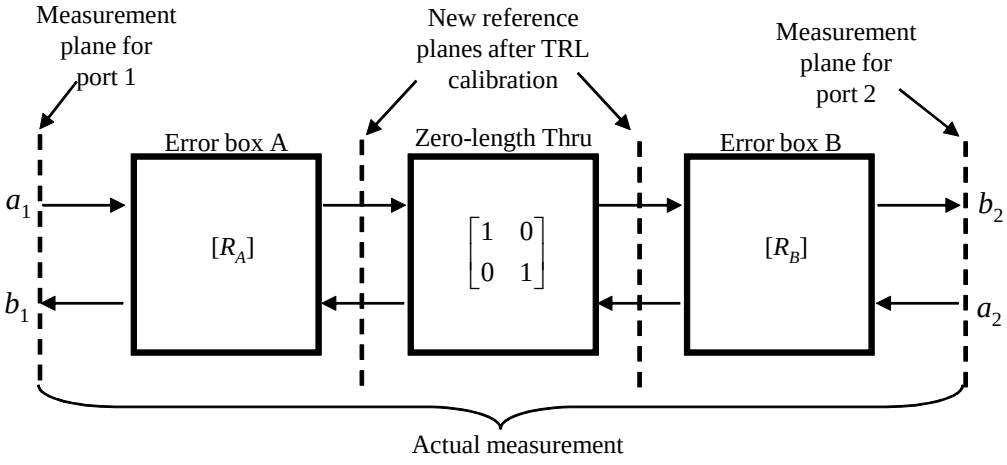

$$R_T = \begin{bmatrix} r_{11t} & r_{12t} \\ r_{21t} & r_{22t} \end{bmatrix} = R_A R_B \qquad \text{(B.2)}$$

Figure B.2: Block diagram of thru-standard measurement

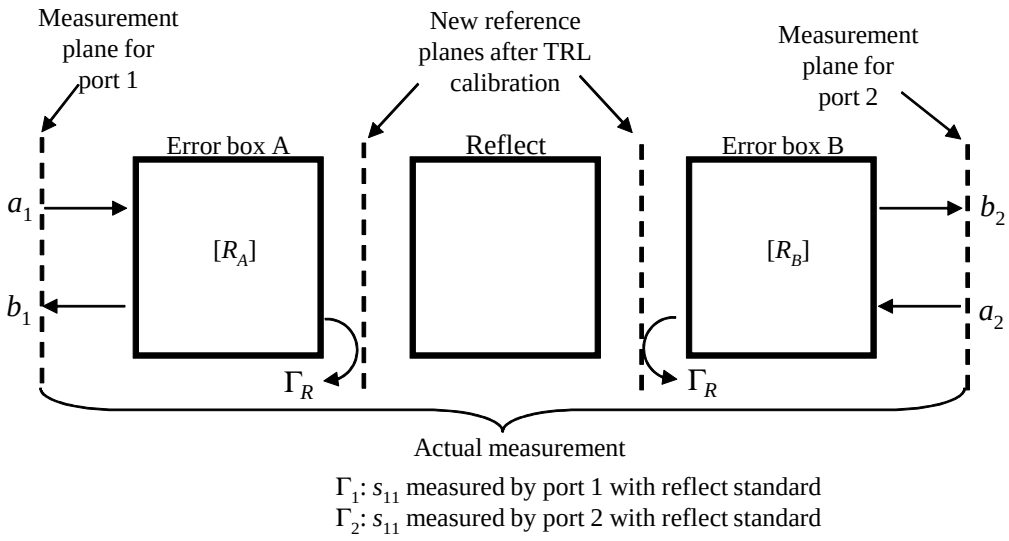

Figure B.3: Block diagram of reflect-standard measurement

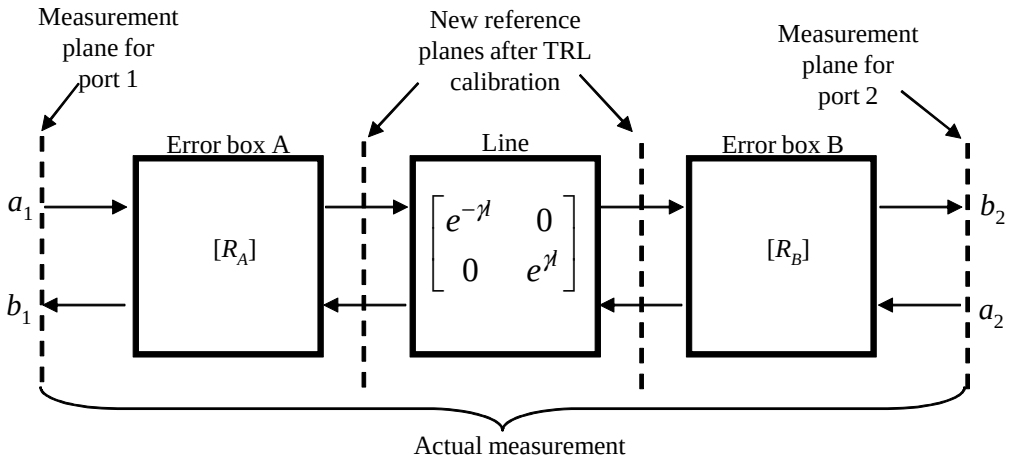

Figure B.4: Block diagram of line-standard measurement

Solving (B.2) for R_B gives

$$R_B = R_A^{-1} R_T. \tag{B.4}$$

Substituting the above into (B.3) yields

$$R_L R_T^{-1} R_A = R_A \begin{bmatrix} e^{-\gamma l} & 0 \\ 0 & e^{\gamma l} \end{bmatrix}, \tag{B.5}$$

By defining $T_A = R_L R_T^{-1}$, (B.5) becomes

$$T_A R_A = R_A \begin{bmatrix} e^{-\gamma l} & 0 \\ 0 & e^{\gamma l} \end{bmatrix}, \tag{B.6}$$

(B.6) provides four linear equations:

$$t_{11a} r_{11a} + t_{12a} r_{12a} = r_{11a} e^{-\gamma l}, \tag{B.7}$$

$$t_{21a} r_{11a} + t_{22a} r_{21a} = r_{21a} e^{-\gamma l}, \tag{B.8}$$

$$t_{11a} r_{12a} + t_{12a} r_{22a} = r_{12a} e^{\gamma l}, \tag{B.9}$$

$$t_{21a} r_{12a} + t_{22a} r_{22a} = r_{22a} e^{\gamma l}, \tag{B.10}$$

Taking the ratio of (B.7) to (B.8) and of (B.9) to (B.10) yields two quadratic equations:

$$t_{21a} \left(\frac{r_{11a}}{r_{21a}} \right)^2 + (t_{22a} - t_{11a}) \left(\frac{r_{11a}}{r_{21a}} \right) - t_{12a} = 0, \tag{A.11}$$

$$t_{21a} \left(\frac{r_{12a}}{r_{22a}} \right)^2 + (t_{22a} - t_{11a}) \left(\frac{r_{12a}}{r_{22a}} \right) - t_{12a} = 0. \tag{A.12}$$

The roots solved from (B.11) and (B.12) are provided below with their corresponding S-parameter expressions:

$$\frac{r_{11a}}{r_{21a}} = \frac{-(t_{22a} - t_{11a}) \pm \sqrt{(t_{22a} - t_{11a})^2 + 4 t_{21a} t_{12a}}}{2 t_{21a}} = s_{11a} - \frac{s_{12a} s_{21a}}{s_{22a}}, \tag{B.13}$$

$$\frac{r_{12a}}{r_{22a}} = \frac{-(t_{22a} - t_{11a}) \mp \sqrt{(t_{22a} - t_{11a})^2 + 4 t_{21a} t_{12a}}}{2 t_{21a}} = s_{11a}, \tag{B.14}$$

where the signs in (B.13) and (B.14) must be correctly chosen to satisfy

$$\left|\frac{r_{11a}}{r_{21a}}\right| > \left|\frac{r_{12a}}{r_{22a}}\right|. \tag{B.15}$$

Following the same procedure but starting with $R_A = R_T R_B^{-1}$ instead of (B.4) provides

$$\frac{r_{11b}}{r_{12b}} = \frac{-\left(t_{22b} - t_{11b}\right) \pm \sqrt{\left(t_{22b} - t_{11b}\right)^2 + 4t_{21b}t_{12b}}}{2t_{12b}} = -s_{22b} + \frac{s_{12b}s_{21b}}{s_{11b}}, \tag{B.16}$$

$$\frac{r_{21b}}{r_{22b}} = \frac{-\left(t_{22b} - t_{11b}\right) \mp \sqrt{\left(t_{22b} - t_{11b}\right)^2 + 4t_{21b}t_{12b}}}{2t_{12b}} = -s_{22b}. \tag{B.17}$$

Similarly, the correct signs are determined by

$$\left|\frac{r_{11b}}{r_{12b}}\right| > \left|\frac{r_{21b}}{r_{22b}}\right|. \tag{B.18}$$

So far, four equations related to the error terms are obtained as in (B.13), (B.14), (B.16), and (B.17). Therefore, we need four more equations to solve all eight error terms. This can be done using the data from the reflect-standard measurement. Using the signal flow graph analysis [49], the reflection coefficients in Fig. B.3 are expressed by

$$\Gamma_1 = s_{11a} + \frac{s_{12a}s_{21a}}{1/\Gamma_R - s_{22a}}, \tag{B.19}$$

$$\Gamma_2 = s_{22b} + \frac{s_{12b}s_{21b}}{1/\Gamma_R - s_{11b}}. \tag{B.20}$$

The above can be combined into a single equation by eliminating the common term Γ_R:

$$s_{22a}\left(1 + \frac{s_{12a}s_{21a}}{s_{22a}}\left(\Gamma_1 - s_{11a}\right)\right) = s_{11b}\left(1 + \frac{s_{12b}s_{21b}}{s_{11b}}\left(\Gamma_2 - s_{22b}\right)\right). \tag{B.21}$$

As observed (B.21) includes several terms we have already solved in (B.13) to (B.18). To keep the equation succinct, let us introduce the following symbols:

$$Q_A = s_{11a} - \frac{s_{12a}s_{21a}}{s_{22a}}, \tag{B.22}$$

$$P_A = s_{11a}, \tag{B.23}$$

$$Q_B = -s_{22b} + \frac{s_{12b}s_{21b}}{s_{11b}}, \tag{B.24}$$

$$P_B = -s_{22b}. \tag{B.25}$$

Using these symbols, (B.21) can be re-written by

$$s_{22a}\left[1 + (P_A - Q_A)(\Gamma_1 - P_A)\right] = s_{11b}\left[1 + (Q_B - P_B)(\Gamma_2 - P_B)\right]. \tag{B.26}$$

Also from the signal flow graph analysis of the thru-standard measurement (see Fig. B.2), we obtain

$$s_{11}^{thru} - s_{11a} = \frac{s_{12a}s_{21a}s_{11b}}{1 - s_{22a}s_{11b}}, \tag{B.27}$$

where s_{11}^{thru} is the measured reflection coefficient with the thru-standard. Using the symbols, (B.27) is re-written by

$$s_{22a}s_{11b} = \left(1 + \frac{P_A - Q_A}{s_{11}^{thru} - P_A}\right)^{-1}. \tag{B.28}$$

From (B.26) and (B.28), s_{11b} and s_{22a} can be solved by

$$s_{11b} = \pm\left[\left(1 + \frac{P_A - Q_A}{\Gamma_1 - P_A}\right)\left(1 + \frac{Q_B - P_B}{\Gamma_2 + P_B}\right)^{-1}\left(1 + \frac{P_A - Q_A}{s_{11}^{thru} - P_A}\right)^{-1}\right]^{1/2}, \tag{B.29}$$

$$s_{22a} = s_{11b}\left(1 + \frac{Q_B - P_B}{\Gamma_2 + P_B}\right)\left(1 + \frac{P_A - Q_A}{\Gamma_1 - P_A}\right)^{-1}. \tag{B.30}$$

Furthermore, substituting these solved quantities into (B.22) and (B.24) gives

$$s_{12a}s_{21a} = (P_A - Q_A)\, s_{22a}, \tag{B.31}$$

$$s_{12b}s_{21b} = (Q_B - P_B)\, s_{11b}. \tag{B.32}$$

That is, with the knowledge of s_{11b} in (B.29), (B.30)-(B.32) are subsequently solved. The correct sign for s_{11b} is determined by observing the phase of Γ_R. From (B.19), Γ_R^{-1} is obtaned as

$$\Gamma_R^{-1} = s_{22a} + \frac{s_{12a}s_{21a}}{\Gamma_1 - s_{11a}}. \tag{B.33}$$

Throughout the calibration bandwidth, the phase of Γ_R^{-1} must not exhibit π-radian jump (2π-radian jump is not a matter). For the frequency range showing such abnormal jump, the sign in (B.29) must be switched to the opposite.

Two more equations are needed to completely solve for (B.1). From the thru-standard measurement set-up (see Fig. B.2), we can also obtain the expressions for the transmission parameters as

$$s_{21}^{thru} = \frac{s_{21a}s_{21b}}{1 - s_{22a}s_{11b}}, \tag{B.34}$$

$$s_{12}^{thru} = \frac{s_{12a}s_{12b}}{1 - s_{22a}s_{11b}}. \tag{B.35}$$

Using these two equations, we obtain

$$s_{21a}s_{21b} = s_{21}^{thru}\left(1 - s_{22a}s_{11b}\right), \tag{B.46}$$

$$s_{12a}s_{12b} = s_{12}^{thru}\left(1 - s_{22a}s_{11b}\right). \tag{B.47}$$

To this end, we have explicit solutions for s_{11a} (B.23), s_{22b} (B.25), s_{11b} (B.29), s_{22a} (B.30), $s_{12a}s_{21a}$ (B.31), $s_{12b}s_{21b}$ (B.32), $s_{21a}s_{21b}$ (B.46), and $s_{12a}s_{12b}$ (B.47). Using these parameters, (B.1) can be completely solved and the calibrated S-parameters can be obtained by converting the wave cascading matrix to S-matrix.

Appendix C

CALCULATION OF REFLECTION COEFFICIENTS FOR COAXIAL PROBE CALIBRATION

Here, we provide solutions for the analytical reflection coefficients of OECP calibration standards in Chapter 6.3. They are A_1 for open, A_2 for load, and A_3 for short standards. Since the ideal reflection coefficient for the short-standard is obviously $A_3 = -1$, we only consider the calculation of A_1 and A_2. A general equation of A_i reflected from a multi-layer media is given in terms of admittance at the coaxial probe aperture (y_{si}) by [99]

$$A_i = \frac{1 - y_{si}}{1 + y_{si}}, \tag{C.1}$$

where

$$y_{si} = \frac{\varepsilon_{ri}}{\sqrt{\varepsilon_r}\ln(b/a)} \int_0^\infty \frac{\left[J_0(k_0\zeta b) - J_0(k_0\zeta a)\right]^2}{\zeta} F_i(\zeta)d\zeta, \tag{C.2}$$

ε_{ri} in (C.2) is the permittivity of material for the air ($\varepsilon_{r1} = 1$) and load ($\varepsilon_{r2} \neq 1$) standards. Otherwise, ε_r in the denominator is the permittivity of material included in the coaxial probe (e.g., $\varepsilon_r = 2.25(1 - j0.001)$ for Polyestyrene). J_0 is Bessel function of the first kind and of order zero. Function $F_i(\zeta)$ results from enforcement of boundary conditions at each layer. For example, there is only one boundary for air

(i.e., boundary between coaxial probe aperture and air). For a load-standard implemented with a finite dielectric slab backed by a PEC, there are two boundaries (i.e., probe aperture-dielectric and dielectric-PEC). $F_i(\zeta)$ for the open and load-standards are given by

$$F_1(\zeta) = \frac{1}{\sqrt{\varepsilon_{r1} - \zeta^2}}, \tag{C.3}$$

$$F_2(\zeta) = \frac{j}{\sqrt{\varepsilon_{r2} - \zeta^2}} \left[\frac{1 + \exp\left(-j2k_0 d\sqrt{\varepsilon_{r2}^2 - \zeta^2}\right)}{1 - \exp\left(-j2k_0 d\sqrt{\varepsilon_{r2}^2 - \zeta^2}\right)} \right], \tag{C.4}$$

where d is the thickness of the load-standard.

References

[1] R. Robert, *Electrical and Magnetic Properties of Materials*. Norwood: Artech House, 1988.

[2] S. Koulouridis, G. Kiziltas, Y. Zhou, D. Hansford, and J. Volakis, "Polymer-ceramic composites for microwave applications: Fabrication and performance assessment," *Microwave Theory and Techniques, IEEE Transactions on*, vol. 54, no. 12, pp. 4202 –4208, Dec. 2006.

[3] V. G. Harris, A. Geiler, Y. Chen, S. D. Yoon, M. Wu, A. Yang, Z. Chen, P. He, P. V. Parimi, X. Zuo, C. E. Patton, M. Abe, O. Acher, , and C. Vittoria, "Recent advances in processing and applications of microwave ferrites," *Journal of Magnetism and Magnetic Materials*, vol. 321, pp. 2035–2047, Jan. 2009.

[4] O. Acher, P. L. Gourrierec, G. Perrin, and O. Robin, "Demonstration of anisotropic composites with tuneable microwave permeability manufactured from ferromagnetic thin films," *Microwave Theory and Techniques, IEEE Transactions on*, vol. 44, no. 5, pp. 674–684, May 1996.

[5] R. M. Walser, "Metamaterials: An introduction," in *Introduction to complex mediums for optics and electromagnetic*, W. S. Weiglhofer and et al., Eds. Bellingham, WA: SPIE Press, 2003.

[6] R. A. Shelby, D. R. Smith, and S. Schultz, "Experimental verification of a negative index of refraction," *Science*, vol. 292, no. 5514, pp. 77–79, 2001.

[7] A. K. Iyer and G. V. Eleftheriades, "A multilayer negative-refractive-index transmission-line (nri-tl) metamaterial free-space lens at x-band," *Antennas and Propagation, IEEE Transactions on*, vol. 55, no. 10, pp. 2746–2753, Oct. 2007.

[8] G. Mumcu, K. Sertel, J. Volakis, I. Vitebskiy, and A. Figotin, "Rf propagation in finite thickness unidirectional magnetic photonic crystals," *Antennas and Propagation, IEEE Transactions on*, vol. 53, no. 12, pp. 4026–4034, Dec. 2005.

[9] S. Yarga, K. Sertel, and J. Volakis, "Degenerate band edge crystals for directive antennas," *Antennas and Propagation, IEEE Transactions on*, vol. 56, no. 1, pp. 119–126, Jan. 2008.

[10] H. Mosallaei and K. Sarabandi, "Magneto-dielectrics in electromagnetics: concept and applications," *Antennas and Propagation, IEEE Transactions on*, vol. 52, no. 6, pp. 1558–1567, Jun. 2004.

[11] P. Ikonen, K. Rozanov, A. Osipov, and S. Tretyakov, "Magneto-dielectric substrates in antenna miniaturization: Potential and limitations," *Antennas and Propagation, IEEE Transactions on*, vol. 2, p. 3391, 2006.

[12] M. Scalora, G. D'Aguanno, N. Mattiucci, M. J. Bloemer, D. de Ceglia, M. Centini, A. Mandatori, C. Sibilia, N. Akozbek, M. G. Cappeddu, M. Fowler, and J. W. Haus, "Negative refraction and sub-wavelength focusing in the visible range using transparent metallo-dielectric stacks," *Optics Express*, vol. 15, no. 2, pp. 508–523, 2007.

[13] M. Sarto, R. Voti, F. Sarto, and M. Larciprete, "Nanolayered lightweight flexible shields with multidirectional optical transparency," *Electromagnetic Compatibility, IEEE Transactions on*, vol. 47, no. 3, pp. 602–611, Aug. 2005.

[14] P. Debye, *Polar Molecules*. New York: Dover, 1929.

[15] M. Afsar, J. Birch, R. Clarke, and G. Chantry, "The measurement of the properties of materials," *Proceedings of the IEEE*, vol. 74, no. 1, pp. 183–199, Jan. 1986.

[16] A. M. Nicolson and G. F. Ross, "Measurement of the intrinsic properties of materials by time-domain techniques," *Instrumentation and Measurement, IEEE Transactions on*, vol. 19, no. 4, pp. 377–382, Nov. 1970.

[17] W. Weir, "Automatic measurement of complex dielectric constant and permeability at microwave frequencies," *Proceedings of the IEEE*, vol. 62, no. 1, pp. 33–36, Jan. 1974.

[18] J. Baker-Jarvis, E. Vanzura, and W. Kissick, "Improved technique for determining complex permittivity with the transmission/reflection method," *Microwave Theory and Techniques, IEEE Transactions on*, vol. 38, no. 8, pp. 1096–1103, Aug. 1990.

[19] L. F. Chen, C. K. Ong, C. P. Neo, V. V. Varadan, and V. K. Varadan, *Microwave Electronics: Measurement and Materials Characterization*. West Sussex, England: Wiley, 2004.

[20] F. Fiorillo, *Measurement and Characterization of Magnetic Materials*. Oxford, U.K.: Elsevier, 2004.

[21] J. Webster, *The Measurement, Instrumentation, and Sensors Handbook, Ch. 8 and 9*. Boca Raton, FL: IEEE Press, 1999.

[22] J. Baker-Jarvis, M. D. Janezic, B. F. Riddle, R. T. Johnk, P. Kabos, C. L. Holloway, R. G. Geyer, and C. A. Grosvenor, "Measuring the permittivity and permeability of lossy materials: solids,liquids, metals, building materials, and negative-indexmaterials," NIST, Tech. Rep. NIST Technical Note 1536, 1990.

[23] J. Baker-Jarvis, C. Jones, B. Riddle, M. Janezic, R. C. Geyer, J. H. Grosvenor, Jr., and C. M. Weil, "Dielectric and magnetic measurements: A survey of nondestructive, quasi-nondestructive and process control techniques," *Research in Nondestructive Evaluation*, vol. 7, no. 8, pp. 117–130, 1995.

[24] J. Krupka, "Frequency domain complex permittivity measurements at microwave frequencies," *Measurement Science Technology*, vol. 17, p. R55R77, Apr. 2006.

[25] B. Lax and K. J. Button, *Microwave Ferrites and Ferrimagnetics*. New York: McGraw-Hill, 1962.

[26] P. Queffelec, P. Gelin, J. Gieraltowski, and J. Loaec, "A microstrip device for the broad band simultaneous measurement of complex permeability and permittivity," *Magnetics, IEEE Transactions on*, vol. 30, no. 2, pp. 224–231, Mar. 1994.

[27] "Basics of measuring the dielectric properties of materials," Application Note 5989-2589EN, Agilent, 2006.

[28] "Solutions for measuring permittivity and permeability with lcr meters and impedance analyzers," Application Note 1369-1, Agilent Technologies, 2003.

[29] H. Bussey, "Measurement of rf properties of materials a survey," *Proceedings of the IEEE*, vol. 55, no. 6, pp. 1046–1053, Jun. 1967.

[30] "Effective impedance measurement using open/short/load correction," Application Note 3463, Hewlett Packard.

[31] C. Grosse and M. Tirado, "Improved calibration of impedance analyzers for measurements on highly conductive liquids," *Instrumentation and Measurement, IEEE Transactions on*, vol. 50, no. 5, Oct. 2001.

[32] V. O. Rastislav Dosoudil, Elemir Usak, "Computer controlled system for complex permeability measurement in the frequency range of 5 hz - 1 ghz," *Journal of Electrical Engineering*, vol. 57, no. 8, pp. 105–109, 2006.

[33] P. D. C. B. W. Hakki, "A dielectric resonator method of measuring inductive capacities in the millimeter range," *Microwave Theory and Techniques, IRE Transactions on*, vol. MTT-8, pp. 402–410, Jul. 1960.

[34] S. Cohn and K. Kelly, "Microwave measurement of high-dielectric-constant materials," *Microwave Theory and Techniques, IEEE Transactions on*, vol. 14, no. 9, pp. 406–410, Sep. 1966.

[35] W. Courtney, "Analysis and evaluation of a method of measuring the complex permittivity and permeability microwave insulators," *Microwave Theory and Techniques, IEEE Transactions on*, vol. 18, no. 8, pp. 476–485, Aug 1970.

[36] Y. Kobayashi and M. Katoh, "Microwave measurement of dielectric properties of low-loss materials by the dielectric rod resonator method," *Microwave Theory and Techniques, IEEE Transactions on*, vol. 33, no. 7, pp. 586–592, Jul 1985.

[37] J. Krupka, K. Derzakowski, B. Riddle, and J. Baker-Jarvis, "A dielectric resonator for measurements of complex permittivity of low loss dielectric materials as a function of temperature," *Measurement Science Technology*, vol. 9, p. 17511756, Oct. 1998.

[38] G. Mumcu, K. Sertel, and J. Volakis, "A measurement process to characterize natural and engineered low-loss uniaxial dielectric materials at microwave frequencies," *Microwave Theory and Techniques, IEEE Transactions on*, vol. 56, no. 1, pp. 217–223, Jan. 2008.

[39] A. Marincic, F. Benson, and J. Tealby, "Measurements of permittivity by the use of surface waves in open and closed structures," *Microwaves, Antennas and Propagation, IEE Proceedings H*, vol. 133, no. 6, pp. 441–449, Dec. 1986.

[40] M. Janezic and J. Baker-Jarvis, "Full-wave analysis of a split-cylinder resonator for nondestructive permittivity measurements," *Microwave Theory and Techniques, IEEE Transactions on*, vol. 47, no. 10, pp. 2014–2020, Oct 1999.

[41] D. Ghodgaonkar, V. Varadan, and V. Varadan, "Free-space measurement of complex permittivity and complex permeability of magnetic materials at microwave frequencies," *Instrumentation and Measurement, IEEE Transactions on*, vol. 39, no. 2, pp. 387–394, Apr. 1990.

[42] W. Barry, "A broad-band, automated, stripline technique for the simultaneous measurement of complex permittivity and permeability," *Microwave Theory and Techniques, IEEE Transactions on*, vol. 34, no. 1, pp. 80–84, Jan. 1986.

[43] G. Hanson, J. Grimm, and D. Nyquist, "An improved de-embedding technique for the measurement of the complex constitutive parameters of materials using a stripline field applicator," *Instrumentation and Measurement, IEEE Transactions on*, vol. 42, no. 3, pp. 740–745, Jun. 1993.

[44] A. Fessant, J. Gieraltowski, J. Loaec, H. Le Gall, and A. Rakii, "Influence of in-plane anisotropy and eddy currents on the frequency spectra of the complex permeability of amorphous cozr thin films," *Magnetics, IEEE Transactions on*, vol. 29, no. 1, Jan. 1993.

[45] J. Hinojosa, "S-parameter broadband measurements on-coplanar and fast extraction of the substrate intrinsic properties," *IEEE Microwave and Wireless Component Letter*, vol. 11, no. 2, pp. 80–82, Feb. 2001.

[46] V. Bekker, K. Seemann, and H. Leiste, "A new strip line broad-band measurement evaluation for determining the complex permeability of thin ferromagnetic films," *Journal of Magnetism and Magnetic Materials*, vol. 270, pp. 327–332, Apr. 2004.

[47] A. Bogle, M. Havrilla, D. Nyquist, L. Kempel, and E. Rothwell, "Electromagnetic material characterization using a partially-filled rectangular waveguide," *Journal of Electromagnetic Waves and Applications*, vol. 19, no. 10, pp. 1291–1306, 2005.

[48] S. Cohn, "Characteristic impedance of the shielded-strip transmission line," *Microwave Theory and Techniques, Trasactions of the IRE Professional Group on*, vol. 2, no. 2, pp. 52–57, Jul. 1954.

[49] D. M. Pozar, *Microwave Engineering, 2nd Ed.* Reading: Addison-Wesley, 1998.

[50] V. Varadan and R. Ro, "Unique retrieval of complex permittivity and permeability of dispersive materials from reflection and transmitted fields by enforcing causality," *Microwave Theory and Techniques, IEEE Transactions on*, vol. 55, no. 10, pp. 2224–2230, Oct. 2007.

[51] U. C. Hasar, "Elimination of the multiple-solutions ambiguity in permittivity extraction from transmission-only measurements of lossy materials," *Microwave and Optical Technology Letters*, vol. 51, no. 2, p. 337341, Feb. 2009.

[52] C.-L. Li and K.-M. Chen, "Determination of electromagnetic properties of materials using flanged open-ended coaxial probe-full-wave analysis," *Instrumentation and Measurement, IEEE Transactions on*, vol. 44, no. 1, pp. 19–27, Feb. 1995.

[53] J. Musil and F. Zacek, *Microwave Measurements of Complex Permittivity by Free Space Methods and their Applications*. Amsterdam: Elsevier, 1986.

[54] N. Gagnon, J. Shaker, P. Berini, L. Roy, and A. Petosa, "Material characterization using a quasi-optical measurement system," *Instrumentation and Measurement, IEEE Transactions on*, vol. 52, no. 2, pp. 333–336, Apr. 2003.

[55] G. Arjavalingam, Y. Pastol, J.-M. Halbout, and G. Kopcsay, "Broad-band microwave measurements with transient radiation from optoelectronically pulsed antennas," *Microwave Theory and Techniques, IEEE Transactions on*, vol. 38, no. 5, pp. 615–621, May. 1990.

[56] L. Carin, K. Agi, D. Kralj, K. Leung, and B. Garetz, "Characterization of layered dielectrics with short electromagnetic pulses," *Quantum Electronics, IEEE Journal of*, vol. 29, no. 7, pp. 2141–2144, Jul. 1993.

[57] D. L. Mensa, *High Resolution Radar Cross-Section Imaging*. Boston: Artech House, 1991.

[58] B. E. A. Saleh and M. C. Teich, *Fundamentals of Photonics*. New York: Wiley, 1991.

[59] T. Eibert, Y. Erdemli, and J. Volakis, "Hybrid finite element-fast spectral domain multilayer boundary integral modeling of doubly periodic structures," *Antennas and Propagation, IEEE Transactions on*, vol. 51, no. 9, pp. 2517–2520, Sep. 2003.

[60] A. Leon-Garcia, *Probability and Random Processes for Electrical Engineering*. Reading, MA: Addison-Wesley, 1994.

[61] "Ece810 class note," Unpublished, Ohio State University, 2005.

[62] F. Sagnard, F. Bentabet, and C. Vignat, "In situ measurements of the complex permittivity of materials using reflection ellipsometry in the microwave band: theory (part i)," *Instrumentation and Measurement, IEEE Transactions on*, vol. 54, no. 3, pp. 1266–1273, June 2005.

[63] T. Nakamura, T. Tsutaoka, and K. Hatakeyama, "Frequency dispersion of permeability in ferrite composite materials," *Journal of Magnetism and Magnetic Materials*, vol. 138, pp. 319–328, Dec. 1994.

[64] K. Buell, H. Mosallaei, and K. Sarabandi, "A substrate for small patch antennas providing tunable miniaturization factors," *Microwave Theory and Techniques, IEEE Transactions on*, vol. 54, no. 1, pp. 135–146, Jan. 2006.

[65] M. Crawford, "Generation of standard em fields using tem transmission cells," *Electromagnetic Compatibility, IEEE Transactions on*, vol. EMC-16, no. 4, pp. 189–195, Nov. 1974.

[66] IEC-61000-4-Series, *Electromagnetic compatibility (EMC) - Part 4: Testing and measurement techniques*.

[67] D. A. Weston, *Electromagnetic Compatibility– Principle and Applications*. New York: Marcel Dekker, 1991.

[68] B. C. Wadell, *Transmission Line Design Handbook*. Norwood, MA: Artech House, 1991.

[69] V. P. Kodali, *Engineering Electromagnetic Compatibility*. Piscataway, New Jersey: IEEE Press, 1996.

[70] G. Engen and C. Hoer, "Thru-reflect-line: An improved technique for calibrating the dual six-port automatic network analyzer," *Microwave Theory and Techniques, IEEE Transactions on*, vol. 27, no. 12, pp. 987–993, Dec 1979.

[71] "Network analysis applying the 8510 trl calibration for non-coaxial measurements," Product Note 8510-8A, Agilent Technologies, 2001.

[72] D. Zhang and C. F. Foo, "Effect of high permeability on the accurate determination of permittivity for mn-zn ferrite cores," *Magnetics, IEEE Transactions on*, vol. 40, no. 6, pp. 3518–3526, Nov. 2004.

[73] A. J. B. Fuller, *Ferrites at Microwave Frequencies*. tevenage, U.K.: Peregrinus, 1987.

[74] M. Pardavi-Horvath, "Microwave applications of soft ferrites," *Journal of Magnetism and Magnetic Materials*, no. 215216, p. 171183, 2000.

[75] T. Tsutaoka, M. Ueshima, T. Tokunaga, T. Nakamura, and K. Hatakeyama, "Frequency dispersion and temperature variation of complex permeability of nizn ferrite composite materials," *Journal of Applied Physics*, vol. 78, no. 6, p. 39833991, 1995.

[76] P. Queffelec, M. Le Floc'h, and P. Gelin, "Broad-band characterization of magnetic and dielectric thin films using a microstrip line," *Instrumentation and Measurement, IEEE Transactions on*, vol. 47, no. 4, pp. 956–963, Aug. 1998.

[77] A. N. Lagarkov, K. N. Rozanov, N. A. Simonov, and S. N. Starostenko, "Microwave permeability of magnetic films," in *Advanced Magnetic Materials, vol.3*, Y. Liu and et al., Eds. Beijing, China: Tsinghua Univ. Press, 2004.

[78] Y. Shimada, M. Yamaguchi, S. Ohnuma, T. Itoh, W. Li, S. Ikeda, K. Kim, and H. Nagura, "Granular thin films with high rf permeability," *Magnetics, IEEE Transactions on*, vol. 39, no. 5, pp. 3052–3056, Sep. 2003.

[79] D. Pain, M. Ledieu, O. Acher, A. L. Adenot, and F. Duverger, "An improved permeameter for thin film measurements up to 6 ghz," *Journal of Applied Physics*, vol. 85, no. 8, pp. 5151–5153, Apr. 1999.

[80] J. Ness, "Broad-band permittivity measurements using the semi-automatic network analyzer," *Microwave Theory and Techniques, IEEE Transactions on*, vol. 33, no. 11, pp. 1222–1226, Nov. 1985.

[81] L. Carin, K. Agi, D. Kralj, K. Leung, and B. Garetz, "Dielectric constant measurement for thin material at microwave frequencies," *Progress in Electromagnetics Research*, vol. 75, pp. 239–252, 2007.

[82] A. Sihvola, *Electromagnetic Mixing Formulas and Applications*. London, U.K.: IEE, 1999.

[83] H. Wheeler, "Transmission-line properties of parallel strips separated by a dielectric sheet," *Microwave Theory and Techniques, IEEE Transactions on*, vol. 13, no. 2, pp. 172–185, Mar. 1965.

[84] B. Bhat and S. K. Koul, "Unified approach to solve a class of strip and microstrip-like transmission lines," *Microwave Theory and Techniques, IEEE Transactions on*, vol. 30, no. 5, pp. 679–686, May. 1982.

[85] R. N. Simons and R. Q. Lee, "Feasibility study of optically transparent microstrip patch antenna," NASA, Tech. Rep. NASA, Tech. Memorandum 107434, 1997.

[86] T. W. Turpin and R. Baktur, "Meshed Patch Antennas Integrated on Solar Cells," *IEEE Antennas and Wireless Propagation Letters*, vol. 8, pp. 693–696, 2009.

[87] F. M. Smits, "Measurement of sheet resistivities with the four-point probe," *Bell System Technical Journal*, vol. 37, pp. 711–718, May 1958.

[88] A. Lynch, A. Drake, and C. Dix, "Measurement of eddy-current conductivity," *IEE Proceedings A*, vol. 130, no. 5, pp. 254–260, July 1983.

[89] R. C. Taber, "A parallel plate resonator technique for microwave loss measurements on superconductors," *Review of Scientific Instruments*, vol. 61, pp. 2200–2206, 1990.

[90] E. K. Moser, W. J. Tomasch, J. K. Furdyna, and J. R. Coffey, M. W.and Clem, "Transmission and reflection of superconducting $YBa_2Cu_3O_{7-x}$ films at 35 ghz," *Applied Superconductivity, IEEE Transactions on*, vol. 3, no. 1, pp. 1119–1122, Mar. 1993.

[91] C.-J. Wu and T.-Y. Tseng, "Effective microwave surface impedance of superconducting films in the mixed state," *Magnetics, IEEE Transactions on*, vol. 33, no. 3, pp. 2348–2355, May 1997.

[92] M. A. Stuchly and S. S. Stuchly, "Coaxial line reflection methods for measuring dielectric properties of biological substances at radio and microwave frequencies-a review," *Instrumentation and Measurement, IEEE Transactions on*, vol. 29, no. 3, pp. 176–183, Sep. 1980.

[93] D. Misra, M. Chabbra, B. Epstein, M. Microtznik, and K. Foster, "Noninvasive electrical characterization of materials at microwave frequencies using an open-ended coaxial line: test of an improved calibration technique," *Microwave Theory and Techniques, IEEE Transactions on*, vol. 38, no. 1, pp. 8–14, Jan 1990.

[94] J. C. Booth, D. H. Wu, and S. M. Anlage, "A broadband method for the measurement of the surface impedance of thin films at microwave frequencies," *Review of Scientific Instruments*, vol. 65, pp. 2082–2090, 1994.

[95] M. L. Stutzman, M. Lee, and R. F. Bradley, "Broadband calibration of long lossy microwave transmission lines at cryogenic temperatures using nichrome films," *Review of Scientific Instruments*, vol. 71, pp. 4596–4599, 2000.

[96] H. Kitano, T. Ohashi, and A. Maeda, "Broadband method for precise microwave spectroscopy of superconducting thin films near the critical temperature," *Review of Scientific Instruments*, vol. 79, no. 7, pp. 074 701–+, 2008.

[97] E. Silva, M. Lanucara, and R. Marcon, "The effective surface resistance of superconductor/dielectric/metal structures," *Superconductor Science and Technology*, vol. 9, no. 11, pp. 934–941, 1996.

[98] D. Rytting, "Network analyzer error models and calibration methods," Agilent, Tech. Rep., 1998.

[99] S. Bakhtiari, S. I. Ganchev, and R. Zoughi, "Analysis of radiation from an open-ended coaxial line into stratified dielectrics," *Microwave Theory and Techniques, IEEE Transactions on*, vol. 42, pp. 1261–1267, 1994.

[100] R. Marks, "A multiline method of network analyzer calibration," *Microwave Theory and Techniques, IEEE Transactions on*, vol. 39, no. 7, pp. 1205–1215, Jul 1991.

[101] J. Green and F. Sandy, "Microwave characterization of partially magnetized ferrites," *Microwave Theory and Techniques, IEEE Transactions on*, vol. 22, no. 6, pp. 641–645, Jun 1974.

[102] C. A. Grimes and J. V. Prodan, "Swept frequency permeameters for measuring the complex, off-diagonal permeability tensor components of anisotropic, thin magnetic films," *Journal of Applied Physics*, vol. 73, no. 10, pp. 6989–6991, 1993.

[103] P. Queffelec, S. Mallegol, and M. LeFloc'h, "Automatic measurement of complex tensorial permeability of magnetized materials in a wide microwave frequency range," *Microwave Theory and Techniques, IEEE Transactions on*, vol. 50, no. 9, pp. 2128–2134, Sep 2002.

[104] O. Hashimoto and Y. Shimizu, "Reflecting rubber characteristics of anisotropic sheets and measurement of complex permittivity tensor," *Microwave Theory and Techniques, IEEE Transactions on*, vol. 34, no. 11, pp. 1202–1207, Nov 1986.

[105] M. Morgan, D. Fisher, and E. Milne, "Electromagnetic scattering by stratified inhomogeneous anisotropic media," *Antennas and Propagation, IEEE Transactions on*, vol. 35, no. 2, pp. 191–197, Feb. 1987.

[106] W. C. Chew, *Waves and Fields in Inhomogeneous Media*. New York: Van Nostrand Reinhold, 1990.

[107] C. Balanis, *Antenna Theory, Analysis, and Design*. New York: Wiley, 1997.

[108] R. R. Pantoja, M. J. Howes, J. R. Richardson, and R. D. Pollard, "Improved calibration and measurement of the scattering parameters of microwave integrated circuits," *Microwave Theory and Techniques, IEEE Transactions on*, vol. 37, pp. 1675–1680, 1989.